Development of the caudal part of the human embryo

Development of the caudal part of the human embryo

Nutmethee Kruepunga

Layout: Tiny Wouters
Design: Nutmethee Kruepunga
Production: Ipskamp Printing, Enschede

The studies presented in this dissertation were supported by 'Stichting Rijp.' and 'the Development and Promotion of Science and Technology Talented project' of Thailand.

ISBN/EAN: 978-94-6421-726-1

Development of the caudal part of the human embryo

DISSERTATION

to obtain the degree of Doctor at the Maastricht University,
on the authority of the Rector Magnificus,
Prof.dr. Pamela Habibović
in accordance with the decision of the Board of Deans,
to be defended in public
on Tuesday 17th May 2022, at 16.00 hours

by

Nutmethee Kruepunga

Supervisor

Prof. dr. S.E. Köhler

Co-supervisors

Dr. J.P.J.M. Hikspoors

Prof. dr. W.H. Lamers

Dr. W. Weerachatyanukul (Mahidol University, Bangkok)

Assessment Committee:

Prof. dr. D.M.A.E. Jonkers, (chair)

Prof. dr. J.-P. Timmermans (University of Antwerp, Belgium)

Prof. dr. D. Tibboel (Erasmus MC, Rotterdam, the Netherlands)

Dr. V. Melotte

Dedicated to my inspiring teacher in embryology
Assoc.Prof. Jantima Rungruangchai, D.D.S, Ph.D.

"The place where you belong is the place where you are recognized"
Sririta J. Narongdej

Table of contents

Chapter 1
Introduction

Developmental anatomy, also known as embryology, is the study of the temporal changes in the structural organization of the components of embryos and foetuses. Developmental anatomy's main aim is to explain the successive steps in building 'normal' adult structures, but also to deduce the developmental history of malformed adult structures. Currently, both developmental and gross anatomy are usually considered to be core courses for medical students. Their essential contents have been suggested as core syllabuses (Smith et al., 2016, Holland et al., 2019). Because developmental anatomy traces the successive steps that lead to the building of a definitive structure, whether normal or abnormal, it is the basis of adult anatomy and the clinically relevant variations thereof. Although medical schools usually require medical students to take embryological courses, they are often considered as less important than courses in gross (adult) anatomy. This relative lack of appreciation of developmental relative to adult anatomy comes back in a smaller study load in the medical curriculum (McBride and Drake, 2018, Rockarts et al., 2020). Terminology in developmental and adult anatomy is largely the same, so having to learn anatomical terms by heart should not deter students from engaging in developmental anatomy. A possible reason for the lesser importance of courses focusing on developmental anatomy could be the lack of realistic images of developing structures that support the written or spoken explanatory text during classes. There are at least four aspects of developmental anatomy that may impede its acceptance: complexity, continuity, visualization, and content.

Challenging aspects in developmental anatomy

Complexity due to temporal changes

The complexity of the developing body makes it a challenge to visualise and describe adequately. In general, the three dimensions of space are necessary to describe the shape and topography of both embryonic and adult structures (O'Rahilly and Müller, 2001, Gasser, 2006, Mitteroecker and Huttegger, 2009, Kicheva and Briscoe, 2015, Sharpe, 2017, Standring and Gray, 2021). The three conventional axes of description are medio-lateral, dorso-ventral, and cranio-caudal (Figure 1.1A). In addition, the time axis is an essential fourth dimension in developmental anatomy, because the structures change in shape, size, and hence, position in the prenatal period. In other words, the positional values in any of the three dimensions fluctuate along the time axis (Meinhardt, 2015)(Figure 1.1B). This fourth dimension, often summarized as spatiotemporal changes, make developmental anatomy more complex than gross anatomy, which "only" describes the static configuration of adult structures. The anatomy of the small intestine in embryos and the adult can serve as an example. Both embryonic and adult small intestine are coiling tubes but the coiling stabilities

are different. The adult coil is almost completely stable but the embryonic intestine increases in coil complexity due to embryonic growth. In terms of structure it starts from a straight tube called the midgut. The midgut undergoes three generations of looping to form four whirls that each have their own mesentery (Soffers et al., 2015). The loopings themselves are complex as well. Due to an asymmetric starting position and extensive growth, the primary loop reorients itself from mostly sagittal to largely transverse. Then 4 secondary loops form along the primary loop. Apart from the looping process, the position of the small intestine is dynamic. It is initially located entirely inside the abdominal cavity, but partially herniates into the extra-abdominal space between 6 and 9.5 weeks of development, to finally return again into the abdominal cavity (Soffers et al., 2015, Nagata et al., 2019).

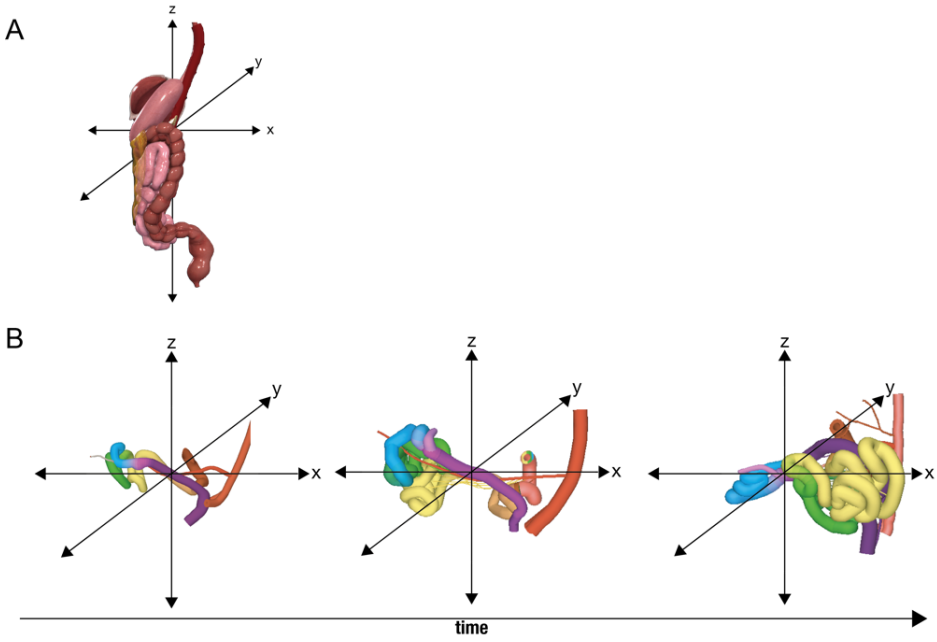

Figure 1.1 **The difference in dimensions between adult (panel A) and developmental (panel B) anatomy**. All images represent left-sided views. Panel A shows that the topography of adult anatomy is explained by three dimensions (image courtesy of Complete Anatomy). In contrast, panel B (adapted from (Soffers et al., 2015)) shows that the topography of developmental anatomy is explained by the same three dimensions plus the additional dimension of time.

Continuity in description

A proper continuity of descriptive information over time can facilitate the understanding of developmental phenomena. In embryos, informative time-

dependent changes are often summarised in stages of development. The first 8 weeks of human development are subdivided in 23 Carnegie stages. The first 18 stages, which cover the first 6.5 weeks of development (O'Rahilly and Müller, 2010) describe relevant time-dependent differences of structures in size and shape, whereas the last 5 stages based on a more quantitative assessment of organ development (e.g. branching morphogenesis of lung, pancreas and kidney; (Streeter, 1951)). In standard textbooks, page layout often limits the number of panels (≈ stages) in Figures illustrating a particular developmental concept to at most six (Carlson, 2014, Sadler, 2015, Schoenwolf et al., 2015, Moore et al., 2016). Limitations of the number of images then generate unexplainable gaps between the developmental steps shown. Without such intermediate steps, an imaginary explanation by an author or teacher often fills the gap and creates confusion.

Visualisation of 3D features

Because of their minute size, classical methods to study embryos are based on serial sectioning of these embryos, followed by standard staining protocols. Alternatively, whole-mount (intact) embryos are stained. Whole mounts display mainly external features of the embryo due to the poor penetration of dyes (Chandler and Roberson, 2009) and scattering of light. The information obtained from serial sections depends on the plane of sectioning. Transversely cut sections are more or less bilaterally symmetric and, hence, relatively easy to understand. These sections provide information on medio-lateral and dorso-ventral position of the structure of interest, but depend on 3D reconstruction of the sections for information on the cranio-caudal course of structures (O'Rahilly and Müller, 2001). Sagittally cut sections, on the other hand, provide information dorso-ventral and cranio-caudal aspects of the structure of interest, but need 3D reconstruction to analyse medio-lateral aspects. Reconstructions used to be made from wax sections, in which the structure of interest was present. Sometimes these wax reconstructions served as template to cast a 3D model. The famous models of the Blechschmidt collection at the University of Goettingen, Germany, are an example of this very labor-intensive methodology (Hinrichsen et al., 1990, Markert, 2020).The ability to inspect a physical 3D model from all sides greatly supports its understanding. The main disadvantage of these models is that they cannot be changed. Some of the disadvantages of the sectional approach are neutralised in present-day computer-aided reconstructions and visualizations.

Content

The analysis of developmental mechanism commonly focuses on specific structures rather than relatively change in either surrounding tissues or the whole body. Descriptions and reconstructions must be meaningful, that is, include not only the

structure of interest, but also surrounding structures, such as dense mesenchymal agglomerates, nerve fibres, vertebrae for segmental levels, or even the entire embryonic body contour. This information is often left out of 3D reconstructions because their implementation is time-consuming and requires complex reconstructions. Such missing information can lead to misinterpretation of developmental mechanisms, such as the difference between the “primary” and “secondary” sympathetic trunks (see Chapter 5). The relationship of the sympathetic trunks with the surrounding tissues, in particular the dorsal aortae and vertebral bodies (commonly used landmarks) defined the type of sympathetic trunks: the “primary” sympathetic trunks locate between the dorsal aorta and vertebral column (so-called prevertebral position), whereas the “secondary” sympathetic trunks are positioned lateral to the vertebrae (so-called paravertebral position). The apparent dorsal migration of the sympathetic trunks can represent a “real” change in position (Kasemeier-Kulesa et al., 2015) but is, as we show, more likely the result of differential growth of the tissues surrounding the trunks. In fact, changes in size and shape of tissues surrounding a structure of interest often determine its temporal apparent change in position. There are 2 axial hinge points involving in the folding and unfolding processes during development. The cranial point is at the transition of head and trunk, while the caudal is the transition of supraumbilical and infraumbilical regions. The angles of the body axis at these hinge points change during embryonic folding and unfolding processes.

Aims and outline of this thesis

In the present study we aim to fill some of the gaps in the description and presentation of the developmental anatomy of the caudal end of the human body. We studied embryos and fetuses at several time points between 4 and 10 weeks of development to allow for a continuous description without gaps that compromise understanding of successive steps in development. During gastrulation, in the 4th week of development, the definitive body plan of the embryo is laid down, while most organs have reached their definitive configuration at 10 weeks of development. Our descriptions and visualisations focused on the lesser pelvis. The lesser or "true” pelvis is the space enclosed by the pelvic girdle laterally and by the pelvic inlet superiorly and the pelvic floor inferiorly. The pelvic inlet is delineated by a bone crest formed by the iliac and pubic bones that extends from the sacral promontory to the upper surface of the pubic symphysis. To visualise and explain developmental anatomy of the lesser pelvis, we have chosen 3D reconstruction as a key tool. We have reconstructed, in addition to the structures of interest, also surrounding structures, such as vertebral bodies and nerve fibres, to produce space-filling models. We have not only studied the developmental changes in architecture qualitatively, but also

quantitatively to reveal developmental changes in the contribution of structures to pelvic anatomy.

In Chapter 2, we describe the developmental anatomy of the caudal part of the gut. At 4 weeks, it is a simple tube of which the caudal-most end is still forming. In the lesser pelvis it visually widens to form the cloaca. The cloaca eventually gives rise to separate passages for the urogenital and gastrointestinal tracts, but the mechanism of cloacal subdivision into these two passages has remained contentious. We, therefore, reinvestigated the cloaca of human embryos between 4 and 8 weeks of development, including its surrounding tissues, by 3D reconstruction and quantitation of distances between landmark structures. This study was awarded the Journal of Anatomy Best Paper Prize for 2018.

In Chapters 3 and 4, we extended our analysis to the histologically identifiable tissues which surround the cloaca, in particular the nerves. Although the human embryos that we studied were stained with standard dyes, nerve fibres and ganglionic cells were easily identifiable because of their relatively large size and typical staining pattern. Ganglionic cells and nerve fibres were segmented separately to follow their spatiotemporal changes in position relative to landmark structures, such as the gut and cloaca, main arteries, and developing vertebrae. In Chapters 3 and 4, the extrinsic innervation of the gut was probed in the abdominal (Chapter 3) and pelvic (Chapter 4) parts of the coelom. In chapter 4, we also compared the developmental patterns of ganglionic cells and nerve fibres in abdominal and pelvic regions.

The autonomic nerves to the gut have their origin in the spinal cord (preganglionic fibres) or in the sympathetic trunk (postganglionic fibres). The development of both sympathetic trunks and their vertical connections was studied in Chapter 5. In addition to architectural changes in sympathetic trunks (regional differences in the size of the ganglia and their connecting fibres), we also established that the difference between the “primary” and “secondary” sympathetic trunks is mediated at least in part by regional differences in the growth of surrounding structures.

In Chapter 6, finally, we discuss differences in the developmental patterns of the autonomic innervation of the gut in the abdominal and pelvic cavities. In addition, we discuss advances in 3D technology, and current resources which facilitate descriptive studies of human embryos and fetuses.

References

Carlson BM (2014) *Human embryology and developmental biology,* Saunders-Elsevier, Philadelphia.

Chandler DE, Roberson RW (2009) *Bioimaging : current concepts in light and electron microscopy,* Jones and Bartlett Publishers, Sudbury, Mass.

Gasser RF (2006) Evidence that some events of mammalian embryogenesis can result from differential growth, making migration unnecessary. *The Anatomical Record Part B: The New Anatomist,* 289B, 53-63.

Hinrichsen KV, Beier HM, Breucker H, et al. (1990) *Humanembryologie,* Springer Berlin Heidelberg, Berlin, Heidelberg.

Holland JC, Smith C, O'Shea M, Stewart J, Ockleford C, Finn GM (2019) The anatomical society core embryology syllabus for undergraduate medicine. *Journal of Anatomy,* 235, 847-860.

Kasemeier-Kulesa JC, Morrison JA, Lefcort F, Kulesa PM (2015) TrkB/BDNF signalling patterns the sympathetic nervous system. *Nature Communications,* 6, 8281.

Kicheva A, Briscoe J (2015) Developmental Pattern Formation in Phases. *Trends in Cell Biology,* 25, 579-591.

Markert M (2020) Ethical Aspects of Human Embryo Collections: A Historically Grounded Approach to the Blechschmidt Collection at the University of Göttingen. *Cells Tissues Organs,* 209, 189-199.

McBride JM, Drake RL (2018) National survey on anatomical sciences in medical education. *Anatomical Sciences Education,* 11, 7-14.

Meinhardt H (2015) Models for patterning primary embryonic body axes: The role of space and time. *Seminars in Cell & Developmental Biology,* 42, 103-117.

Mitteroecker P, Huttegger SM (2009) The Concept of Morphospaces in Evolutionary and Developmental Biology: Mathematics and Metaphors. *Biological Theory,* 4, 54-67.

Moore KL, Persaud TV, Torchia MG (2016) *The developing human : clinically oriented embryology,* Elsevier, Philadelphia.

Nagata A, Hatta S, Ji X, et al. (2019) Return of the intestinal loop to the abdominal coelom after physiological umbilical herniation in the early fetal period. Journal of Anatomy, 456-464.

O'Rahilly R, Müller F (2001) Human embryology & teratology, Wiley-Liss, New York.

O'Rahilly R, Müller F (2010) Developmental Stages in Human Embryos: Revised and New Measurements. *Cells Tissues Organs,* 192, 73-84.

Rockarts J, Brewer-Deluce D, Shali A, Mohialdin V, Wainman B (2020) National Survey on Canadian Undergraduate Medical Programs: The Decline of the Anatomical Sciences in Canadian Medical Education. *Anatomical Sciences Education,* 13, 381-389.

Sadler TW (2015) *Langman's medical embryology,* Wolters Kluwer, Philadelphia.

Schoenwolf GC, Bleyl SB, Brauer PR, Francis-West PH (2015) *Larsen's human embryology,* Elsevier/Churchill Livingstone, Philadelphia.

Sharpe J (2017) Computer modeling in developmental biology: growing today, essential tomorrow. *Development,* 144, 4214.

Smith CF, Finn GM, Stewart J, et al. (2016) The Anatomical Society core regional anatomy syllabus for undergraduate medicine. *Journal of Anatomy,* 228, 15-23.

Soffers JH, Hikspoors JP, Mekonen HK, Koehler SE, Lamers WH (2015) The growth pattern of the human intestine and its mesentery. *BMC Developmental Biology,* 15, 31-.

Standring S, Gray H (2021) *Gray's anatomy : the anatomical basis of clinical practice*, Elsevier, Amsterdam.

Streeter G (1951) Description of age groups XIX, XX, XXI, XXII and XXIII, being the fifth issue of a survey of the Carnegie collection. *Contrib. Embryol. Carneg. Inst,* 34, 165-196.

Chapter 2
The development of the cloaca in the human embryo

Nutmethee Kruepunga, Jill P.J.M. Hikspoors, Hayelom K. Mekonen, Greet M.C. Mommen, Krai Meemon, Wattana Weerachatyanukul, Somluk Asuvapongpata, S. Eleonore Köhler, Wouter H. Lamers
Journal of Anatomy (2018); 233(6): 724-739

"The Journal of Anatomy Best Paper Prize 2018" ★
"The Top 10% Most Downloaded Papers 2018-2019" ★
"Suggested as a key reference in Gray's Anatomy 42nd edition" ★

Abstract

Subdivision of cloaca into urogenital and anorectal passages has remained controversial because of disagreements about the identity and role of the septum developing between both passages. This study aimed to clarify the development of the cloaca using a quantitative 3D morphologic approach in human embryos of 4-10 post-fertilisation weeks. Embryos were visualised with Amira 3D-reconstruction and Cinema 4D-remodelling software. Distances between landmarks were computed with Amira3D software. Our main finding was a pronounced difference in growth between rapidly expanding central and ventral parts, and slowly or non-growing cranial and dorsal parts. The entrance of the Wolffian duct into the cloaca proved a stable landmark that remained linked to the position of vertebra S3. Suppressed growth in the cranial cloaca resulted in an apparent craniodorsal migration of the entrance of the Wolffian duct, while suppressed growth in the dorsal cloaca changed the entrance of the hindgut from cranial to dorsal on the cloaca. Transformation of this "end-to-end" into an "end-to-side" junction produced temporary "lateral (Rathke's) folds". The persistent difference in dorsoventral growth straightened the embryonic caudal body axis and concomitantly extended the frontally oriented "urorectal (Tourneux's) septum" caudally between the ventral urogenital and dorsal anorectal parts of the cloaca. The dorsoventral growth difference also divided the cloacal membrane into a well-developed ventral urethral plate and a thin dorsal cloacal membrane proper, which ruptured at 6.5 weeks. The expansion of the pericloacal mesenchyme followed the dorsoventral growth difference and produced the genital tubercle. Dysregulation of dorsal cloacal development is probably an important cause of anorectal malformations: too little regressive development may result in anorectal agenesis and too much regression in stenosis or atresia of the remaining part of the dorsal cloaca.

Introduction

The cloaca is the common compartment of the urogenital and anorectal channels in the 5th developmental week of humans that subdivides into two separate passages during the 6th and 7th weeks. The process of cloacal subdivision has remained controversial even though it has been studied for well over a century. Two main hypotheses exist to account for subdivision of the cloaca. The classical model, which is present in standard textbooks, is the “active" concept (Carlson, 2014, Moore et al., 2016): a frontally oriented urorectal septum (“Tourneux’s” septum) actively expands caudally to divide the cloaca into its two compartments (Tourneux, 1888, Pohlman, 1911, Quan et al., 2000). The problem with Tourneux’s septum has always been that it is shown only as a midline structure without adequate description of its more lateral extension. Alternatively, lateral folds in the wall of the cloaca (“Rathke’s” folds) merge in caudal direction (Rathke, 1832, Retterer, 1890, Reichel, 1893). Although Rathke is credited with the description of the lateral folds, these structures, which are all but invisible in his miniature drawings, are often cited without proper definition of their composition or position. More than 30 years ago the “passive” concept was formulated (van der Putte and Neeteson, 1983, Kluth et al., 1995): the urorectal septum extends caudally due to differential growth in the (peri-)cloacal region, which results in “unfolding” of the caudal body axis of the embryo (van der Putte and Neeteson, 1983, Zhang et al., 2011, Xu et al., 2012, Huang et al., 2016). However, apart from the unfolding of the caudal body axis (Paidas et al., 1999), the description of the passive concept has been qualitative thus far. In particular, regional differences in cloacal growth have been implicated, but not yet quantified.

The cloacal membrane and pericloacal mesenchyme are important components of the cloacal region. We define the cloacal membrane as that part of the cloacal wall where ectoderm and endoderm have no basal membrane, that is, are indistinguishable. The cloacal membrane is usually described as a thin membrane that eventually ruptures to provide a passage for the urogenital and anorectal channels (Felix, 1912, Kluth et al., 1995, Paidas et al., 1999, van Der Werff et al., 2000). However, other studies have described the cloacal membrane as consisting of a well-developed solid mass ventrally (“urethral plate”) and a thin cloacal membrane “proper” dorsally. The urethral plate (also known as “cloacal plate” (Penington and Hutson, 2002a)) expands ventrally and cranially concomitant with the growth of the genital tubercle, whereas the cloacal membrane proper does not grow and eventually even ruptures (Tourneux, 1888, Penington and Hutson, 2002a, Li et al., 2015). These data suggest that

the ventral and dorsal parts of the original cloacal membrane have quite different characteristics. In addition, the mesenchymal components in the cloacal region have attracted interest because of their role in regional growth differences that underlie the subdivision of the cloaca according to the passive concept (van der Putte and Neeteson, 1983, Sasaki et al., 2004, Huang et al., 2016).

Visualization of the cloacal region has proved challenging (Ikebukuro and Ohkawa, 1994, Kluth et al., 2011). The cloaca is usually shown as a midsagittal drawing, with histological sections to support developmental processes in other planes. In addition, the growth pattern in the cloacal region has been globally described (van der Putte, 2004), with most quantitative histological data addressing cell proliferation and apoptosis (Sasaki et al., 2004, Nebot-Cegarra et al., 2005, Matsumaru et al., 2015, Huang et al., 2016). To clarify the growth pattern and the fate of the components of the cloacal region, we reinvestigated the changes in shape of the cloaca, including its lumen, wall, and surrounding mesenchyme in human embryos and foetuses between 4 and 10 weeks of development. Changes in size and shape were assessed qualitatively and quantitatively in three-dimensional reconstructions to establish the growth pattern. We report that the cloaca consisted of a ventral "growing" zone initially sandwiched between cranial and dorsal "non-growing" zones that account for the changes in cloacal shape during the period studied.

Materials and methods

This study was undertaken in accordance with the Dutch regulations for the proper use of human tissue for medical research purposes. Anonymized specimens from the historical collections of human embryos of the Departments of Anatomy and Embryology, Leiden University Medical Centre (LUMC), Leiden, Academic Medical Centre (AMC), Amsterdam, and Radboud University, Nijmegen, The Netherlands, that were donated for scientific research were included. In addition, digital images of human embryos of the Carnegie collection (Washington D.C., USA) were downloaded from the Digitally Reproduced Embryonic Morphology (DREM) project (http://virtualhumanembryo.lsuhsc.edu).

Image acquisition, 3D reconstruction, and visualization

Well-preserved human embryos and foetuses between 4–10 weeks of development were studied (Table 2.1. The criteria of O'Rahilly as modified in 2010 were used to

determine the Carnegie Stage of development and post-fertilisation age of the embryos ((O'Rahilly and Müller, 2010); Table 2.2). We subdivided CS14 into CS14-early, -intermediate and -late because of rapid developmental changes during this stage. The collection from which we selected this group amounts to ~150 embryos (collections in LUMC and AMC). Selection criteria were histological quality of the sections (embryos undergo autolysis (maceration) quite quickly) and developmental stage. The main limitation to use more embryos was the time required for their 3D reconstruction: scanning and aligning sections remain very time-consuming activities. Instead, we used quantitative (Figures 2.1 and 2.5) and qualitative (Figures 2.2, 2.6, and 2.7) chronological development as our most important indicators for adequate description. Accordingly, developmental trends in our account are not based on a single developmental stage. Furthermore, the correlation coefficients that we report are characteristically >0.8. If a discontinuity or a discrepancy with literature is found, we do check sections of the non-reconstructed group of embryos to confirm our findings.

Table 2.1 Average ages of CS (Adapted from (O'Rahilly and Müller, 2010)

CS	Ages (days)
10	28
11	29
12	30
13	31
14-early*	33
14-intermediate*	34
14-late*	35
15	36
16	39
17	41
18-early	43
18-late	45
20	49
23	56
9 weeks	63
10 weeks	70

* We subdivided CS14 into early, intermediate, and late because of rapid developmental changes during this stage.

Table 2.2: Sources of human embryos and foetuses.

Stage	Embryo number	Section plane	Source
CS10	S6330	Transverse	DREM
CS11	S6344	Transverse	DREM
CS12	S8943	Transverse	DREM
CS13	S836	Transverse	DREM
CS14-early*	S2201	Transverse	AMC
CS14-intermediate*	S5029	Sagittal	AMC
CS14-late*	S6502	Transverse	DREM
CS15	S2213	Transverse	AMC
CS15	S721	Transverse	DREM
CS16	S5032	Sagittal	AMC
CS16	S6517	Transverse	DREM
CS16	S39	Transverse	LUMC
CS17	S6520	Transverse	DREM
CS18-early	S97	Transverse	LUMC
CS18-late	S4430	Transverse	DREM
CS19	S9325	Transverse	DREM
CS20	S2025	Transverse	AMC
CS20	S462	Transverse	DREM
CS20	S34	Sagittal	LUMC
CS21	S4090	Transverse	DREM
CS22	S983	Transverse	DREM
CS23	S4141	Transverse	AMC
CS23	S9226	Transverse	DREM
CS23	S48	Transverse	LUMC
CS23	S88	Sagittal	RadboudMC
9 weeks	S89	Transverse	LUMC
9.5 weeks	S57	Transverse	LUMC
10 weeks	S1507	Transverse	AMC

*: We subdivided CS14 because of rapid developmental changes during this stage.

The serial sections from AMC, LUMC, and Radboud were digitized with an Olympus BX51 or BX61 microscope and the Dotslide program (Olympus, Leiderdorp, The Netherlands). All images were converted into greyscale 'JPEG' format and loaded into Amira3D (version 6.0; base package; FEI Visualization Sciences Group Europe, Merignac Cedex, France). The greyscale images were aligned automatically with the least-squares alignment mode and then manually adjusted for correct curvature of the embryonic body axis with the help of photographs and magnetic resonance images of human embryos of the same stage (Pooh et al., 2011). Structures of interest were segmented manually and reconstructed three-dimensionally with the Amira3D program. Small deformations of individual sections due to the histological processing and stepwise stacking of sections conferred a distracting noise on the 3D reconstructions. Therefore, polygon meshes from all reconstructed materials were exported via 'vrml export' from Amira3D to Cinema 4D (MAXON Computer GmbH, Friedrichsdorf, Germany) and remodelled using the Amira3D

model as template. The accuracy of the remodelling process was safeguarded by simultaneous visualization in Cinema 4D of the original output from Amira and the remodelled Cinema model (Supplemental Figure S2.1). The Cinema-4D models were transferred via 'wrl export' to Adobe Acrobat version 9 (http://www.adobe.com) to generate interactive 3D Portable Device Format (PDF) files, which are an easily accessible format for 3D visualization (Supplemental Figures S2.1 and S2.4-2.6).

Measurements

All morphometric analyses were performed in Amira3D. Analyses included angles between landmarks on the vertebral column, topographic position of landmarks, and distances between landmarks. The data was subsequently analysed in Microsoft Excel (Microsoft Corporation, Washington, USA). We used 9 landmarks: 1) individual vertebrae, 2) the insertion of the Wolffian duct into the cloaca/urogenital sinus, 3) the transition of epithelium between urogenital sinus (pseudostratified columnar) and allantois (low cuboidal), 4) the transition of epithelium between urethral plate (stratified epithelium) and cloacal membrane (simple epithelium), 5) the caudal tip of the urorectal septum, 6) the caudal (deepest) point of the peritoneal trough in the urorectal septum, 7) the caudal end of the dense cuff of mesenchyme surrounding the hindgut, 8) the distal (ventral-most) tip of the mesenchymal condensation in the genital tubercle, and 9) the tail fold. When the tail fold was no longer identifiable (after CS20), we used the midpoint between the external anal sphincter and the caudal tip of the coccyx. The cloacal membrane was defined as the area where the basal membrane between endodermal and ectodermal epithelium could not be distinguished. The transition of the (ventral) urethral plate into the (dorsal) cloacal membrane proper marks the boundary of growing and non-growing parts of the cloaca. The caudal cone of the dense cuff of mesenchyme surrounding the hindgut is a marker of the caudal end of the hindgut epithelium during the stages we studied (van der Putte and Neeteson, 1983).

Results

Axial curvature of embryo

The caudal end of the embryo bent ventrally between CS11 and CS13, and straightened again between CS14 and CS23. We determined the time course of this process by

establishing the position of the C1, T1, L1, S1 and S5 vertebrae, and marking their centre on the notochord, which is an unambiguous and, therefore, reliable midline structure. Next, the angles determined by C1-T1-L1, T1-L1-S1, and L1-S1-S5 were measured. Vertebrae are still added caudally until CS14 (Figure 2.1A-C; cf. (O'Rahilly and Müller, 2003)). This extension results in a helical shape of the embryonic axis (Soffers et al., 2015). From CS14 onwards, the caudal region straightened (Figure 2.1D-F). To confirm the unfolding process, C1-T1-L1, T1-L1-S5 and L1-S1-S5 angles were measured (Figure 2.1G). Neck and thorax, as measured with the C1-T1-L1 angle, straightened slightly, but the lumbar (T1-L1-S5) and, in particular, the sacral region (L1-S1-S5) straightened in a more pronounced fashion between 4.5 and 6 weeks (CS14-CS17). After 6 weeks, only the L1-S1-S5 angle continued to increase (Figure 2.1H), which corresponds with the development of the promontory (the lumbar lordosis only develops after birth (Reichmann and Lewin, 1971)).

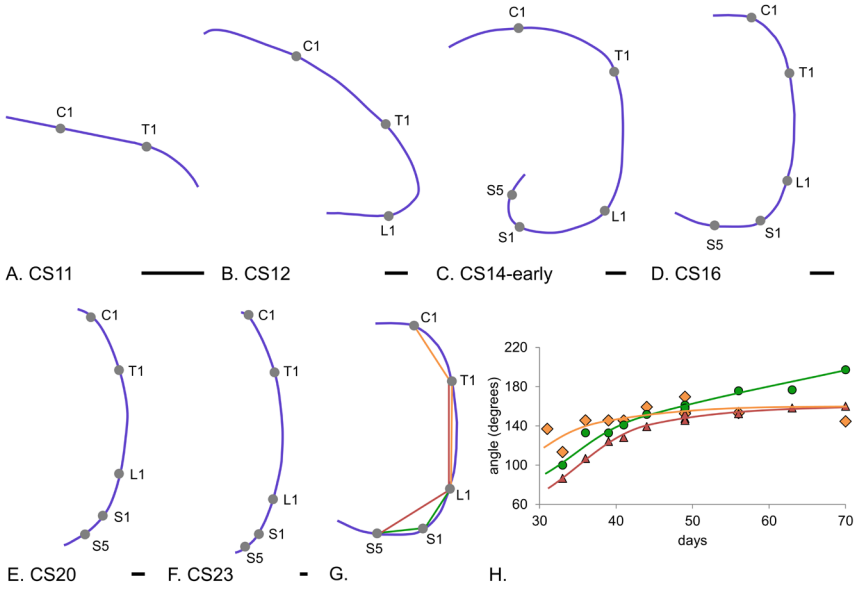

Figure 2.1 **Curvature of the embryonic axis between 4 and 10 weeks post-fertilisation**. Panels A-F show left-sided views of the notochord as landmark for the embryonic axis. Panels A-C show that, concomitant with the addition of vertebrae (grey dots) up to CS14-early (33 days), the caudal body axis folded ventrally to straighten again between 34 and 42 days (panels D-F). The angles of C1-T1-L1 (orange diamonds; R2: 0.62), T1-L1-S5 (red triangles; R2: 0.97) and L1-S1-S5 (green circles; R2: 0.94) that quantify this process are shown in panels G and H. The continuing increase in the L1-S1-S5 angle reflects the development of the sacral promontory. Abbreviations: C1, 1st cervical level; T1, 1st thoracic level; L1, 1st lumbar level; S1, 1st sacral level; S5, 5th sacral level. Bar = 500 µm.

Shape of the developing cloaca

The cloaca connects to both allantois and hindgut. As the caudal end of the embryo folded and unfolded, the cloaca changed its shape (Figure 2.2). From CS12 onwards the boundary of cloaca and allantois was identifiable as the transition of pseudostratified columnar epithelium (cloaca) into low cuboidal epithelium (allantois; Figure 2.3A-E). We defined the cloacal membrane as the area where a basal membrane could not be distinguished between the endo- and ectodermal epithelium. Concomitant with caudal folding, cloaca and cloacal membrane elongated. This expansion corresponded in time with the presence of the tailbud in the caudal-most part of the embryo, which suggested that the tailbud provided cells for cloacal growth. The Wolffian ducts also extended caudally and inserted into the cloaca at CS13 (Figure 2.2B,C), coincident with the disappearance of the tailbud. Subsequently, the caudal end of the body, including the cloaca, started to unfold. Furthermore, the part of the cloaca distal to the cloacal membrane began to regress by narrowing into the so-called "tailgut", a transient structure that could only be identified during CS14 and disappeared entirely during CS15 (Figures 2.2D-F and 2.4A). The junction of cloaca and hindgut became identifiable, because the hindgut epithelium thickened and the ventrocranial part of the cloaca widened more rapidly than the dorsocaudal part of the cloaca and the hindgut in CS13 and CS14 embryos (Figure 2.3). Because the junction of hindgut and cloaca came to resemble the obliquely connected spout of a watering can, a semilunar ridge defined the cranial part of their junction on the inside (asterisks in Figure 2.3). We interpreted this semilunar ridge as the so-called "lateral folds" of the cloaca in many early studies (Retterer, 1890, Reichel, 1893). Figure 2.3F gives a 3D impression of the lateral folds between cloaca and hindgut at CS14-intermediate, when they extend to the Wolffian ducts. The lateral folds were identifiable from CS13 (31 days) to CS14-late (35 days; Figure 2.3), when the folds had just passed beyond the insertion of the Wolffian ducts into the cloaca (Figure 2.2F) and were effacing during CS15 (36 days; Figure 2.3A-F). While the lateral folds were recognizable, the peritoneal cavity ("trough") reached down to the separation between hindgut and cloaca (asterisks in Figure 2.2), that is, to the lateral folds.

Starting in CS15 embryos, a transverse wedge of loose connective tissue extended distally that further separated the cloaca into a larger ventral component, the urogenital sinus, and a smaller dorsal component, the future anal pecten region (Figure 2.4). This wedge of loose connective tissue, which is known as "urorectal septum", only became recognizable after the lateral folds had separated the cloaca from the hindgut

to just distal of the insertion of the Wolffian ducts (Figure 2.2F). The insertion of the Wolffian ducts into the cloaca was a reliable landmark because it remained associated with segmental level 31-32 (S3-S4; Figure 2.5B). This landmark revealed that the apparent cranial migration of the entrance of the Wolffian ducts into the cloaca and, later, the urogenital sinus, was caused by a lack of growth of the cranial portion of the urogenital sinus between the entrance of the Wolffian ducts and the junction with the allantois (Figure 2.5C). The peritoneal trough inside the urorectal septum (asterisks in Figures 2.2 and 2.4) extended caudally from just distal to the entrance of the Wolffian ducts at 36 days (CS15) to halfway the distance between the entrance of the Wolffian ducts and the caudal tip of the urorectal septum at 41 days (CS17) and back again in the next 2 weeks (Figure 2.4).

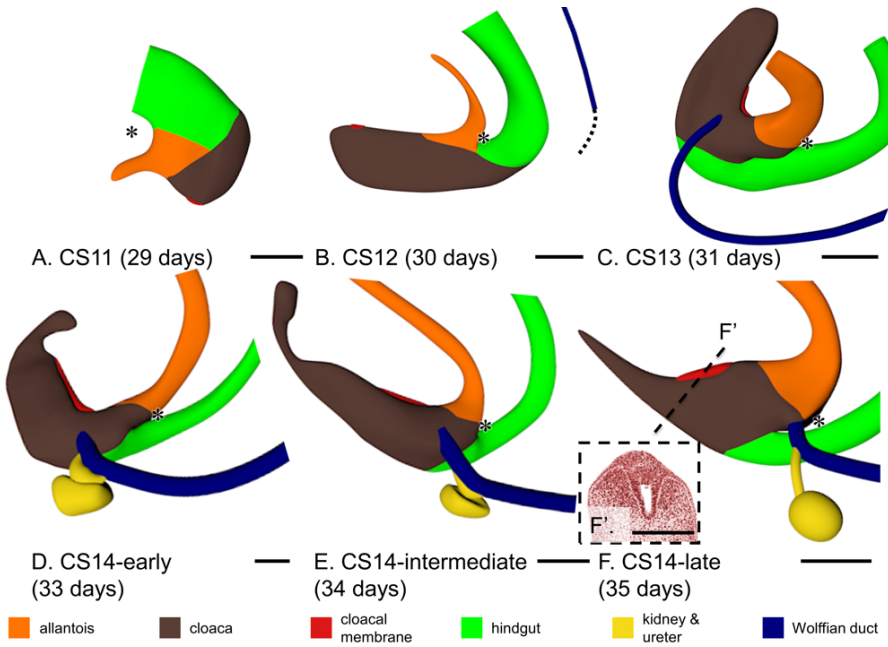

Figure 2.2 **Early phase of development of the cloacal region (CS11 – CS14). Left-sided views.** Cloaca (brown) and cloacal membrane (red) elongated in this period. Caudal to the cloacal membrane, the so-called "tailgut" was maximally developed at CS13 (panel C), narrowed during CS14 (panels D-F), and had disappeared at CS15 (Figure 2.4A). Wolffian ducts (dark blue) appeared at CS12 (panel B) and extended caudally (dotted line in panel B) to insert into the cloaca at CS13 (panel C). From CS14-early onwards (panels D-F), ureters and kidneys (yellow) were formed dorsolaterally on the Wolffian ducts just upstream of its insertion into the cloaca. The lateral folds separated the cranial part of the cloaca from the hindgut (green) between CS13 and CS14 (panels C-F; *cf.* Figure 2.3). Up to CS14-late, no urorectal septum was found because the peritoneal cavity extended up to the junction of hindgut and cloaca. Asterisks: most caudal part of peritoneal trough. Panel F' shows the appearance of the urethral plate in the ventral part of the cloacal membrane. Bar = 200 µm.

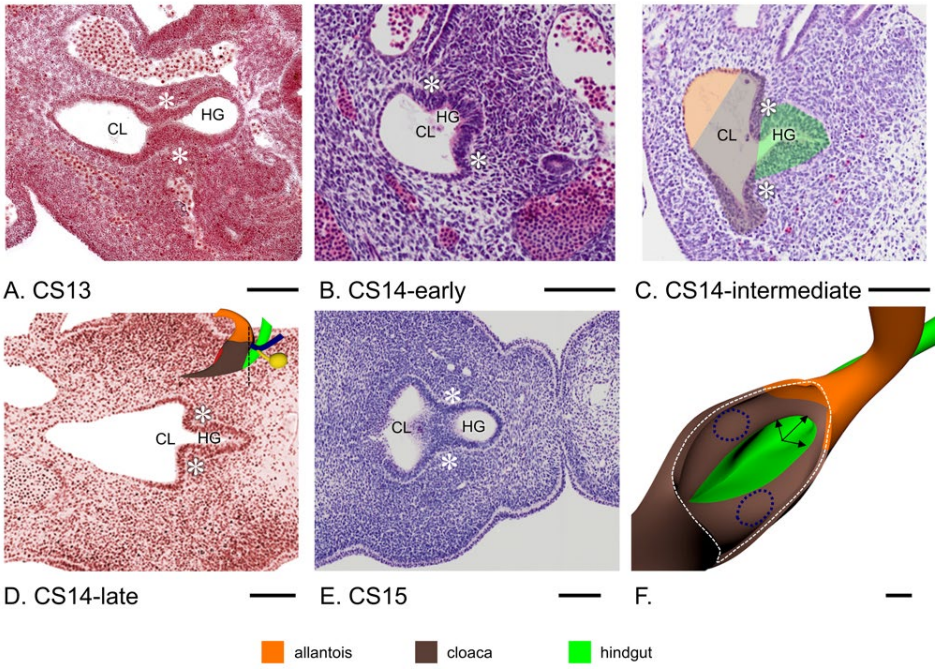

Figure 2.3 **The lateral fold.** The lateral folds (asterisks) demarcate the junction between the dorso-cranial part of the cloaca and hindgut between CS13 and CS14-late. Note that the folds are first identifiable as blunt ridges at CS13 (panel A) to become pronounced ridges that demarcate the transition between the narrow hindgut and the wide cloaca (panels B-D) and efface again in CS15 (panel E). Panel F shows a 3D perspective of the sharp-edged lateral folds at CS14-intermediate (arrows) between cloaca (brown) and hindgut (green) of the embryo shown in panel D. The position of the entrance of the Wolffian ducts is shown as dark blue dotted lines. Abbreviations: CL, cloaca; HG, hindgut. Bar = 100 µm.

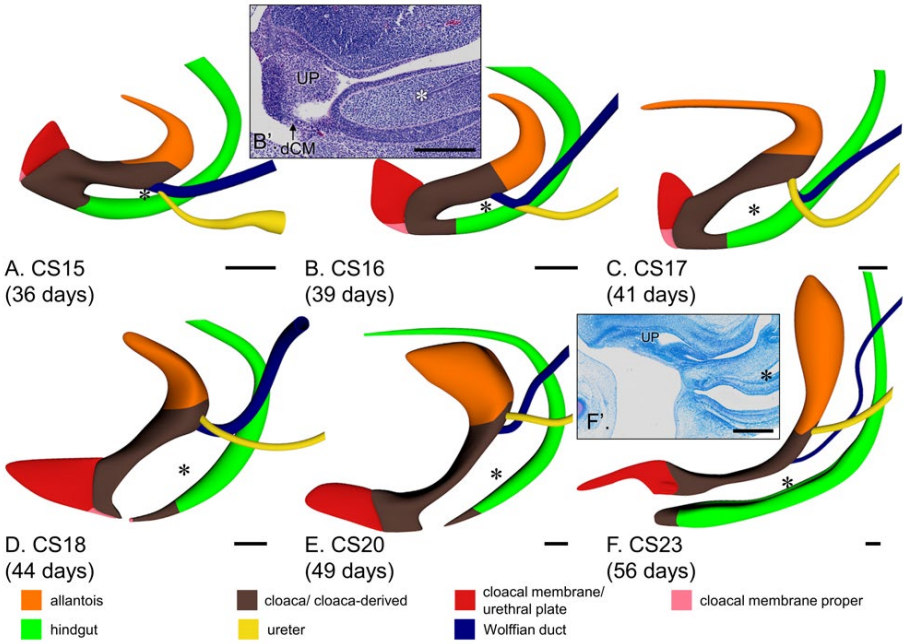

Figure 2.4 **Late phase of development of the cloacal region (CS15 – CS23).** Left-sided views aligned with respect to the caudal portion of the vertebral column. The cloaca resembled a U-shaped tube (panel A-C) with ventral urogenital and dorsal anorectal parts between CS15 and CS17, and the urorectal septum separating both parts. The urorectal septum consisted of loose mesenchyme (panels B' and F'). The caudal-most point of the peritoneal trough in its centre is indicated with asterisks. Note that the caudal tip of the urorectal septum and the peritoneal trough move caudally relative to the Wolffian ducts (panels A-E; *cf.* Figure 2.5B,D). The cloacal membrane consisted of a well-developed ventral urethral plate (UP; red) and a thin dorsal cloacal membrane proper (dCM; pink). The cloacal membrane proper did not grow between CS15 and CS17 (panels A-C) and ruptured at CS18 (panel D). Note the changing position of the cloaca due to the unfolding of the caudal body axis in panels A-D and its subsequent ventral extension concomitant with the growth of the genital tubercle (panels D-F). Bar = 200 µm.

Our description implies that the growth pattern of the cloacal region is complex. For that reason, we carried out measurements in our Amira reconstructions (Figure 2.5). The distance between the entrance of the Wolffian duct and the middle of the cloacal membrane (Figure 2.5C) increased linearly with time at ~10-fold the rate of the distance between the entrance of the Wolffian duct and the allantois. Since the Wolffian duct enters the cloaca near its centre at CS13 (Figure 2.2C), these measurements show that growth primarily occurred in the caudal part of the cloacal region. Taking into account the shorter path, the distance between the entrance of the Wolffian duct and the caudal tip of the urorectal septum increased at a similar rate as

that to the cloacal membrane (Figure 2.5D). The distance between the entrance of the Wolffian duct and the peritoneal trough first decreased (up to ~45 days or CS18) and then increased again (after 49 days CS20; Figure 2.5D). This complex growth pattern is described qualitatively in the previous paragraph and can be traced in Figures 2.2 and 2.4 by following the position of the asterisks. The distance between the caudal tip of the urorectal septum and the ventral tip of the urethral plate increased exponentially at the same rate as the embryonic body at large (Figure 2.5E). In contrast, the distance between the caudal tip of the urorectal septum and the dorsal end of the cloacal membrane decreased (Figure 2.5E), which reveals a large and distinct growth difference between the ventral and dorsal parts of the cloaca. Similarly, the distance between the caudal tip of the urorectal septum and the tail-fold did not increase until after 39 days. Thereafter, this distance increased exponentially like that to the ventral tip of the urethral plate, but with a ~1-week delay. The area of restricted growth in the cloaca, therefore, seems strictly limited to the dorsal cloaca. To confirm these data, we also determined the distance between segment 32 (S5) and the ventral tip of the cloaca on the one hand (exponential growth at a slightly higher rate than the embryonic body at large) and the caudal tip of the urorectal septum on the other hand (also exponential growth; Figure 2.5F), indicating that the growth of the vertebral column was not affected. In aggregate, these measurements show a more extensive growth in the caudal than cranial part of the cloaca and a much more extensive growth in the ventral than dorsal part. The area of highest growth is the genital tubercle. This tubercle becomes identifiable at CS14-late, is similar in shape at CS18 and CS20, but has clearly changed in shape by CS23 (Figure 2.6).

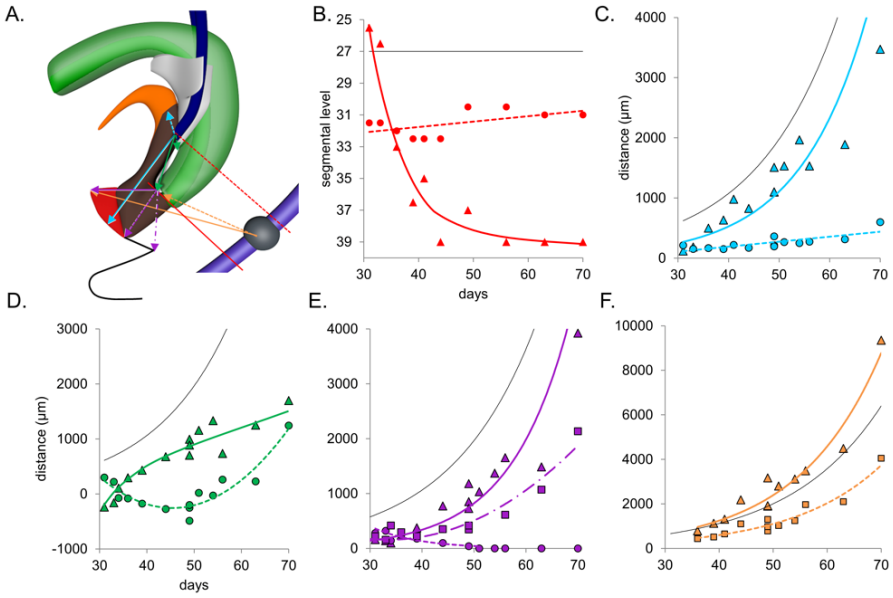

Figure 2.5 **Regional growth differences in the cloacal region**. Panel A shows the landmarks used to prepare panels B-F. Colours correspond to those in the respective graphs. The black line shows the position of the aortic bifurcation (panel B; *cf.* (Hikspoors et al., 2015)) or the temporal changes in greatest length of the embryo (divided by ten; panels C-F, *cf.* (O'Rahilly and Müller, 2010)). Panel B shows that the entrance of the Wolffian duct into the cloaca / urogenital sinus (dotted red line; R^2: 0.31) remained associated with segment 31-32 (S3-4), whereas the tip of the urorectal septum (drawn red line; R^2: 0.87) moved caudally to the level of the last coccygeal vertebra. Panels C and D show the cranio-caudal growth of the cloacal region. The dotted blue line in panel C (R^2: 0.62) shows the marginal increase in distance between the entrance of the Wolffian duct and the allantois, whereas the distance between the entrance of the Wolffian duct and the middle of the cloacal membrane (continuous blue line; R^2: 0.82) grew at a similar rate as the body at large (black line). The continuous green line in panel D (R^2: 0.90) shows that the caudal tip of the urorectal septum moved from above (negative values) to below (positive values) the entrance of the Wolffian duct between 30 and 40 days. The distance then increased more slowly. The dotted green line (R^2: 0.88) represents the distance between the entrance of Wolffian duct and the peritoneal trough. The biphasic shape of this measurement with an inflection at 50 days can also be deduced from the position of the asterisks in Figures 2.2 and 2.4. Panels E and F show the dorso-ventral growth of the cloacal region. The dotted purple line in panel E (R^2: 0.23) shows that the distance between the caudal tip of the urorectal septum and the cloacal membrane proper gradually declined, whereas the distance between the tip of the septum and the ventral tip of the urethral plate (drawn purple line; R^2: 0.90) increased concomitant with the growth rate of the embryo. The dash-dotted purple line in panel E (R^2: 0.92) shows that the distance between the tip of the septum and the tail-fold also increased, but with a delay of ~7 days (after CS20, the middle of the distance between the coccygeal tip and the anal sphincter was used instead of the tail-fold). Panel F shows the distances between the centre of S5 and the caudal limit of the hindgut mesenchyme (dotted orange line; R^2: 0.91) or the ventral tip of the mesenchyme of the genital tubercle (drawn orange line; R^2: 0.93). Both distances increase at a similar rate. Together with the dash-dotted line in panel E, these data show that the absence of growth in the dorsal cloaca is a very local phenomenon. To demonstrate that growth was exponential some of the curves are shown in Supplemental Figure S2.2 after logarithmic transformation of the Y-axis.

Ventral and dorsal parts of cloacal membrane

At the end of the 4th week (CS11 and CS12), the cloacal membrane was a thin, more or less circular structure on the ventral surface of the cloaca (Figure 2.2A). As the caudal end of the body curved (CS13 and CS14), the cloacal membrane elongated and divided into a ventral part that proliferated to form a solid epithelial mass, the so-called "urethral plate" (Figures 2.2F', 4B', 4F'; UP), and a thin dorsal part that represented the cloacal membrane proper (Figure 2.4B'; dCM). The apical part of the urethral plate was transiently covered on its caudal side with an ectodermal "epithelial tag" (Supplemental Figure S2.6; (van der Putte, 2004)). Both parts of the cloacal membrane and the epithelial tag elongated between CS15 and CS17 (Figure 2.4A-C). After CS18, the urethral plate continued to elongate, whereas the cloacal membrane proper did not grow and ruptured, starting at its centre at CS18 (Figure 2.4D-F). Similarly, the epithelial tag on the urethral plate regressed towards the apex of the tubercle between CS17 and CS20, and had disappeared at CS23. In the reconstructions, the epithelial tag is visible as the epithelial cover of the urethral plate (Supplemental Figure S2.6). Only the growth of the urethral plate, therefore, mirrored that of the genital tubercle.

Mesenchymal component in the cloacal region

The developmental changes in the distribution of dense and loose mesenchyme in the cloacal region are incompletely described. Dense mesenchyme included pericloacal mesenchyme (PCM, blue code) and hindgut mesenchyme (HGM; green code; Figure 2.7A), while loose mesenchyme occupied the remaining parts of the cloacal region, including the urorectal septum (Figure 2.7A). Dense PCM became identifiable on the sides of the cloaca in CS14-late embryos (Figure 2.7B). The bilateral PCMs expanded on the dorsocranial side of the urethral plate to form a single U-shaped "roof" on the cranial side of the genital tubercle at CS15 (Figure 2.7C). This pericloacal mesenchyme had also extended dorsally around the dorsal cloaca at CS20 (Figure 2.7E). A separate cuff of dense mesenchyme with a tapering end at the junction of hindgut and cloaca surrounded the hindgut in embryos older than 5 weeks (CS15; Figure 2.7B-F). Initially both areas of dense mesenchyme touched (CS15 and CS16; Figure 2.7C), but as the urorectal septum extended caudally, both areas became separated (CS18; Figure 2.7D,G), showing that the loose mesenchyme of the urorectal septum was not solely a midline structure, but also extended laterally. Because the PCM expanded dorsally to embrace the anorectal part of the cloaca in the 8th week (CS20-CS23; Figure 2.7E,F,H,I), PCM and HGM again became contiguous structures (Figure 2.7F). At the

same time, a shelf of dense mesenchyme, which formed in the ventral-most part of the urorectal septum (Figure 2.7H) began to expand ventrally between the surface ectoderm and the remaining part of the urethral plate (cf. Figure 2.6E and F, with appearance of surface epithelium on developing perineum in Figure 2.6F). At CS23, this structure could be identified as the spongious body (Figure 2.7I). At this stage the other components of the pericloacal mesenchyme became identifiable as separate anatomical structures (external anal sphincter and bulbospongious muscle, cavernous body, ischiocavernous muscle, and urethral sphincter; Figure 2.7I).

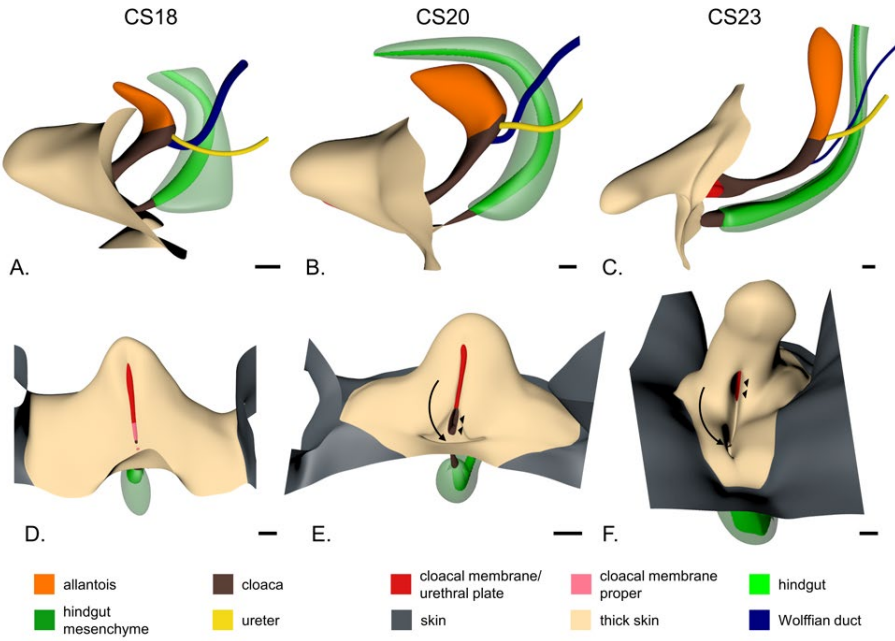

Figure 2.6 **The ectodermal cover of the cloacal region.** Panels A-C show left-sided views and panels D-F frontal views of CS18, 20 and 23 embryos, respectively. The shape of the genital tubercle was similar at CS18 (panels A and D) and 20 (panels B and E) but had changed at CS23 (panels C and F). The epithelium that covered the external genitals (sand-coloured) was markedly thicker than the more peripheral skin (dark grey). Further, note that a surface groove started to develop at CS20 (panels B and E) at the site of the ruptured cloacal membrane, which extended ventrally and became deeper in CS23 (panels C and F). The bottom of the groove in panels E and F contained the very narrow anorectal opening dorsally (arrow) and the wide urogenital opening ventrally (arrowheads). Bar = 200 µm.

Development of the cranial part of the urogenital sinus and allantois

The portion of the urogenital sinus cranial to the entrance of the Wolffian ducts grew much slower than the caudal portion. The allantois remained a tubular structure until it started to balloon at CS20 (7 weeks). Shortly after the Wolffian ducts inserted into the cloaca at CS13, the ureteric buds started to form on the dorsal side of the Wolffian ducts near their insertion into the cloaca (Figures 2.2D-F and 2.3A,B). The portion of the Wolffian ducts between the cloaca and the ureteric buds disappeared at CS17 (41 days), so that both ureters gained access to the urogenital sinus as well (Figure 2.4C). The entrance of the ureters into the urogenital sinus was first localized laterally (CS17) and gradually also cranially to the entrance of the Wolffian ducts, but remained within the domain of the epithelium of the cranial portion of the urogenital sinus. The insertions of the Wolffian ducts and ureters demarcate the trigone of the bladder (Figure 2.3D-F).

Development of the anorectum

After the cloacal membrane ruptured at CS18, the cone-shaped small dorsal part of the cloaca retained only a very narrow opening to the outside. From CS20 onwards, this opening connected with the funnel-like ectodermal structure known as the “anal pit”. In all our embryos, the connection was patent. The anorectum, therefore, derived from three different regions: the caudal hindgut, the dorsal cloaca, and the anal pit (Figure 2.6E,F). Up to CS15, the hindgut connected to the dorsal side of the cloaca forming the lateral folds as described above. After CS15, the hindgut only connected to the dorsal part of the cloaca. The boundary of hindgut and cloaca was marked by the distal end of the dense mesenchymal cuff (HGM) that surrounded the hindgut (Figure 2.7). The junction of dorsal cloaca and anal pit is characterized by the transition from pseudostratified to stratified squamous epithelium (Figures 2.4F’ and S2.3).

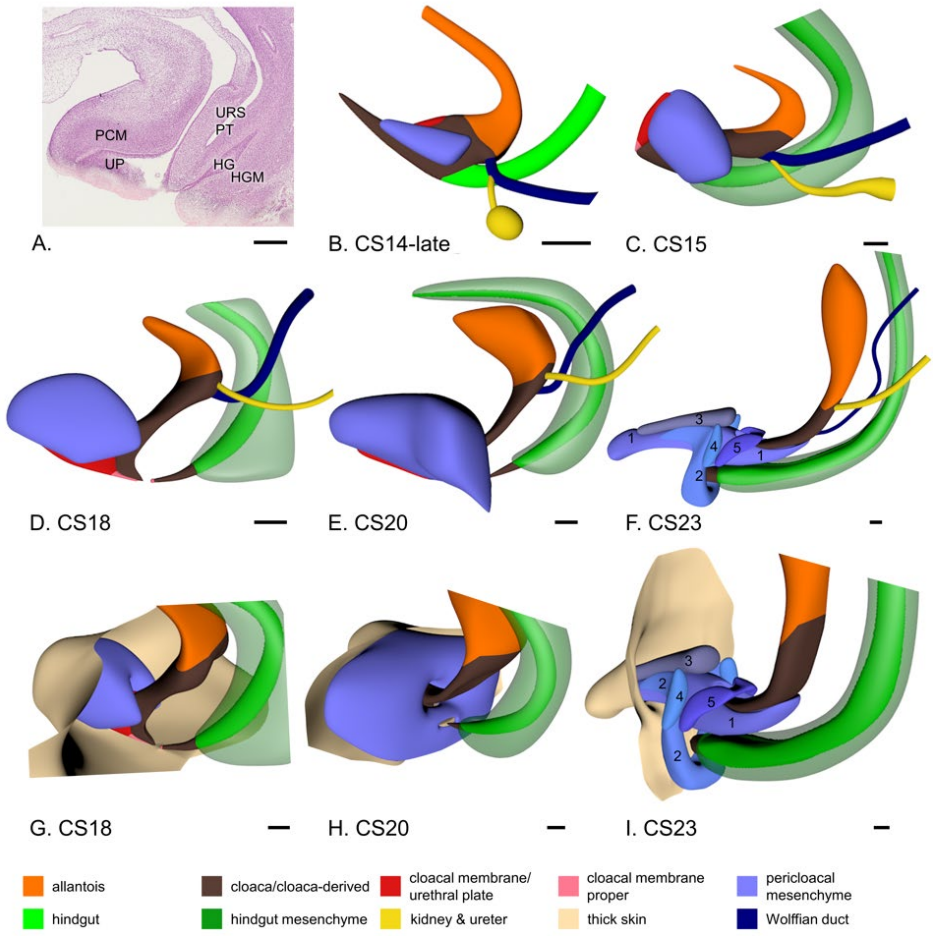

Figure 2.7 **Growth of mesenchymal masses in the cloacal region.** Panel A shows a sagittal section of the cloacal region of a CS20 embryo to show the differences between dense (e.g. the pericloacal mesenchyme (PCM)) and loose connective tissue (e.g. urorectal septum (URS)). Panels B-F show the 3D shape and location of the PCM (blue) and the hindgut mesenchyme (HGM; green) between CS14-late and CS23 (33-56 days). The PCM was first identifiable on both sides of the cloaca at CS14-late, extended ventrally and cranially to embrace the cranial side of the cloaca between CS15 and CS18, and extended dorsally embracing the caudal-most part of the cloaca after CS20. At CS23 (panels F and I), the components of the pericloacal mesenchyme had become identifiable: spongious body (1), external anal sphincter and bulbospongious muscle (2), cavernous body (3), ischiocavernous muscle (4), and urethral sphincter (5). The caudal end of the HGM coincided with the junction of hindgut (green) and cloaca (brown) from CS15 onwards (panels C-F; transparent green). Abbreviations: HG, hindgut; HGM, hindgut mesenchyme; PCM, pericloacal mesenchyme; PT, peritoneal trough; UP, urethral plate. Bar = 200 µm.

Discussion

We studied the development of the cloacal region to clarify the mechanism of cloacal subdivision and the fate of cloacal derivatives (Supplemental Figures S2.4-2.6). A pronounced difference in growth between the rapidly growing ventral and central areas, and the hardly growing cranial and dorsal areas produced separate urogenital and anorectal compartments in the cloacal lumen (Figure 2.8). Regressive development of the dorsal cloaca transformed the "end-to-end" connection of the hindgut and cloaca into an "end-to-side" connection during CS13 and CS14, with the lateral folds marking the junction of cloaca and hindgut during this transformation. The dorso-ventral difference in growth subsequently straightened the curved caudal body axis of the embryo and concomitantly extended the urorectal septum caudally. The subdivision of the cloacal membrane into a rapidly growing, thick urethral plate ventrally and a hardly growing, very thin membrane dorsally best represented the dorsoventral difference in growth. The cloacal membrane proper ruptured at CS18.

Mechanism of cloacal subdivision

The mechanism of cloacal subdivision has remained controversial with respect to origin and growth of the septum that separates its ventral urogenital and dorsal anorectal parts. Early studies emphasized the role of the lateral ("Rathke's") folds (Retterer, 1890, Reichel, 1893) or the frontal urorectal ("Tourneux's") septum (Tourneux, 1888). Unfortunately, the descriptions of the shape of the lateral folds and timing of the developmental appearance of folds and urorectal septum were sufficiently diffuse to induce textbook writers to combine both concepts (Carlson, 2014, Schoenwolf et al., 2015, Moore et al., 2016). Our present study, therefore, defined the lateral folds and showed that their temporary presence marks a changing attachment of the hindgut to the cloaca. When the cloaca forms between 28-30 days (CS10-12), it is a smooth, caudal extension of the hindgut with an "end-to-end" type of junction. During the next few days (CS13-14-late), this connection transformed into an "end-to-side" type of junction and its position changed from cranial to dorsal relative to the cloaca (cf. Figure 2.2 in (Kluth et al., 1995)). We consider this change in position of the connection of hindgut and cloaca as the first sign of dorsal cloacal regression.

The dorsoventral difference in growth of cloaca and surrounding mesenchyme has also been associated with the caudal extension of the urorectal septum (van der Putte, 2004, Huang et al., 2016). The combination of lengthening of the body axis with an

increasingly convex curvature (see also (Müller and O'Rahilly, 2004) suggests an initial predominance of dorsal growth (for the consequence of insufficient dorsal growth at this stage, see (van de Ven et al., 2011)). However, the subsequent uncurling of the body axis in the 6th week (CS14-18; see also (Paidas et al., 1999)) indicates a change to predominantly ventral growth. This regional change in growth is important, because some claim that the urorectal septum actively descends caudally ("active" theory; (Pohlman, 1911, Stephens, 1988)), whereas others consider the growth of the urorectal septum and, hence, the septation of the cloaca as merely the result of the differential dorsoventral growth in the cloacal region ("passive" theory; (van der Putte, 2004, Xu et al., 2012, Tschopp et al., 2014, Matsumaru et al., 2015, Huang et al., 2016)). To distinguish between both conjectures, the entrance of the Wolffian ducts into the cloaca / urogenital sinus is a reliable landmark, because its position is fixed to segments 31-32 (vertebrae S3-4). Our measurements (Figure 2.5) show that the cranial and dorsal areas of the cloaca hardly grow, whereas the ventrocaudal area, including the surrounding cloacal mesenchyme, grows at a similar rate as the embryo at large. Our measurements in human embryos, therefore, support the passive theory. Other convincing non-quantitative arguments in favour of pronounced regional growth differences in the cloaca are disappearance of the tailgut, apoptosis in the dorsal cloaca, absence of growth of the dorsal cloacal membrane and pronounced growth of the ventral part of the cloacal membrane (urethral plate) (van der Putte, 1986, Nievelstein et al., 1998, van der Putte, 2004, Sasaki et al., 2004, Matsumaru et al., 2015)). Furthermore, the urorectal septum consists of loose rather than dense mesenchyme that one usually associates with local cell proliferation.

Fate of the cloaca

The topographic distribution of the regional differences in growth rate of the cloaca determines the remodelling of the cloaca. Figure 2.8 shows that the rapidly growing central part of the cloaca is initially sandwiched between slowly growing cranial (future vesical trigone) and dorsal parts (future anal pecten). As a result, the Wolffian ducts appear to move cranially and dorsally on the surface of the cloaca, as was earlier observed in mice (Matsumaru et al., 2015). Similarly, the anorectal part of the cloaca becomes a progressively smaller part due to the difference in growth of the dorsal and ventral parts of the cloaca.

Cell replication rates in the cloacal wall and its surrounding mesenchyme appear similar in human (Nebot-Cegarra et al., 2005) and mouse embryos (Matsumaru et al.,

2015), but rapid proliferation may continue longer in mesenchyme than epithelium (Matsumaru et al., 2015). Observed regional differences in growth, therefore, point to regional accumulation of extracellular matrix or regional differences in cell death. In early mouse embryos (up to CS14) apoptosis in the cloacal epithelium is prevalent ventrally and dorsally, with an almost apoptosis-free area in the centre, while apoptosis in the surrounding mesenchyme concentrates around the anorectal part of the cloaca. Thereafter, apoptosis is mainly seen in the mesenchyme of the urorectal septum caudal to the Wolffian ducts (Batourina et al., 2005, Matsumaru et al., 2015, Sasaki et al., 2004), the epithelium of the caudal tip of the urorectal septum and the dorsal part of the cloacal membrane (Ng et al., 2014).

Fate of cloacal membrane and pericloacal mesenchyme

The ventrocaudal part of the cloaca, including the ventral part of the cloacal membrane and the pericloacal mesenchyme, represents the expanding part in the cloacal region. Concomitant with the ventral expansion of the genital tubercle, the length of the cloacal membrane increases during CS14 (33-35 days; Figure 2.2). The expanding and non-expanding parts of the cloacal membrane can be distinguished in sections and reconstructions from CS15 onwards, when the ventral part of the membrane not only increases in length, but also in height (Figure 2.4; (Ludwig, 1965, Penington and Hutson, 2002b, Hynes and Fraher, 2004, Li et al., 2015)), with most of the epithelium being endodermal (van der Putte, 2004, Seifert et al., 2008). Due to the expansion of the urethral plate the connection between the relatively wide lumen of the lower urogenital sinus and the part of the cloacal lumen overlying the thin dorsal part of the cloacal membrane is narrow and known as “cloacal duct” (Figure 650 in (Felix, 1912)). The centre of the thin cloacal membrane ruptures at CS18 (44 days), with often a dorsal remnant (“anal membrane”) temporarily covering the anorectal outlet remaining (Ludwig, 1965, Nievelstein et al., 1998). Growth of the pericloacal mesenchyme depends on Sonic Hedgehog secretion by the endodermal cloacal epithelium (Haraguchi et al., 2007, Seifert et al., 2009, Lin et al., 2009). Dense masses of pericloacal mesenchyme become identifiable bilaterally of the cloaca at CS14-late (35 days), expand cranially to bridge the urethral plate (at CS18; 44 days), and then dorsally to surround urogenital sinus (CS20; 49 days), anorectal junction and anal pit (CS23; 56 days). The portion of the dense pericloacal mesenchyme between urogenital sinus and anorectal junction began to expand ventrally in the 8th week to form the penile urethra (cf. (Seifert et al., 2009)).

Fate of the dorsal cloaca

The dorsal part of cloaca, including the dorsal cloacal membrane, is, in contrast, a "non-growing" area (Figure 2.5E; cf. (van der Putte, 1986, van der Putte, 2004, Huang et al., 2016)). The decline is visible qualitatively: the narrowing tailgut impresses as a transient stage in the regression of the dorsocaudal cloaca during CS14 (33-35 days), the dorsal cloacal membrane proper thins and ruptures after CS18 (44 days), and the dorsal cloaca (developing anal pecten) becomes a narrow, cone-shaped structure with a very small opening between CS17 and CS20 (41-49 days; Figure 2.4) without any dense pericloacal mesenchyme surrounding it until CS20 (49 days; Figure 2.7; (van der Putte, 1986)). Microscopically, the dorsocaudal area is characterized by a high prevalence of apoptotic cells between CS14 and CS20 (~34-49 days; (Sasaki et al., 2004, Ng et al., 2014, Matsumaru et al., 2015)). Interestingly, the area affected by the lack of growth is also limited dorsally: the area of the tail-fold does not grow up to CS18 (41 days; Figure 2.5E), but thereafter the (pre-)vertebral sacral and coccygeal tissues exhibit a similar growth rate as the ventral part of the cloaca (Figure 2.5E,F). The hindgut and its surrounding dense mesenchymal cuff, the future smooth-muscle layer of the rectum, also appear to expand normally (the caudal end of the mesenchymal cuff can serve as a reliable marker for junction between the hindgut and anorectal part of the cloaca (van der Putte and Neeteson, 1983)). Until CS18 (44 days), the dense pericloacal mesenchyme flanks the urethral plate as urethral folds, but by expanding dorsally around the urogenital and anal openings during the next 2 weeks, these urethral folds and the groove they embrace merge with the perianal folds and anal pit (Figure 2.4D-F). The endoderm of the hindgut and that of the dorsal cloaca, and the ectoderm of the anal pit are easily distinguishable in histological sections and three-dimensional models thereof (Fritsch et al., 2007, Yamaguchi et al., 2008). These zones can be traced to the epithelium of the formed rectum (simple columnar epithelium), the anal pecten (non-keratinized stratified squamous epithelium), and the perianal skin (keratinized stratified squamous epithelium), respectively.

Development of bladder and trigone

Apoptosis in the epithelium of the distal Wolffian duct and cloaca is necessary for insertion of the Wolffian duct at CS13 (31 days; (Hoshi et al., 2018)), while apoptosis in the common nephric duct separates the entrance of the Wolffian duct and ureter into the urogenital sinus between CS15 and CS20 (36-49 days) to establish the vesical trigone (Batourina et al., 2005, Matsumaru et al., 2015). Further support for this

mechanism comes from tissue-recombination experiments of trigonal epithelium and foetal urogenital-sinus mesenchyme in mice, which demonstrate that trigonal epithelium derives from urogenital endoderm and not from the mesodermal common nephric duct (Tanaka et al., 2010), while the Cre-lox genetic recombination technique has shown that the underlying smooth muscle forms from bladder smooth muscle (Viana et al., 2007). The bladder fundus develops from the intra-abdominal portion of the allantois (van der Putte, 2006, Georgas et al., 2015). The fundus develops a muscular wall and begins to expand after the trigone has formed at CS20 (Figure 2.4), and extends, flanked by both umbilical arteries, as an intraperitoneal structure up to the umbilical ring to transform into a retroperitoneal structure only after the 4th month (Cunéo and Veau, 1899).

Fate of the peritoneal trough

The position of the "deepest" (most caudal) part of the peritoneal trough between urogenital sinus and hindgut first descended caudally after CS13 to touch the developing levator ani muscle at CS18 and CS20, and then ascended again to just caudal of the junction of the Wolffian ducts with the urogenital sinus (Figures 2.2, 2.4, and 2.5D). In rodents, the configuration as seen between CS18 and CS20 persists into adult life (Treuting and Dintzis, 2012, Navarro et al., 2017), so that the caudal boundary of the peritoneal trough in human CS18-20 embryos (and adult rodents) is apparently localized more caudally than in adult humans (~12 cm above the pelvic floor). The trough disappears due to a widening of the dorsal mesentery from caudal to cranial between CS20 and CS23 that is accompanied by an increase in the distance between the levator ani muscle and the deepest point of the trough (our unpublished observations). In fetuses of 9-10 weeks the deepest point of the prerectal peritoneal pouch is located in the plane through S3 and symphysis (Fritsch, 1988), that is, at the same location as in the adult. These topographic relations are also found between 22 and 35 weeks of fetal life (Saguintaah et al., 2002). The only structure that can explain the transition of the configuration at 6 weeks to that at 9-10 weeks is "Denonvilliers' fascia". Based on a single embryo Cunéo and Veau (Cunéo and Veau, 1899) first proposed that Denonvilliers' fascia developed from the obliterated peritoneal trough by adhesion and fusion of its peritoneal walls. Their model was subsequently vindicated (Tobin and Benjamin, 1945, Uhlenhuth et al., 1948). In agreement, pelvic surgeons occasionally report peritoneal troughs that extend to the pelvic floor in neonates

(Uhlenhuth et al., 1948) or coelomic remnants on the pelvic floor in adults (Heald and Moran, 1998). The fascia as such develops only after birth (Kraima et al., 2015).

Implications for cloacal malformations

Cloacal malformations are still poorly understood and classifications tend to emphasize anatomical or clinical rather than developmental aspects (Holschneider et al., 2005). Anorectal malformations are often associated with caudal regression. In rodents, deficiency of homeobox genes like Cdx family members and an excess of retinoic acid can, acting via inhibition of WNT signalling, both cause dosage-dependent caudal vertebral and urorectal defects (Padmanabhan, 1998, van de Ven et al., 2011). Deficiency in SHH signalling in the caudal endoderm causes, independently of CDX, dosage-dependent inhibition of cloacal development (Mo et al., 2001). Interestingly, the dorsal (anorectal) part of the cloaca appears to be more sensitive to SHH deficiency than the ventral, urogenital part (Runck et al., 2014). The separate roles of the homeobox genes and SHH may explain the weak correspondence between the type of anorectal malformation and pelvic floor development in human anorectal malformations (Smith and Stephens, 1988, de Vries, 1988), and why striated pelvic-floor muscles are nearly always present if development of the sacrum is not affected (Wilkinson, 1972).

We have identified differential growth of the ventral and dorsal parts of the cloaca as a prominent feature of normal development between 4.5 and 7 weeks of development. Its onset coincides with the switch from predominant growth in the dorsal part of the caudal embryo (resulting in the curling-up of the caudal body axis) to growth in the ventral part of the caudal embryo (resulting in straightening of the caudal body axis; Figure 2.1). The near absent growth of the dorsal cloaca becomes manifest at CS14 with transformation of the caudal cloaca into the tailgut, continues with disappearance of the tailgut at CS15, and results in a similar size and shape of dorsal cloaca and cloacal membrane between CS15 and CS20, with the weak middle portion of the cloacal membrane normally rupturing at CS18 (the dorsal-most portion of the cloacal membrane proper persists temporarily as the “anal membrane” (our observations in an CS18-early embryo; (Fritsch et al., 2007, van der Putte, 2009)) Too little or absent regressive development of the dorsal cloaca results in its persistence. This group of malformations is phenotypically characterized by more extensive development of the dorsal portion of the cloacal membrane proper (the portion corresponding to the anal membrane) and its surrounding mesenchyme so that, with

increasing severity of the malformation the anal opening, becomes positioned more ventrally on the perineum and then more cranially on the urogenital sinus (van der Putte and Neeteson, 1984, van der Putte, 1986, van der Putte, 2006). Due to the strengthening of the dorsal part of the cloacal membrane proper, the abnormally localized anal opening is smaller or does not form, but the musculature surrounding the anorectum follows its change in topographic position, at least in hereditary pig models (van der Putte and Neeteson, 1984, Lambrecht and Lierse, 1987). Too much regression of the dorsal cloaca leads, on the other hand, to stenosis or atresia of the anorectal junction (van der Putte, 1986, Nievelstein et al., 1998, Fritsch et al., 2007) and reportedly insufficient development of the internal anal sphincter (Fritsch et al., 2007).

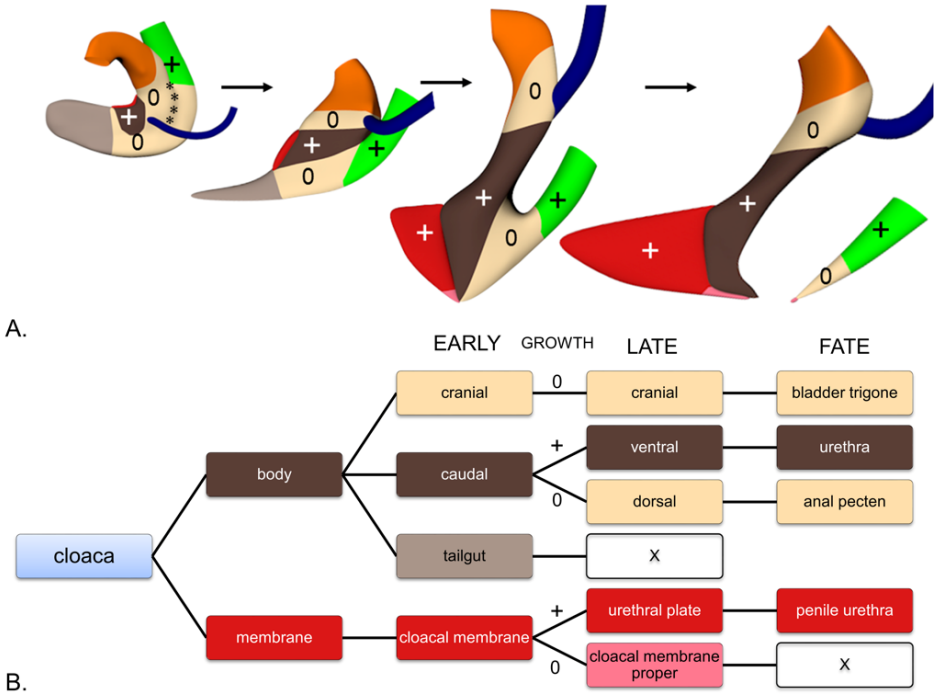

Figure 2.8 **Proposed mechanism of cloacal subdivision and the fate of the cloaca.** Panel A shows the global distribution of "growing" and "non-growing" zones in the cloaca of CS13, CS14-late, CS15, and CS18 embryos. Initially, the non-growing zone is located in the cranial and dorsal portions of the cloaca and surround the ventral (central) growing zone. Growth in the ventral portion changes the shape of the cloaca and eventually mediates the separation into urogenital and anal compartments. Panel B shows the fate of the cloaca in 3 phases: early (CS11-14), late (CS15-18) and definitive (fate). The colour codes in panels A and B correspond. Symbols: +, growing; 0, non-growing; X, disappear.

Conclusion

The subdivision of the cloaca appears to be based on differential growth of the "growing" ventral (central) and "non-growing" craniodorsal parts of the cloacal region. The growing central zone is initially sandwiched between the non-growing zones, but eventually separates the urogenital and anorectal compartments and forms the genital tubercle.

Supplemental figures

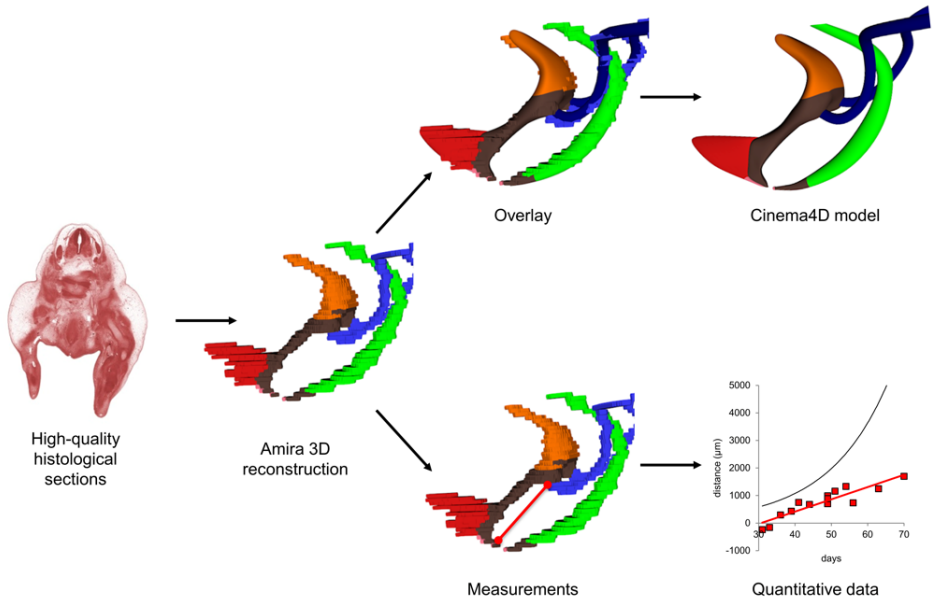

Figure S2.1 Brief procedure of 3D analysis.

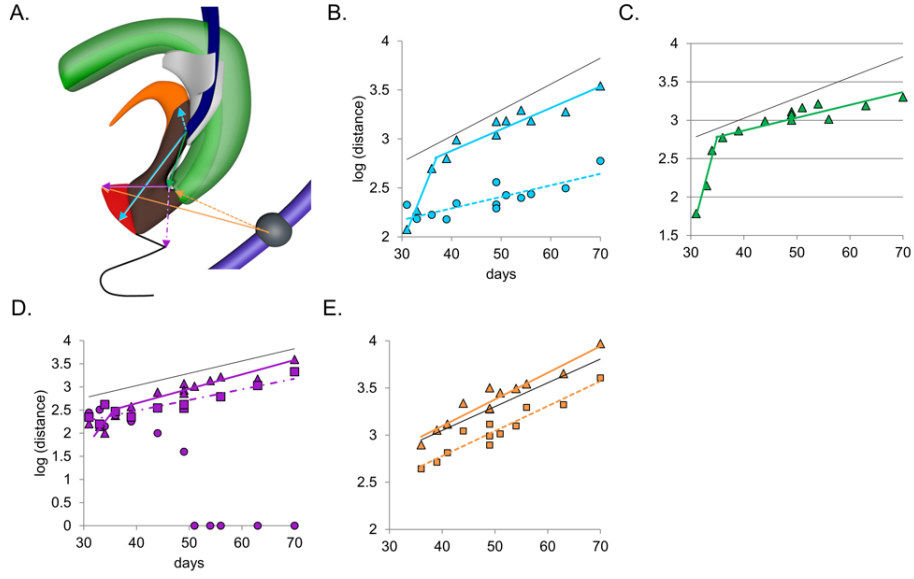

Figure S2.2 Semilogarithmic plots of growth in the cloacal region. Colour codes and line qualities correspond to those in Figure 2.5.

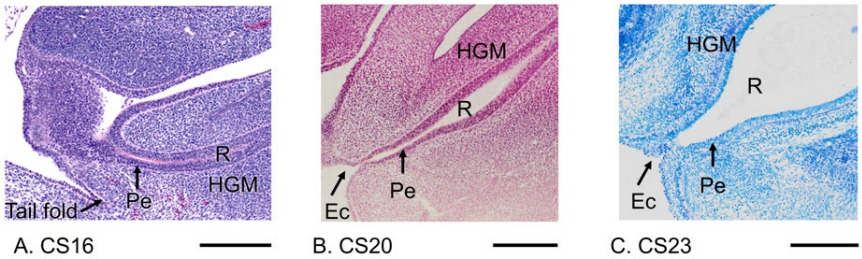

Figure S2.3 **Zonation of anorectal canal.** The three distinct zones in the anorectal canal are defined by different epithelia. The rectum (R) is lined by pseudostratified epithelium and surrounded by dense mesenchyme (HGM), the anal pecten (Pe) by pseudostratified epithelium without HGM, and the ectodermal anal pit (Ec) by stratified squamous epithelium. Bar = 200 µm.

Figure S2.4 **3D pdfs of the cloacal region from CS11 – CS14.**
Figure S2.5 **3D pdfs of the lateral folds from CS13 – CS14.**
Figure S2.6 **3D pdfs of the cloacal region from CS15 – CS23.**

Note! The interactive 3D-PDFs of the Supplemental Figures can be found in the digital version of the thesis on the USB stick, or directly downloaded from the journal website.

References

Batourina E, Tsai S, Lambert S, et al. (2005) Apoptosis induced by vitamin A signaling is crucial for connecting the ureters to the bladder. *Nat Genet,* 37, 1082-1089.

Carlson BM. (2014) *Human embryology and developmental biology,* Philadelphia, Saunders-Elsevier.

Cunéo B, Veau V. (1899) De la signification morphologique des aponévroses périvésicales. *J Anat Physiol,* 35, 235-245.

De Vries PA. (1988) High, intermediate, and low anomalies in the female. *Birth Defects Orig Artic Ser,* 24, 73-98.

Felix W. (1912) The development of the urinogenital organs. *In:* KEIBEL, F. & MALL, F. P. (eds.) *Manual of human embryology.* Philadelphia: J.B. Lippincott Co., 752-979.

Fritsch H. (1988) Developmental changes in the retrorectal region of the human fetus. *Anat Embryol (Berl),* 177, 513-22.

Fritsch H, Aigner F, Ludwikowski B, et al. (2007) Epithelial and Muscular Regionalization of the Human Developing Anorectum. *Anat Rec (Hoboken),* 290, 1449-1458.

Georgas KM, ArmstrongJ, Keast J R, et al. (2015) An illustrated anatomical ontology of the developing mouse lower urogenital tract. *Development,* 142, 1893-1908.

Haraguchi R, Motoyama J, Sasaki H, et al. (2007) Molecular analysis of coordinated bladder and urogenital organ formation by Hedgehog signaling. *Development,* 134, 525-533.

Heald RJ, Moran BJ. (1998) Embryology and anatomy of the rectum. *Semin Surg Oncol,* 15, 66-71.

Hikspoors JP, Soffers JH, Mekonen HK, et al. (2015) Development of the human infrahepatic inferior caval and azygos venous systems. *J Anat,* 226, 113-125.

Holschneider A, Hutson J, Peña A, et al. (2005) Preliminary report on the International Conference for the Development of Standards for the Treatment of Anorectal Malformations. *J Pediatr Surg,* 40, 1521-1526.

Hoshi M, Reginensi A, Joens MS, et al. (2018(Reciprocal Spatiotemporally Controlled Apoptosis Regulates Wolffian Duct Cloaca Fusion. *J Am Soc Nephrol,* 29, 775-783.

Huang YC, Chen F, Li X. (2016) Clarification of mammalian cloacal morphogenesis using high-resolution episcopic microscopy. *Dev Biol,* 409, 106-113.

Hynes PJ,& Fraher JP. (2004) The development of the male genitourinary system: II. The origin and formation of the urethral plate. *Br J Plast Surg,* 57, 112-121.

IKebukuro K, Ohkawa H. (1994) Three-dimensional analysis of anorectal embryology. *Pediatr Surg Int,* 9, 2-7.

Kluth D, Hillen M, Lambrecht W. (1995) The principles of normal and abnormal hindgut development. *J Pediatr Surg,* 30, 1143-1147.

Kluth D, Fiegel HC, Geyer C, Mryzger R. (2011) Embryology of the distal urethra and external genitals. *Semin Pediatr Surg,* 20, 176-187.

Kraima AC, West NP, Treanor D, et al. (2015) Whole mount microscopic sections reveal that Denonvilliers' fascia is one entity and adherent to the mesorectal fascia; implications for the anterior plane in total mesorectal excision? *Eur J Surg Oncol,* 41, 738-45.

Lambrecht W, Lierse W. (1987) The internal sphincter in anorectal malformations: morphologic investigations in neonatal pigs. *J Pediatr Surg,* 22, 1160-8.

Li, Y, Sinclair A, Cao M, et al. (2015) Canalization of the Urethral Plate Precedes Fusion of the Urethral Folds during Male Penile Urethral Development: The Double Zipper Hypothesis. *J Urol,* 193, 1353-1360.

Lin C, Yin Y, Veith GM, et al. (2009) Temporal and spatial dissection of Shh signaling in genital tubercle development. *Development,* 136, 3959-3967.

Lidwig KS. (1965) Über die Beziehungen der Kloakenmembran zum Septum urorectale bei menschlichen Embryonen von 9 bis 33 mm SSL. *Z Anat Entwicklungsgesch,* 124, 401-413.

MatsumaruD, Murashima A, Fukushima J, et al. (2015) Systematic stereoscopic analyses for cloacal development: The origin of anorectal malformations. *Sci Rep,* 5, 13943.

Mo R, Kim JH, Zhang J, et al. (2001) Anorectal Malformations Caused by Defects in Sonic Hedgehog Signaling. *Am J Pathol,* 159, 765-774.

Moore KL, Persaud TV, Torchia MG. (2016) *The developing human : clinically oriented embryology,* Philadelphia, Elsevier.

Müller F, O'Rahilly R. (2004) The Primitive Streak, the Caudal Eminence and Related Structures in Staged Human Embryos. *Cells Tissues Organs,* 177, 2-20.

Navarro M, Rubertie J, Carretero A, Nacher V, Dominguez E. (2017) Digestive tract. *In:* RUBERTE, J., CARRETERO, A. & NAVARRO, M. (eds.) *Morphological mouse phenotyping: anatomy, histology and imaging.* Amsterdam: Elsevier, 89-146.

Nebot-Cegarra J, Fabregas PJ, Sanchez-Pérez I. (2005) Cellular proliferation in the urorectal septation complex of the human embryo at Carnegie stages 13–18: a nuclear area-based morphometric analysis. *J Anat,* 207, 353-364.

Ng RC, Matsumaru D, Ho AS, et al. (2014) Dysregulation of Wnt inhibitory factor 1 (Wif1) expression resulted in aberrant Wnt-beta-catenin signaling and cell death of the cloaca endoderm, and anorectal malformations. *Cell Death Differ,* 21, 978-89.

Nievelstein RA, Van der Werff JF, Verbeek FJ, Valk J, Vermeij-Keers C. (1998) Normal and abnormal embryonic development of the anorectum in human embryos. *Teratology,* 57, 70-8.

O'Rahilly R, Muller F. (2003) Somites, Spinal Ganglia, and Centra. *Cells Tissues Organs,* 173, 75-92.

O'Rahilly R, Müller F. (2010). Developmental Stages in Human Embryos: Revised and New Measurements. *Cells Tissues Organs,* 192, 73-84.

Padmanabhan R. (1998) Retinoic acid-induced caudal regression syndrome in the mouse fetus. *Reprod Toxicol,* 12, 139-151.

Paidas CN, Morreale RF, Holoski KM, Lund RE, Hutchins GM. (1999) Septation and differentiation of the embryonic human cloaca. *J Pediatr Surg,* 34, 877-884.

Penington EC, Hutson JM. (2002a) The cloacal plate: the missing link in anorectal and urogenital development. *BJU Int,* 89, 726-732.

Penington EC, Hutson JM. (2002b) The urethral plate – does it grow into the genital tubercle or within it? *BJU Int,* 89, 733-739.

Pohlman AG. (1911) The development of the cloaca in human embryos. *Am J Anat,* 12, 1-26.

Pooh RK, Shiota K, Kurjak A. (2011) Imaging of the human embryo with magnetic resonance imaging microscopy and high-resolution transvaginal 3-dimensional sonography: human embryology in the 21st century. *Am J Obstet Gynecol,* 204, 77.e1-77.e16.

Quan BQ, Beasley SW, Williams AK, Frizelle F. (2000) DOES THE URORECTAL SEPTUM FUSE WITH THE CLOACAL MEMBRANE? *J Urol,* 164, 2070-2072.

Rathke H. (1832) *Abhandlungen zur Bildungs- und Entwicklungsgeschichte des Menschen und der Thiere 1. Theil,* Leipzig, Vogel.

Reichel P. (1893) Die Entwicklung der Harnblase und Harnröhre. *Phys-Med Gesell zu Würzburg,* 27, 1-41.

Reichmann S, Lewin T. (1971) The development of the lumbar lordosis. *Arch orthop Unfall-Chir,* 69, 275-285.

Retterer E. (1890) Sur l'origine et l'evolution de la region ano-genitale des mammiferes. *J Anat Physiol,* 26, 126-216.

Rinck LA, Mehtod A, Bischoff A, et al. (2014) Defining the molecular pathologies in cloaca malformation: similarities between mouse and human. *Dis Model Mech,* 7, 483-493.

Saguintaah M, Couture A, Veyrac C, Baud C, Quere MP. (2002) MRI of the fetal gastrointestinal tract. *Pediatr Radiol,* 32, 395-404.

Sasaki C, Yamaguchi K, Akita K. (2004) Spatiotemporal distribution of apoptosis during normal cloacal development in mice. *Anat Rec A Discov Mol Cell Evol Biol,* 279A, 761-767.

Schoenwolf GC, Bleyl SB, Brauer PR, Francis-West PH. (2015) *Larsen's human embryology,* Philadelphia, Elsevier/Churchill Livingstone.

Seifert AW, Harfe BD, Cohn MJ. (2008) Cell lineage analysis demonstrates an endodermal origin of the distal urethra and perineum. *Dev Biol,* 318, 143-152.

Seifert AW, Bouldin CM, Choi KS, Harfe BD, Cohn MJ. (2009) Multiphasic and tissue-specific roles of sonic hedgehog in cloacal septation and external genitalia development. *Development,* 136, 3949-3957.

Smith ED, Stephens FD. (1988) High, intermediate, and low anomalies in the male. *Birth Defects Orig Artic Ser,* 24, 17-72.

Soffers JH, Hikspoors JP, Mekonen HK, Koehler SE, Lamers WH. (2015) The growth pattern of the human intestine and its mesentery. *BMC Dev Biol,* 15, 31.

Stephens FD. (1988) Embryology of the cloaca and embryogenesis of anorectal malformations. *Birth Defects Orig Artic Ser,* 24, 177-209.

Tanaka ST, Ishi, K, Demarco RT, et al. (2010) Endodermal origin of bladder trigone inferred from mesenchymal-epithelial interaction. *J Urol,* 183, 386-91.

Tobin CE, Benjamin JA. (1945) Anatomical and surgical restudy of Denonvilliers' fascia. *Surg Gynec Obst,* 80, 373-388.

Tourneux F. (1888) Sur les premiers developpements du cloaque du turbercule genital et de l'anus chez l'embryon de mouton. *J Anat Physiol,* 24, 503-517.

Treuting PM, Dintzis SM. (2012) Lower gastrointestinal tract. *In:* TREUTING, P. M. & DINTZIS, S. M. (eds.) *Anatomy and Histology – a mouse and human atlas.* Amsterdam: Academic Press, 177-192.

Tschopp P, Sherratt E, Sanger TJ, et al. (2014) A relative shift in cloacal location repositions external genitalia in amniote evolution. *Nature,* 516, 391.

Uhlenhuth E, Wolfe W, Smith E, Middleton E. (1948) The rectogenital septum. *Surg Gynec Obst,* 86, 148-163.

Van de Ven, C., Bialecka, M., Neijts, R., et al. 2011. Concerted involvement of Cdx/Hox genes and Wnt signaling in morphogenesis of the caudal neural tube and cloacal derivatives from the posterior growth zone. *Development,* 138, 3859.

Van der Putte SC, Neeteson FA. (1983) The normal development of the anorectum in the pig. *Acta Morphol Neerl Scand,* 21, 107-32.

Van der Putte SC, Neeteson FA. (1984) The pathogenesis of hereditary congenital malformations of the anorectum in the pig. *Acta Morphol Neerl Scand,* 22, 17-40.

Van der Putte SC. (1986) Normal and abnormal development of the anorectum. *J Pediatr Surg,* 21, 434-440.

Van der Putte SC. (2004) *The development of the perineum in the human: a comprehensive histological study with a special reference to the role of the stromal components,* New York, Springer.

Van der Putte SC. (2006) Anal and Ano-Urogenital Malformations: A Histopathological Study of "Imperforate Anus" with a Reconstruction of the Pathogenesis. *Pediatr Dev Pathol,* 9, 280-296.

Van der Putte SC. (2009) The development of the human anorectum. *Anat Rec (Hoboken),* 292, 951-4.

Van der Werff JF, Nievelstein RA, Brands E, Luijsterburg AJ, Vermeij-Keers C. (2000) Normal development of the male anterior urethra. *Teratology,* 61, 172-183.

Viana R, Batourina E, Huang H, et al. (2007) The development of the bladder trigone, the center of the anti-reflux mechanism. *Development,* 134, 3763-3769.

Wilkinson AW. (1972) Congenital anomalies of the anus and rectum. *Archives of Disease in Childhood - Fetal and Neonatal Edition,* 47, 960-969.

Xu K, Wu X, Shapiro E, et al. (2012) Bmp7 Functions via a Polarity Mechanism to Promote Cloacal Septation. *PLoS One,* 7, e29372.

Yamaguchi K, Kiyokawa J, Akita K. (2008) Developmental processes and ectodermal contribution to the anal canal in mice. *Ann Anat,* 190, 119-128.

Zhang T, Zhang HL, Wang DJ, et al. (2011) Normal development of hindgut and anorectum in human embryo. *Int J Colorectal Dis,* 26, 109-116.

Chapter 3
Development of extrinsic innervation in the abdominal intestines of human embryos

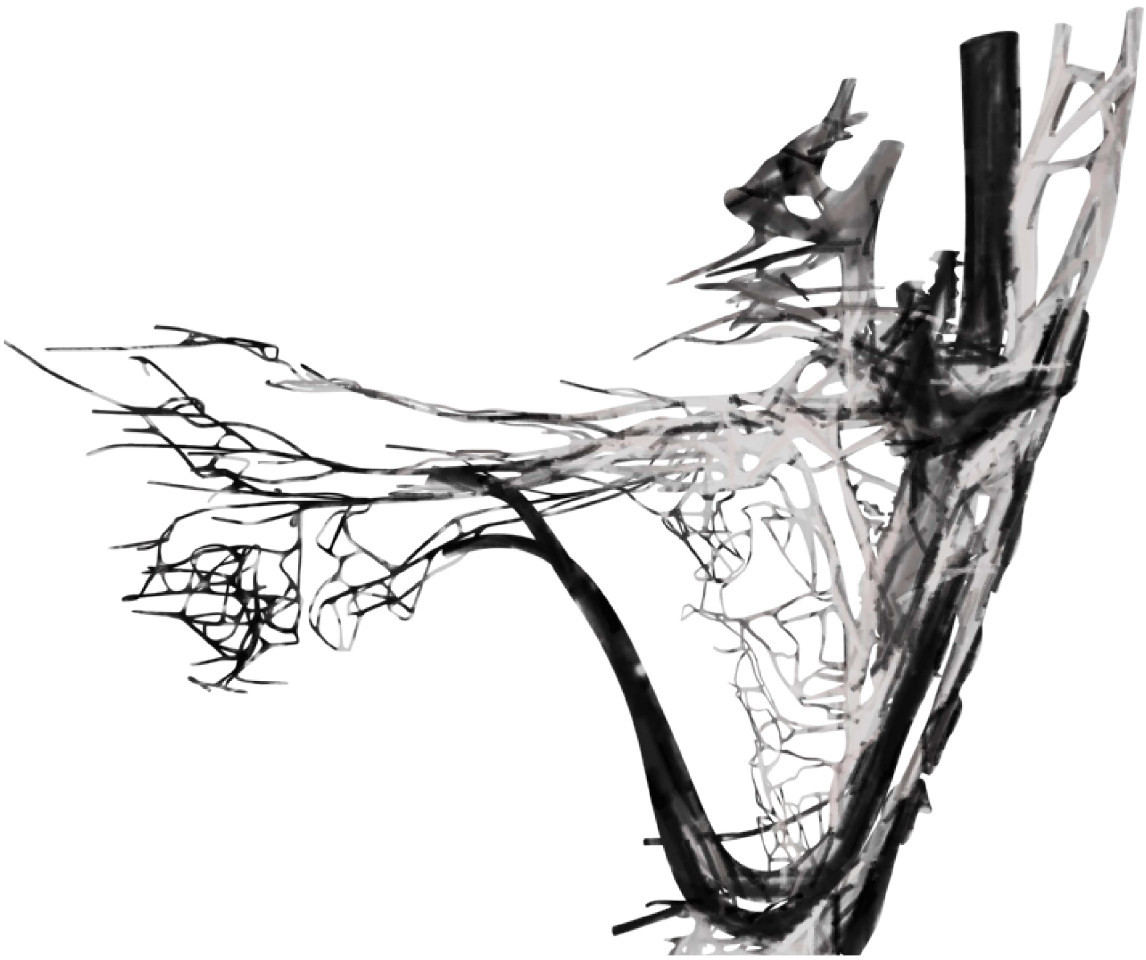

Nutmethee Kruepunga, Jill P.J.M. Hikspoors, Cindy J.M. Hülsman,
Greet M.C. Mommen, S. Eleonore Köhler and Wouter H. Lamers
Journal of Anatomy (2020); 237(4): 655-671

Abstract

Compared to the intrinsic enteric nervous system (ENS), development of the extrinsic ENS is poorly documented, even though its presence is easily detectable with histological techniques. We visualised its development in human embryos and foetuses of 4-9.5 weeks post-fertilisation using Amira 3D-reconstruction and Cinema 4D-remodelling software. The extrinsic ENS originated from small, basophilic neural crest cells (NCCs) that migrated to the para-aortic region and then continued ventrally to the pre-aortic region, where they formed autonomic pre-aortic plexuses. From here, nerve fibres extended along the ventral abdominal arteries and finally connected to the intrinsic system. Schwann cell precursors (SCPs), a subgroup of NCCs that migrate on nerve fibres, showed region-specific differences in differentiation. SCPs developed into scattered chromaffin cells of the adrenal medulla dorsolateral to the coeliac artery (CA) and into more tightly packed chromaffin cells of the para-aortic bodies ventrolateral to the inferior mesenteric artery (IMA), with reciprocal topographic gradients between both fates. The extrinsic ENS first extended along the CA, and then along the superior mesenteric artery (SMA) and IMA 5 days later. Apart from the branch to the coecum, extrinsic nerves did not extend along SMA branches in the herniated parts of the midgut until the gut loops had returned in the abdominal cavity, suggesting a permissive role of the intraperitoneal environment. Accordingly, extrinsic innervation had not yet reached the distal (colonic) loop of the midgut at 9.5 weeks development. Based on intrinsic ENS-dependent architectural remodelling of the gut layers, extrinsic innervation followed intrinsic innervation 3-4 Carnegie stages later.

Introduction

The enteric nervous system (ENS) is, together with the sympathetic and parasympathetic systems, a component of the autonomic nervous system as defined by Langley (1921). The ENS regulates intestinal motility, secretion, and blood flow. The ENS is also known as the "little" or "second" brain because of the large number of enteric neurons (2-6*10^8 in man (Furness et al., 2014) and 1-1.5*10^6 in mice (Gianino et al., 2003)) and their complex network of connections (Gershon, 1999). It consists of intrinsic and extrinsic components. The intrinsic ENS comprises ganglionated plexuses in the wall of the intestine, while the extrinsic ENS is mainly found as catecholaminergic fibres along the arterial trees that perfuse the intestine. The entire ENS originates from neural crest cells (NCCs; for review, see e.g. (Sasselli et al., 2012)). NCCs may well represent the last remaining group of pluripotent cells of the epiblast (Buitrago-Delgado et al., 2015). NCCs make the first of many sequential steps towards differentiation into neuronal or glial cells shortly after delamination from the neural plate (Soldatov et al., 2019). This series of sequential binary decisions shows that the fate of NCCs is not prespecified, but that their differentiation is accompanied by a progressive restriction of developmental options (Ruhrberg and Schwarz, 2010, Anderson, 1989).

The fates of the head and trunk NCCs differ (Kuratani et al., 2018). The cephalic NCCs typically migrate along a dorsolateral pathway underneath the surface epithelium (Serbedzija et al., 1992), whereas most truncal NCCs follow a ventrolateral pathway (Serbedzija and McMahon, 1997). The vagal neural crest, which arises adjacent to somites 1-5 in embryonic day (ED) 8.5 mouse embryos (≈ Carnegie Stage (CS) 11 in human embryos) (Durbec et al., 1996), represents a transitional structure (Kuratani et al., 2018): its cranial portion (adjacent to somites 1 and 2) migrates along the dorsolateral route and colonises the emerging vagus nerve alongside the oesophagus and stomach, while its caudal portion (adjacent to somites 3-5) migrates ventrolaterally to populate the emerging cranial portion of the sympathetic trunks and the entire caudal foregut and midgut (Anderson et al., 2006, Espinosa-Medina et al., 2014). The minority of NCCs in neck and trunk that follow the dorsolateral pathway expresses the marker c-KIT, but not the neurotrophin receptor p75NTR. The majority of NCCs that follow the ventral pathway, instead, express the reciprocal phenotype (Wilson et al., 2004) and pass between the neural tube and the dermomyotomes along the intersomitic blood vessels and then through the cranial portion of the sclerotomes (Serbedzija et al., 1990, Ruhrberg and Schwarz, 2010). The earliest group of these cells

(ED8.5-9.5 in the mouse, ~CS11-late) follows a more ventrolateral course towards the para-aortic space to form the sympathetic trunks, whereas a slightly later group (ED9.5-ED10.5; CS12-14) follows a more medial route to the spinal motor nerves (Serbedzija et al., 1990).

NCCs that reside on the spinal nerves often differentiate into Schwann cells, but a subpopulation retains the capacity to differentiate into ganglionic cells. The entire population was referred to as "Schwann-cell precursors" (SCPs) 30 years ago (Jessen and Mirsky, 1991), but were already recognized by phenotype and position 80 years earlier (Kuntz, 1910). SCPs are found on the vagus nerve (Espinosa-Medina et al., 2014), but also account for as much as 80% of the chromaffin cells of the adrenal medulla (Furlan et al., 2017) and para-aortic bodies (Kastriti et al., 2019). Furthermore, up to 5% of the submucosal neurons in the small intestine and ~20% of the submucosal and myenteric neurons in the colon have an SCP origin (Uesaka et al., 2015). NCCs that become sympathetic neurons and those that become SCPs and eventually chromaffin cells differ phenotypically in that SCPs express more tyrosine hydroxylase (TH), less cocaine and amphetamine-regulated transcript (CART), and have a lower proliferative activity than sympathetic neurons well before they arrive at their respective target positions (Chan et al., 2016). The decision of cells in sympathetic ganglia or ganglionic plexuses of the gut to differentiate into ganglionic or glial cells depends on upregulation of the expression of transcription factor PHOX2B at ED10.5 (~CS14) (Tiveron et al., 1996) and the ensuing downregulation of neural stem-cell marker SOX10 (Nagashimada et al., 2012). NCC migration is largely determined by environmental signals that induce or maintain growth in the NCC population (Young et al., 2001, Burns and Thapar, 2006, Vega-Lopez et al., 2017, Lumb et al., 2018).

Whereas the development and fate of the intrinsic ENS has been studied extensively in the last 40 years, the extrinsic ENS has mustered only cursory interest (Uesaka et al., 2016). This discrepancy is the more remarkable since at least part of the extrinsic ENS is phenotypically identifiable in standardly stained sections because of the early appearance of the acidophilic staining property of its nerve fibres. Since no recent account of its early topographic development in human embryos is available, we have carried out such a study, using histology as method of identification and three-dimensional reconstruction as method to visualize developmental changes in architecture and distribution.

Materials and methods

Embryos

This study was undertaken in accordance with the Dutch regulations for the proper use of human tissue for medical research purposes. Well-preserved human embryos and foetuses of the historical collections of the Departments of Anatomy and Embryology, Leiden University Medical Centre (LUMC), Leiden, the Academic Medical Centre (AMC), Amsterdam, Radboud University, Nijmegen, The Netherlands, and the University of Göttingen, Germany (Blechschmidt Collection; https://doi.org/10.3249/ugoe-publ-2) that were donated for scientific research were studied. In addition, digital images of carefully staged human embryos of the Carnegie collection (Washington D.C., USA) were downloaded from the Digitally Reproduced Embryonic Morphology (DREM) project (http://virtualhumanembryo.lsuhsc.edu). A detailed time line of the development of the enteric nervous system in mice can be found in (Sasselli et al., 2012, Hao et al., 2016).

Image acquisition, 3D reconstruction, and visualization

Human embryos and foetuses between 4 and 9.5 weeks of development were studied. Embryonic development is expressed in Carnegie Stages (CS), which, from the 3rd week onward, are virtually identical to Streeter's Developmental Horizons (Streeter, 1951, O'Rahilly and Müller, 1987). CS were converted into estimated embryonic age according to (O'Rahilly and Müller, 2010). A graph relating the Carnegie stages of human embryos to days of development in mice or Hamilton-Hamburger (HH) stages (Hamburger and Hamilton, 1951) in chicken is found in Supplemental Figure S3.1. The resolution of the physiological hernia at 9.5 weeks was used as criterion to define foetal ages between 9 and 9.5 weeks of development (Soffers et.al, 2015) (Table 3.1). Serial sections from AMC, LUMC, and Radboud embryos were digitized with an Olympus BX51 or BX61 microscope and the Dotslide program (Olympus, Leiderdorp, The Netherlands), whereas those of the Blechschmidt collection were digitized with a Zeiss Axio Scan.Z1 (Carl Zeiss Microscopy, Jena, Germany). All digital images were converted into greyscale 'JPEG' format and loaded into Amira3D (version 6.5; FEI Visualization Sciences Group Europe, Merignac Cedex, France). The greyscale images were aligned automatically with the least-squares alignment mode and further adjusted manually for the correct curvature of the embryonic body axis with the help of photographs and magnetic resonance images (MRI) of human embryos of the same

stage of development (Pooh et al., 2011). Structures of interest were segmented manually and reconstructed three-dimensionally with the Amira3D program. Because small deformations of individual sections due to histological processing and section stacking introduced a distracting noise into the 3D reconstructions, polygon meshes from all reconstructed materials were exported via 'vrml export' from Amira3D to Cinema 4D (MAXON Computer GmbH, Friedrichsdorf, Germany) and remodelled using the Amira3D model as template. The accuracy of the remodelling process was validated by simultaneous visualization in Cinema 4D of the Amira3D output and the remodelled Cinema model (Supplemental Figure S3.2). The Cinema-4D models were transferred via 'wrl export' to Adobe Acrobat version 9 (http://www.adobe.com) to generate interactive 3D Portable Device Format (PDF) files, which are an easily accessible format for 3D visualization (Supplemental Figures S3.3-3.5). Whereas we mostly refer in the text to the Figures to relate histology to developing structures, the reader is encouraged to simultaneously inspect the interactive PDFs, because their rotational options ("live" images) allow a much better understanding of the complex local topography than the "still" images in the Figures.

Terminology

We categorized the nerve fibres innervating the gut into intrinsic and extrinsic fibres. The well-studied intrinsic nerve fibres are located in the intestinal wall, whereas the less-studied extrinsic nerve fibres have their origin outside the gut and reach the gut wall, as we show, predominantly by following the peripheral branches of the intestinal arteries (Uesaka et al., 2016).

Intestinal development in avian embryos (Southwell, 2006) proceeds in a similar fashion as in mammalian embryos (Soffers et al, 2015), with the midgut or primary loop extending into the coelom of the umbilical cord. In agreement, the umbilical "hernia" contains only the midgut in both vertebrate classes. The main differences appear to be the formation in birds of only a single (duodeno-jejunal) rather than 4 secondary loops and 2 rather than 1 coecal diverticula. However, the nomenclature used to identify the respective parts of the embryonic gut is not the same and at times confusing. In avian and mammalian embryos the cells of the vagal neural crest colonise both the "pre-umbilical" and "post-umbilical" parts of the gut, whereas sacral NCCs only colonise the "post-umbilical" gut in a caudocranial direction (Le Douarin & Teillet, 1973; Burns & Le Douarin, 1998; Anderson & Young, 2006). The sacral neural crest begins distal to

somite 24 in mice (Dong et al., 2006) and somite 28 in chicken (Le Douarin & Teillet, 1973), which corresponds to vertebral segment L1-2 in both birds and mammals. In mammalian embryos, the part of the gut colonised by sacral NCCs is often referred to as hindgut (Young & Newgreen, 2001; Wang & Chan, 2011) and corresponds with the distal loop of the embryonic midgut and hindgut "proper" in our descriptions. The autonomic innervation of the embryonic hindgut is reported in the accompanying study.

Results

Early sources of peripheral autonomic ganglionic cells

The neural crest had formed and its cells were actively migrating in CS13 human embryos (~32 days of development (O'Rahilly and Müller, 2007)), but spinal nerves and their associated ganglionic cells still had to develop. Small scattered intensely basophilic cells appeared laterally to the dorsal aorta at CS14-early (~33 days; Figure 3.1, blue arrows in panel C). We identified these cells as neural crest-derived cells, because phenotypically similar cells at this developmental stage and location had previously been shown to be c-RET-, SOX10-, and p75NTR-positive neural-crest cells (Fu et al., 2003, Wallace and Burns, 2005). Cells with similar staining properties as the neural crest-derived ganglionic cells in Figure 3.1C transiently accumulated on the vagus nerve in CS14-mid (~34 days; not shown), on the spinal nerves of cervical segments C1-C6 in CS14-late (~35 days; Figure 3.2A, B), and at a lower density on more caudal nerves in CS15 embryos (not shown). Spinal nerves in front of the "wave" did not show such nerve-associated cells (e.g. pale nerve fibres in Figure 3.2D for CS14-late).

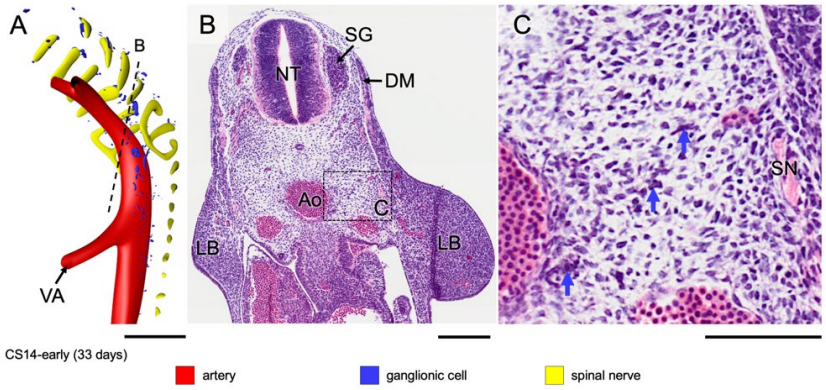

Figure 3.1 **Appearance of neural crest-cell precursors of ganglionic cells in a CS14-early embryo (~33 days).** Panel A shows the distribution of ganglionic precursor cells dorsal and lateral to the dorsal aorta (see also Supplemental Figure S3.3A). The ventral roots of the spinal nerves are coded yellow. Panels B and C show a section indicated by the dotted line in panel A and a magnified view of the rectangle in panel B. Intensely staining basophilic cells (blue arrows in panel C) represent ganglionic precursor cells between spinal nerve (SN) and aorta (Ao) in panel C. Bars = 200 µm.

Early development of the sympathetic trunk

In CS14-late embryos (~35 days), the number of ganglionic cells lateral to the dorsal aorta had increased markedly between the mid-cervical and lower thoracic segments. In the next few days (CS15 and CS16; 36-39 days of development) part of these still scattered ganglionic cells began to form two longitudinal columns laterally to the dorsal aorta. Furthermore, strands of ganglionic cells began to form caudal to cervical segment C3 between the entrance of spinal nerves into dermomyotomes laterally and the foregut and dorsal aorta medially (blue arrows in Figure 3.2F), together with tiny nerves (dark-yellow arrows in Figure 3.2A,G; see also in Supplemental Figure S3.3B). Based on this topography, we have identified the dorsolateral columns of scattered cells as the emerging sympathetic trunks and the small nerves as communicating branches. The communicating branches elongated from the spinal nerves to the sympathetic trunks at CS15-early (~36 days; Figure 3.3, dark-yellow arrow in panel C) and joined these trunks at CS15-late (~37 days; Figure 3.4, dark-yellow arrow in panel C). In the 2-3 days between CS14-late and CS15-late the position of the forming sympathetic trunk changed from lateral to dorsolateral of the dorsal aorta (cf. Figures 3.2C and F, 3.3B and C, and 3.4B and C). The ganglionic cells of the sympathetic trunk extended caudally to thoracic level T8 at CS14-late, lumbar level L2 at CS15-early

(~36 days), sacral level S1 at CS15-late (~37 days), and S5 at CS16 (~39 days). The rate of caudal extension of the sympathetic trunk was, therefore, ~4 segments per day (Supplemental Figures 3.3-5). The cell density in the clusters of the caudal-most 5-6 segments of the sympathetic trunk rapidly increased during the first 1-2 days after they became identifiable. We will describe the development of the sympathetic trunk in more detail in a subsequent study.

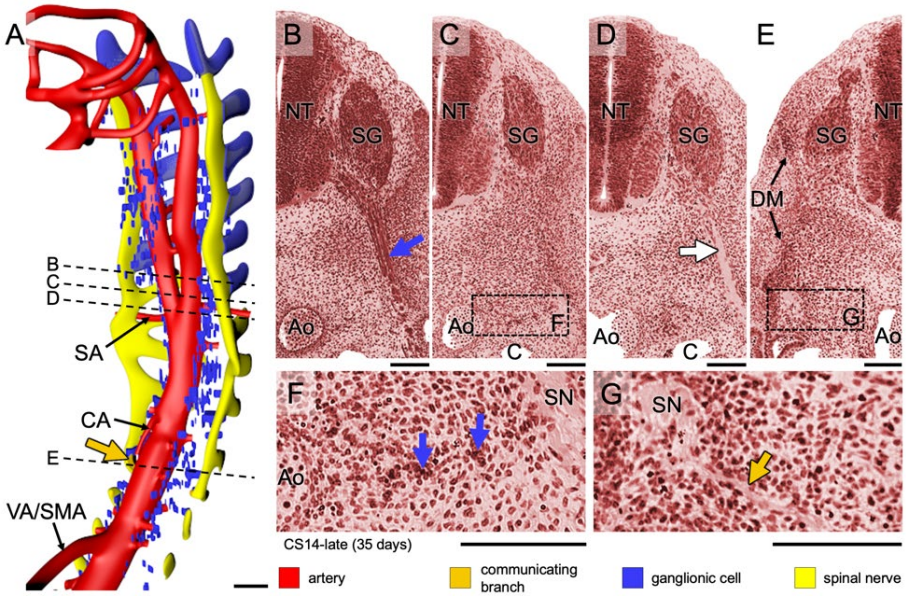

Figure 3.2 **Formation of sympathetic trunks and communicating branches in a CS14-late embryo (~35 days).** Panel A shows the distribution of ganglionic cells with the ventral roots of spinal nerves and dorsal aorta from C1 to T5 (see also Supplemental Figure S3.3B). Panels B - E show transverse sections from cranial to caudal as indicated by dotted lines in panel A. Panels F and G show magnified views of the rectangles in panels C and E, respectively. In this embryo, Schwann cell precursors cells migrate along the ventral roots of spinal nerves as intensely staining strands in the cervical region (blue cover on spinal roots in panel A and blue arrow in panel B), but not further caudally (pale nerve strand; white arrow in panel D). Ganglionic cells (blue arrows) are also present between the dorsal aorta (Ao) and spinal nerves (SN) in this area (panel F). Furthermore, nerve fibres extend medially following the route of ganglionic cells as communicating branches in the upper thoracic region (dark-yellow arrow in panels A,G). Bars A = 200 µm; B-G = 100 µm.

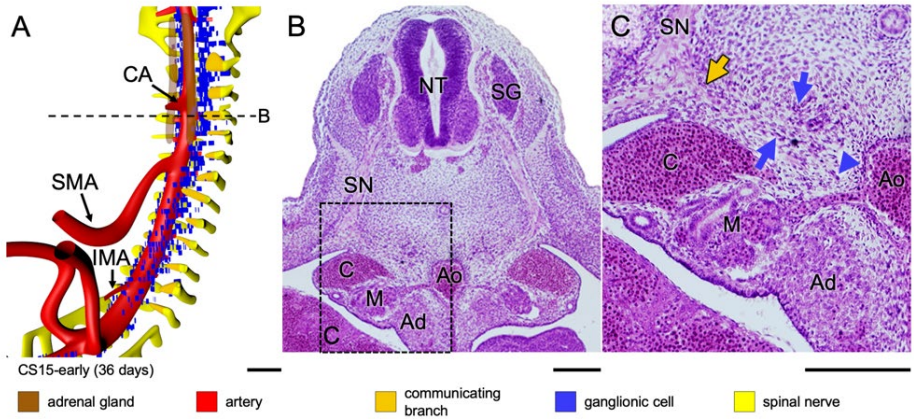

Figure 3.3 **Aggregation of ganglionic cells dorsolateral to aorta in a CS15-early embryo (~36 days).** Panel A shows the distribution of ganglionic cells with ventral roots of spinal nerves, communicating branches, and dorsal aorta (see also Supplemental Figure S3.3C). Panels B and C show a transverse section and its magnified view, respectively, as indicated by a dotted line in panel A. Two groups of ganglionic cells are seen: aggregated sympathetic ganglia dorsolateral to the dorsal aorta, and ventrally migrating ganglionic cells (blue arrows and arrowhead in panel C, respectively). In addition, communicating branches are present (beige arrow in panel C). Bars A = 200 µm; B-C = 100 µm.

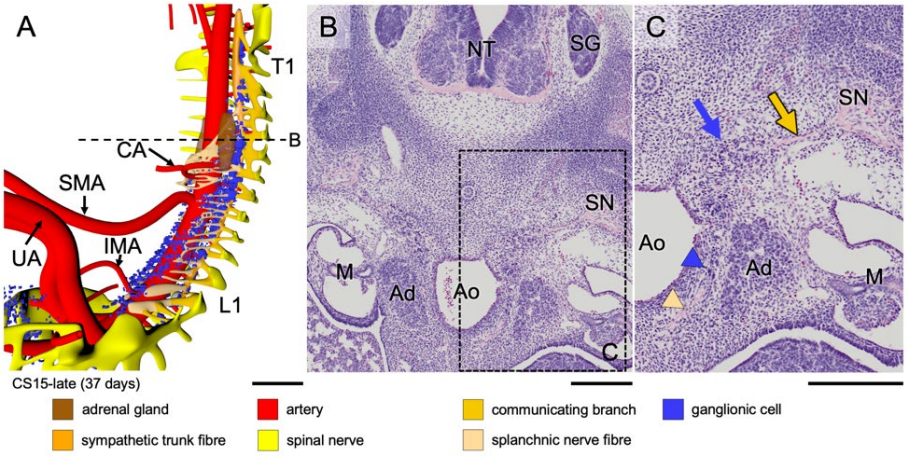

Figure 3.4 **Formation of ventral (pre-aortic) plexuses in a CS15-late (~37 days) embryo.** Panel A shows the distribution of ganglionic cells and nerve fibres around the aorta (see also Supplemental Figure S3.3D). Panels B and C show a transverse section and its magnified view, respectively, as indicated by the dotted line in panel A. Note communicating branch and sympathetic trunk (beige and blue arrows, respectively). Both ganglionic cells and nerve fibres (blue and beige arrowheads, respectively) migrate ventrally between the aorta and developing adrenal gland (Ad). Ganglionic cells accumulated around the roots of the CA and IMA, but not yet around the SMA (panel A). In addition, ventrally extending nerve fibres have formed a plexus around the CA. Bars A = 500 µm; B-C = 200 µm.

Ventral migration of ganglionic cells

Scattered ganglionic cells were also found near the oesophagus, but these cells were associated with the developing vagus nerve. We will also describe the development of the vagus nerve in a separate study. Along the medial boundary of the adrenal gland, so starting just caudal to the future diaphragm, scattered ganglionic cells remained present not only in the form of both columns of the sympathetic trunk dorsolateral to the aorta, but also as scattered cells lateral to the aorta. These lateral cells were initially (CS15-early) most abundant between the coeliac (CA) and inferior mesenteric arteries (IMA) (Figure 3.3A), but caudal to the superior mesenteric artery (SMA; successor of vitelline artery) these cells then (CS15-late, CS16) moved on towards the ventral side of the aorta (Figures 3.4A and 3.5A), so that ganglionic cells that remained associated with the adrenal cortex were mainly seen in the area between T7 and T12. At the same time (CS15-late) nerve fibres (beige arrowhead in Figure 3.4C) amidst this lateral group of scattered ganglionic cells (blue arrowhead) extended ventrally and had become well-developed entities at CS16 (~39 days of development; Figure 3.5A; histological details in panels B-D). At CS18 (Figure 3.6), the number of ganglionic cells at the site of the forming adrenal medulla increased substantially (panels B and C), while dorsoventrally oriented nerve fibres extended further ventrally (beige arrowhead) and started to form a network around the stem of the coeliac trunk (Supplemental Figure S3.4B). The dorsoventral fibres became subsequently (CS20) organized into nerve trunks that formed, from cranial to caudal, the greater, lesser, and least splanchnic nerves, respectively, while the ventral network formed the coeliac nerve plexus (Figure 3.7A, Supplemental Figures S3.3-5).

Starting also at CS16 (~39 days), a ventral plexus developed between IMA and aortic bifurcation, which, like its coeliac counterpart, was connected with the sympathetic trunk. These nerve fibres are known as the lumbar splanchnic nerves (LSN in Figure 3.5A). At CS16, small nerve fibres from the IMA plexus extended caudally (# in Figure 3.5A,D) and passed, at CS18, the root of the umbilical arteries to become the single superior hypogastric nerve (# in Figure 3.6A,B). This single nerve trunk began to split up into a plexus of smaller nerve fibres in CS20 embryos and is described in more detail in the accompanying article. The superior hypogastric nerve bifurcated distal to the umbilical arteries into left and right hypogastric nerves (Figure 3.6B). Although nerves also surrounded the IMA and the stem of the SMA, these parts of the ventral aortic plexus started to develop relatively late (CS20; ~49 days) and became well-developed only by CS22 (~53 days).

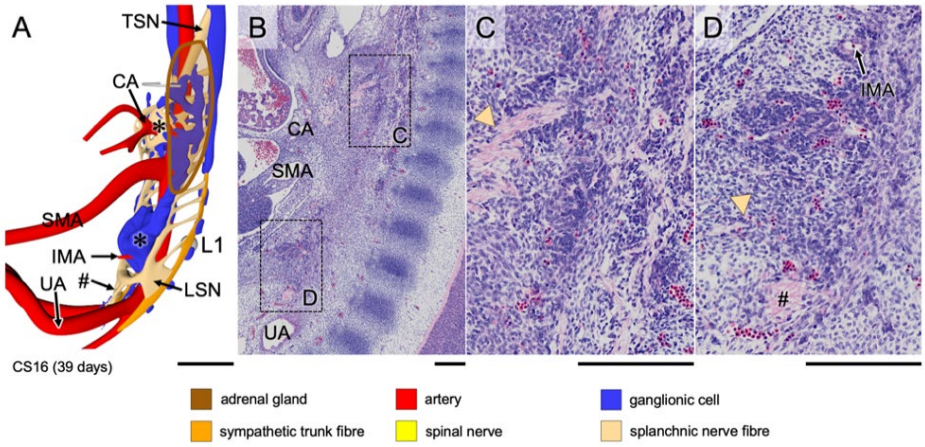

Figure 3.5 **Appearance of coeliac and inferior mesenteric plexuses in a CS16 (~39 days) embryo.** Panel A shows a right ventrolateral view of the distribution of ganglionic cells and nerve fibres, with the left adrenal gland (brown contour; see also Supplemental Figure S3.3E). Panel B shows a paramedian sagittal section of the plexuses surrounding the roots of the CA and IMA (boxes), with panels C and D showing magnified views. The roots of both CA and IMA are surrounded by abundant ganglionic cells (indicated by asterisks in panel A), whereas the root of the SMA is almost devoid of ganglionic cells. Nerve fibres of the thoracic splanchnic nerves (arrowhead in panel C) integrate with the ganglionic cells surrounding the root of CA. Similarly, nerve fibres of the lumbar splanchnic nerves (arrowhead in panel D) integrate with the ganglionic cells surrounding the root of IMA. Nerve bundles (#) from the lumbar splanchnic nerves extend caudally across the bifurcation of the umbilical arteries to form the superior hypogastric nerve. Bars A = 500 µm, B-D = 200 µm.

Fate of para-aortic ganglionic cells

The para-aortic ganglionic cells either retained their intense staining mode or differentiated into pale-staining cells that typically formed coherent agglomerates. The former group of cells evolved into ganglionic cells that were to become the adrenal medulla, whereas the latter transformed into the so-called para-aortic bodies (Coupland, 1952). The intensely staining scattered ganglionic cells predominated cranially near the CA and covered the medial side of the adrenal cortex, which they had started to penetrate with finger-like extensions (blue arrowheads in Figure 3.6C). The intensely staining cells tapered off caudally (blue arrowheads in Figure 3.6D), where smaller aggregates were seen in association with the superior hypogastric nerve (Figure 3.6B). Differentiation of the para-aortic bodies (colour coded light blue in Figures S3.6-S3.8) proceeded via the formation of coherent, but still intensely staining agglomerates at CS18 (~44 days; P in Figure 3.6D) to the definitive pale-staining para-aortic bodies at CS20 (~49 days; P in Figure 3.7D). The pale-staining cells predominated

caudally, with the largest, dumbbell-shaped para-aortic body, known as Zuckerkandl's organ (Zuckerkandl, 1901), typically straddling the IMA at its cranial side, but smaller agglomerates of pale cells were present more cranially, with the upper-most agglomerate usually seen at the level of the adrenals (Figure 3.7B). The opposite and partially overlapping gradients between persistence of scattered, intensely staining ganglionic cells and formation of para-aortic bodies was striking and obvious in CS18 and CS20 embryos.

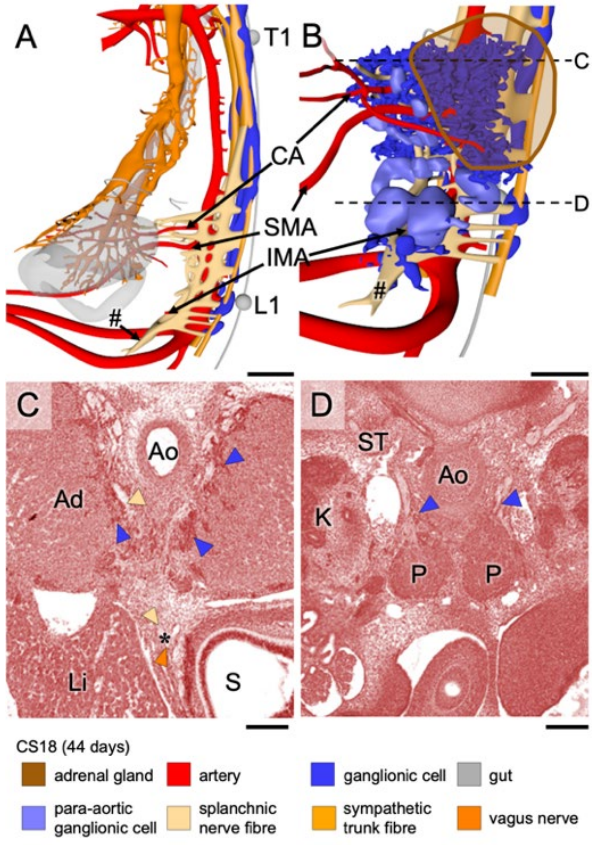

Figure 3.6 **Extension of the coeliac and inferior mesenteric plexuses in a CS18 (~44 days) embryo.** Panels A and B show side views without and with ganglionic cells in the pre-aortic plexuses, respectively (see also Supplemental Figure S3.4A). Ventral plexus fibres have contacted the vagal nerve plexus on the stomach (panel A). Panels C and D show transverse sections at the levels indicated by dotted lines in panel B. Scattered ganglionic cells (blue arrowheads) surround the root of the CA and invade the adrenal cortex (AC; panels C and D), whereas clustered ganglionic cells form the para-aortic bodies (P; panel D). A branch of the lumbar splanchnic nerves has extended caudally and passes the umbilical arteries ventrally to form the superior hypogastric nerve (# in panel A). Bars A, B = 500 µm, C,D = 200 µm.

Extension of nerves along the ventral abdominal arteries

No ganglionic cells or nerve fibres were found around any of the three abdominal arterial trunks until CS15-late (~37 days), when nerve fibres began to surround the root of the CA (Figure 3.4A). Ganglionic cells followed at CS16 (~39 days) and more massively at CS18 (~44 days), concomitant with a major increase in the number of ganglionic cells at the site of the forming adrenal medulla (blue arrowheads in Figure 3.6C,D). Ganglionic cells surrounded the roots of the SMA and IMA with a similar timeline as described for the CA (Figure 3.6A,B), but nerve fibres passed the clusters of ganglionic cells (beige in Figure 3.7B) to extend along the stems of the SMA and IMA ~2 stages (CS20) later than those along the stem of the CA (CS18).

Nerves of the coeliac plexus started to extend along the main stem and branches of the CA at CS18 (~44 days) to the duodenum ventrally and to the stomach and spleen craniodorsally. These nerve branches (beige) met those of the vagal trunks (orange) on the surface of the stomach (orange-coded nerve tree in Figure 3.6A and asterisk in Figure 3.6C). In the reconstructed embryo the connection was best developed via the coeliac branch of the posterior vagal trunk. At CS20 (~49 days), nerve fibres also extended distally along the main trunk of the IMA and, to a lesser extent, of the SMA (Figure 3.7A). At CS22 (~53 days; Figure 3.8) the nerve fibres surrounding the CA extended to the surface of the stomach, and those surrounding the IMA to the surface of the hindgut (Supplemental Figure S3.5A). Histologically, we established that, at this stage, both extrinsic plexuses (Figure 3.8C,H,I; beige arrowheads) connected to the intrinsic nerve fibres (Figure 3.8C,H,I; light green arrowheads) along the corresponding parts of the gut wall. Meanwhile, nerve fibres surrounding the SMA that extended within the dorsal mesentery of the midgut loop followed the main trunk of that artery to the coecum, but the nerves surrounding its other branches only reached to the umbilical ring (Supplemental Figure S3.5A). Accordingly, the first secondary gut loop, which comprises distal duodenum and proximal jejunum and never leaves the peritoneal cavity (Soffers et al., 2015), had become colonised by extrinsic nerves at 8 weeks. Extrinsic innervation of the 2nd - 4th secondary loops, which do herniate, developed by extension along the arterial branches of the SMA only upon the return of these loops into the peritoneal cavity during the 9th week of development (Figure 3.9B,C,F-H). However, in the 9.5 weeks embryo, extrinsic nerves had not yet reached the surface of the 4th secondary loop (distal ileum containing the regressing, but still patent vitelline artery; Figure 3.9A') and the colic part of the midgut between coecum and left colic artery (dotted line in Figure 3.9E, histological details in panels D, K). The

extrinsic fibres, therefore, reached the coecum well before those to the distal ileum and colic part of the midgut arrived at their destination (Supplemental Figure S3.4B).

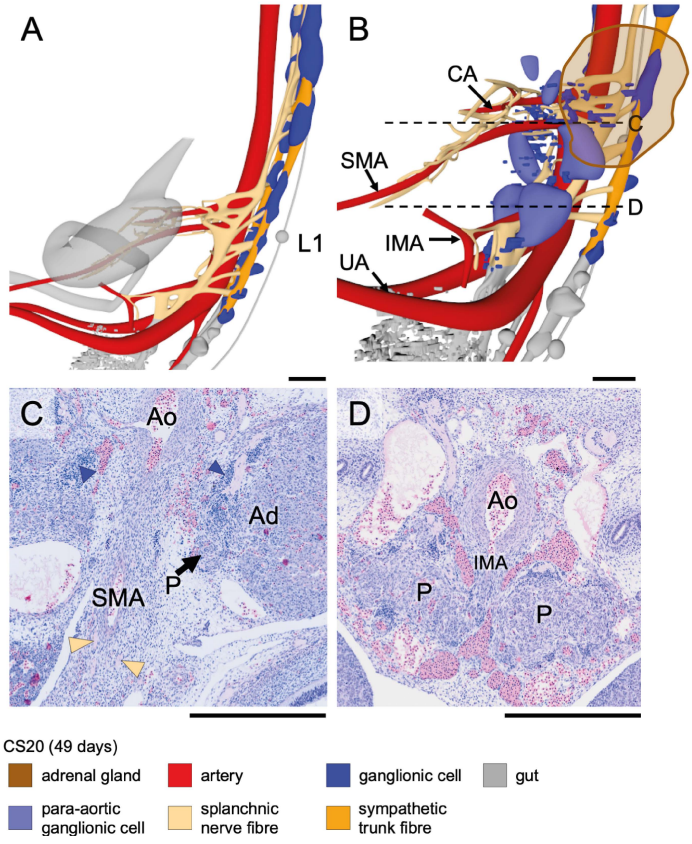

Figure 3.7 **Coeliac and inferior mesenteric plexuses in a CS20 (~49 days) embryo.** Panels A and B show side views without and with ganglionic cells in the pre-aortic plexuses, respectively (see also Supplemental Figure S3.4B). Panels C and D show transverse sections at the levels indicated in panel B. Compared to CS18 and to scattered ganglionic cells (blue arrowheads), clustered ganglionic cells have become paler (P in panels C and D). At the level of the IMA (panel D) para-aortic bodies are substantially larger than at the level of the SMA (panel C). Bars = 500 µm.

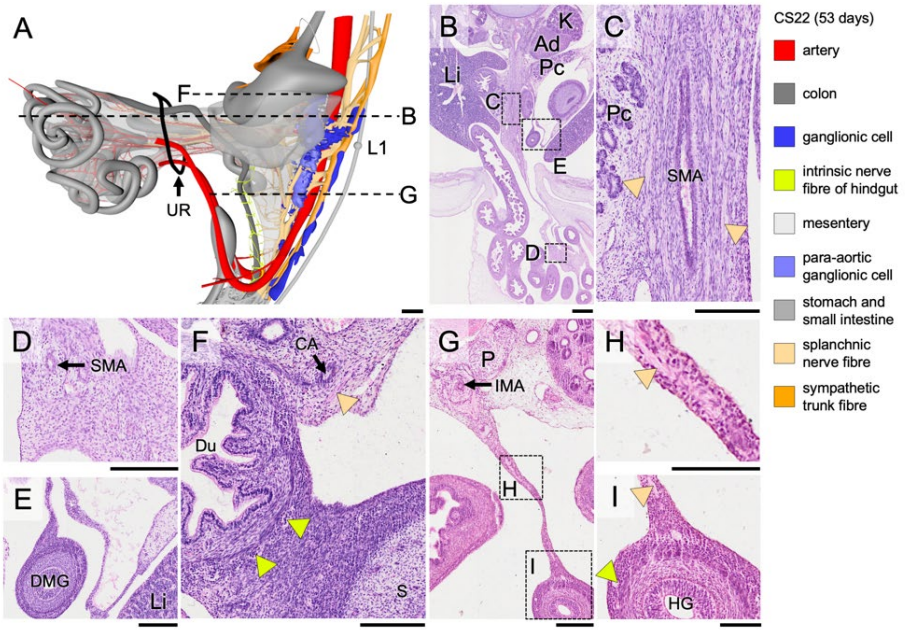

Figure 3.8 **Expansion of extrinsic nerves along the superior mesenteric artery and appearance of contacts between extrinsic and intrinsic enteric nerves in a CS22 (~53 days) embryo.** Panel A shows a side view, including the umbilical hernia of the midgut (black ring: umbilical ring; note further that the mesentery is rendered in transparent grey; see also Supplemental Figure S3.5A). Panel B shows a transverse section at the level indicated in panel A, with magnified views of the root of mesentery containing the main trunk of SMA, extra-abdominal loops of the small intestine and colon in panels C-E, respectively. Panel F shows a transverse section of the duodenum at the level indicated in panel A. Note numerous well-developed intrinsic ganglia, but absence of nerve fibres in the duodenal wall, as opposed to the configuration of the hindgut (panel I). Panel G shows a transverse section of the midgut (thin mesentery) at the level indicated in panel A, with the boxes magnified in panels H and I. Nerve fibres extend along branches of the SMA to the intra-abdominal small intestine and coecum (beige arrowheads in panel C), but not to the extra-abdominal part of the small intestine and proximal colon (panels D and E, respectively). In the hindgut, the extrinsic nerve fibres (beige arrowheads in panels H and I) have extended along the mesentery and connect with nerve fibres within the hindgut mesenchyme (light green arrowhead in panel I). Bars A-D = 500 µm, E-J = 200 µm, K-L = 100 µm.

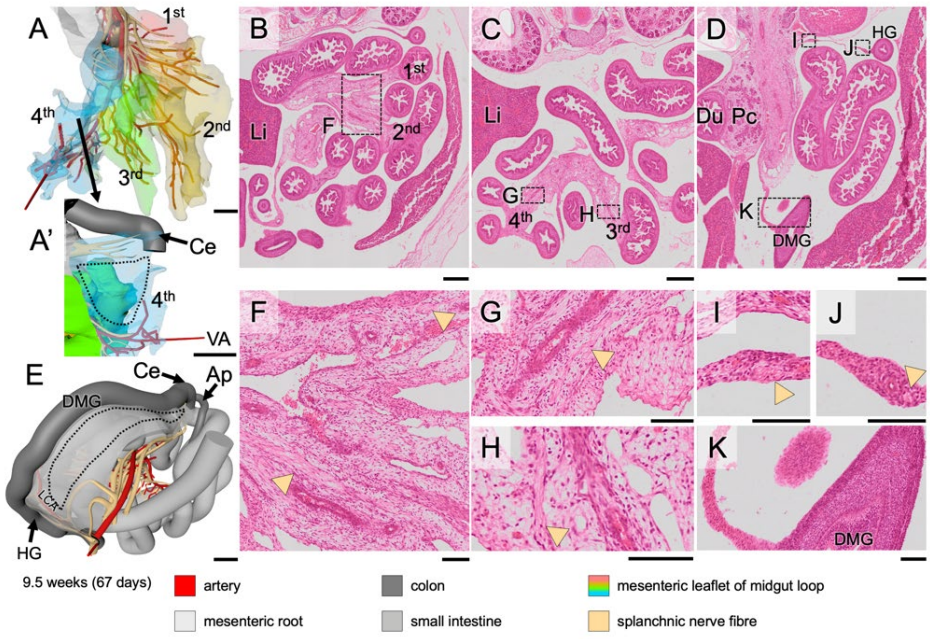

Figure 3.9 **The extension of the extrinsic nerve fibres in the midgut in a 9.5 weeks embryo.** Panels A and E show the midgut region in frontal and dorsolateral views, respectively; see also Supplemental Figure S3.5B). The intestines have returned into the abdominal cavity. Panels B-D show transverse sections of the abdominal cavity and intestinal loops, with magnified views of the boxes in panels F-K. The small intestinal part of the midgut has 4 secondary loops, each of them anchored by its own mesenterial fold (1st – 4th; panel A; (Soffers et al., 2015)). The extrinsic nerve fibres along branches of the SMA have reached all midgut loops (beige arrowheads in panels F-H) except for the distal ileum (dotted line in panel A') and proximal colon (dotted line in panel E and panel K), whereas the distal colon and hindgut is innervated by nerve fibres extending along the IMA (beige arrowheads in panel I-J). Bars A,E = 1 mm, B-D = 500 µm, F-K = 100 µm.

Neural crest cell-induced changes in intestinal-wall architecture

Vagal neural crest-derived cells that will form the intrinsic ENS begin to migrate through the wall of the gut at CS14 (Fu et al., 2003, Wallace and Burns, 2005). We noticed that the arrival of these cells changed the morphology of the intestinal wall by inducing the appearance of a layered architecture with p75NTR-positive cells forming a prominent and characteristic peripheral layer (Wallace and Burns, 2005). To be able to correlate the progression of the extrinsic to that of the intrinsic enteric nervous system, we mapped the time line of the appearance of this layer (Figure 3.10). The external ring of cells became first visible in the foregut (oesophagus, stomach and proximal small

intestine) at CS17, in the middle portion of the small intestine at CS18, in the distal small intestine and hindgut just cranial to the cloaca (Kruepunga et al., 2018) at CS20, and in the remaining parts of the colon (distal limb of midgut) at CS22. The delay between the passage of the migratory front of neural crest-derived cells and the subsequent transformation of the architecture of the gut wall was 2-3 Carnegie stages in the small intestine and ~4 Carnegie stages in the colon.

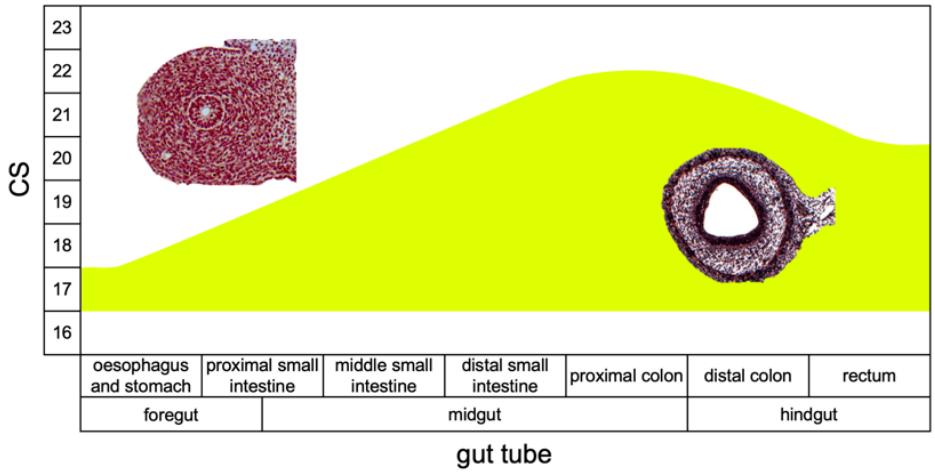

Figure 3.10 **Time line of the appearance of layering in the gut wall of human embryos.** The histological sections show the absence (left) and presence (right) of the layered gut wall. The layered gut wall appears first in oesophagus, stomach and proximal small intestine at CS17, in the middle portion of the small intestine at CS18, in the distal small intestine and distal hindgut (just cranial to cloaca) at CS20, and in the rest of the colon (ascending limb and hindgut) at CS22.

Discussion

The present study shows that extrinsic innervation of the gut becomes established between ~5 and ~9.5 weeks of development. We distinguished three stages (Figure 3.11): migration of neural crest cells (NCCs) to the para-aortic area (5th week; CS14 and CS15); migration of ganglionic cells and nerve fibres from the para- to the pre-aortic area and stems of the abdominal arteries, in particular the coeliac (CA) and inferior mesenteric (IMA) arteries (6th week; CS16-18); and finally the extension of mainly nerve fibres along the main arteries and their connection with the intrinsic ENS (7th-9th week). At 9.5 weeks, however, extrinsic innervation of the colon was not yet complete.

Early development of the extrinsic ENS

The extrinsic ENS and sympatho-adrenal lineage share an early stage in development. Part of the NCCs that exit the closing neural tube migrate between the neural tube and the dermomyotome towards the dorsal aorta (the so-called medioventral pathway; NCCs in Figure 3.11A) (Serbedzija et al., 1990). Schwann-cell precursors (SCPs), which are regarded as neural crest-derived pluripotent cells that appear slightly later (Petersen and Adameyko, 2017), migrate in contact with the ventral roots of the spinal nerves (SCPs in Figure 3.11A). They serve as precursors for the adrenal medulla (Furlan et al., 2017), para-aortic bodies (a.k.a. chromaffin paraganglia) (Kastriti et al., 2019), and part of the intrinsic gut ganglia (Uesaka et al., 2015). We studied 12 CS14 and CS15 embryos, in which we found SCPs transiently present along the vagus nerve (CS14-mid), cervical spinal nerves (C1-C6; CS14-late), and more caudal spinal nerves (CS15). The presence of SCPs on the nerve trunks was short (~1 day) and their density on the spinal nerves highest cranially. Migration of both groups of NCCs towards the dorsal aorta is directed by chemo-attractive factors that include CXCL12 (SDF1) and NRG1 produced by the dorsal aorta, and GDNF and complement component 3A (C3A) produced by gut mesenchyme (Wright and Snider, 1996, Vega-Lopez et al., 2017). The many simultaneously active chemo-attractants may facilitate a more precise final location of the migrating cells (Dyson et al., 2018).

Formation of adrenal medulla and para-aortic bodies

Ventral migration of paravertebral neural crest-derived ganglionic cells was first seen at CS15-early, was most prominent during CS16 and at all stages only observed at and caudal to the developing adrenals. The adrenals were first identifiable between C7 and T5 (CS15-early), “descended” to T4-T9 during CS15-late and CS16, to end up between T11-L3 at and after CS20 (Hikspoors et al., 2015). The cell bodies of the preganglionic nerves to the adrenal medulla locate to the intermediolateral horn of segments T1-L1, whereas the postganglionic nerves originate in sympathetic ganglia at levels T4-12 (Kesse et al., 1988), suggesting that medullar cells become associated with the cortex early during its descent. The location, cellularity, and fate of these SCP-derived ganglionic cells exhibited pronounced and opposite cranial-to-caudal gradients, with cells lateral to the aorta predominating cranially as adrenal medulla and cells ventral to the aorta caudally as para-aortic bodies (Coupland, 1952). The fate of the cranial and caudal ganglionic cells also reflected the observed craniocaudal gradient in cell aggregation: the cells forming the future adrenal medulla retained their scattered

distribution, whereas the para-aortic bodies formed tightly packed, pale-staining cell agglomerates at CS18 ("6 weeks" in Figure 3.11A). The largest para-aortic body, which straddles the aorta cranial to the IMA, is known as Zuckerkandl's organ. Zuckerkandl's organ is largest in infants and regresses in toddlers (Zuckerkandl, 1901, Coupland, 1954). This topographic gradient was also seen in reconstructions of mouse embryos (Furlan et al., 2017) but, as far as we are aware, the mechanism that underlies these opposing gradients is still unknown. In addition, the dorsoventrally oriented nerve fibres were most numerous cranially. In all likelihood, these nerve fibres provide a matrix for SCPs to migrate, since ~80% of the chromaffin cells of the adrenal medulla and pre-aortic paraganglia are formed from such SCPs (Furlan et al., 2017, Kastriti et al., 2019).

Formation of pre-aortic plexuses and extension of nerves along the ventral abdominal arteries

Scattered neural crest-derived cells and nerve fibres form the preaortic nerve plexuses. The plexuses surrounding the CA became identifiable at CS16 and further extended along the CA beyond the cluster of ganglionic cells at CS18, whereas that surrounding the IMA and stem of SMA acquired a similar stage of development at CS20. Accordingly, nerve fibres started to extend along the CA and IMA towards the gut tube well before those along the branches of SMA (Figure 3.11B). A subsequent striking feature was the apparent blockade of nerve extension along the branches of the SMA that passed through the umbilical ring to perfuse the midgut loops in the umbilical hernia. As a result, the extrinsic nerves had reached the gut wall of the non-herniating 1st secondary loop of the small intestine (duodenum and proximal jejunum; (Soffers et al., 2015)) and the hindgut already at CS22 (7.5 weeks), whereas the herniating 2nd to 4th secondary loops of the gut became innervated by extrinsic nerves only after their return into the peritoneal cavity between 9 and 9.5 weeks of development (Soffers et al., 2015). Consequently, the walls of the distal ileum and proximal colon were still not innervated at 9.5 weeks of development (Figure 3.11B). To the best of our knowledge, this regional difference in the development of the extrinsic innervation of the gut has not yet been reported. The delay in innervation may correspond with the rapid growth of the midgut resulting in the formation of loops (Soffers et al., 2015, Ueda et al., 2016). In agreement, the ganglionic cells of the intrinsic ENS begin to form the myenteric plexus at ~CS22 (Okamoto and Ueda, 1967, Fu et al., 2004, Wallace and Burns, 2005), just prior to intestinal return and resolution of the hernia (Soffers et al.,

2015, Nagata et al., 2019). Furthermore, it has been reported, however, that the mitotic index in the ileocoecal region of 11-12 weeks old foetuses was still ~2-fold higher than in the oesophagus or hindgut (Vaos, 1989), while enteric neurons were less developed in the ileum than in adjacent parts of the gut (Tam, 1986). Since cell-cycle withdrawal usually precedes neuronal differentiation in the gut (Pham et al., 1991, Chalazonitis et al., 2008, Bergner et al., 2014), these findings could point at more growth and less differentiation in the herniating part of the midgut.

Timeline of in- and extrinsic innervation of the gut

The timeline of the development of the intrinsic autonomic innervation in experimental animals is known in far greater detail than that of the extrinsic autonomic innervation. In mouse embryos the colonisation of the wall of the gut by caudal vagal neural crest-derived cells is reported to proceed as a unidirectional craniocaudal wave that begins at ED9.5 (Theiler's stage (TS) 15; ~CS13) in the foregut, reaches the proximal small intestine at ED10.5 (TS17; CS14) (Erickson et al., 2014, Hatch and Mukouyama, 2015) and the terminal ileum at ED11.0 (TS18; ~CS15) (Young et al., 1998, Druckenbrod and Epstein, 2005, Anderson et al., 2006). Here, the caudal-ward progression temporarily slows while the NCCs bypass the coecum by taking a transmesenteric route to migrate from the proximal (ileal) to the distal (colonic) limb of the then forming primary intestinal loop (Soffers et al., 2015). Caudal migration resumes at ED12.0 (TS 20; CS17) and reaches the hindgut at ED14.0 (TS22; ~CS21) (Young et al., 1998, Druckenbrod and Epstein, 2005, Anderson et al., 2006, Erickson et al., 2014). The intrinsic NCCs may (Hatch and Mukouyama, 2015) or may not (Delalande et al., 2014) follow the advancing front of the developing enteric capillary plexus. The generally accepted view is that the extension of extrinsic nerves along the intestinal arteries follows the intrinsic innervation in mice with a delay of ~2 days (~3 Carnegie stages) (Erickson et al., 2014, Hatch and Mukouyama, 2015, Uesaka et al., 2016), but has only been documented in detail in the proximal intestine (Hatch and Mukouyama, 2015).

The reported migration of NCCs through the human gut progresses at a similar rate (expressed per developmental stage) as that in mice with a delay of ~1 Carnegie stage (Okamoto and Ueda, 1967, Fu et al., 2004, Wallace and Burns, 2005). This delay can probably be ascribed to a lower sensitivity of the visualization methods for NCCs in humans. In humans, the transformation of the amorphous gut mesenchyme into the layered architecture of the intestinal wall followed the passage of the wave front of NCCs by ~2 Carnegie stages in the small intestine and ~3 stages in the colon (Figure

3.10). We have compared the temporal progress of the transformation of the intestinal wall in human embryos with 22 conventionally stained mouse embryos between ED11 and ED15 (~CS15-~CS22) that were sectioned transversely (8), sagittally (7), or frontally (7). Apart from a slower development of the mural architecture in the stomach and especially the proximal duodenum in mice, the findings were comparable, with a delay of 3-4 Carnegie stages between the passage of the wavefront of neural crest-derived cells and the transformation of the gut wall. Unfortunately, the developmental change in architecture of the midgut wall was too coarse a parameter to allow detection of a migratory delay of the intrinsic ganglionic cells at the ileocoecal junction in human embryos.

Region-specific developmental pattern of the extrinsic innervation

The extrinsic innervation in the thoraco-abdominal cavity can be divided into three subregions that follow the three main ventral branches of the dorsal aorta. Of these, the development of the autonomic plexus surrounding the root of the CA is best studied because of the presence of the developing adrenal glands (Saito and Takahashi, 2015, Furlan et al., 2017). In this region, NCCs migrate to the para-aortic region to form sympathetic ganglia, followed by continued migration of SCP-derived ganglionic cells along spinal nerve fibres, communicating branches, and nerves forming the pre-aortic plexuses (Figure 3.11). SCPs then migrate laterally to the developing adrenal cortex to become the chromaffin cells of the adrenal medulla (Furlan et al., 2017). In contrast to the ganglionic cells, which remain largely confined to the root of the CA, the presumably postganglionic nerve fibres extend further ventrally along the branches of the CA starting at CS16 (39 days) and begin to connect to the intrinsic nerve fibres at CS18 on the stomach (44 days; Figure 3.11A) (Fu et al., 2004, Wallace and Burns, 2005). The coeliac plexus is further characterized by an extensive sympathetic innervation via the greater (segments T5-T9), lesser (segments T10, T11), and least (T12) thoracic splanchnic nerves, which become first identifiable at CS15-late (~37 days). Interestingly, the segments from which the splanchnic nerves derive are persisting landmarks of the “descent” of the coeliac and superior mesenteric arteries and adrenals. In addition to the splanchnic nerves, the vagal nerve contacts the coeliac plexus, starting with the posterior vagal trunk at CS18.

The development of the inferior mesenteric plexus follows the same general pattern as the coeliac plexus with a few notable differences, which correspond to the differentiation of the SCP-derived cells into para-aortic bodies rather than the adrenal

medulla (Kastriti et al., 2019). As mentioned in the previous section, the region of the adrenal medullary cluster of cells gradually changes into one with both scattered neural cells and more tightly packed cells in the para-aortic bodies (Coupland, 1952). The extrinsic nerves that migrate along the IMA take around 1 week [CS20 (49 days) – CS22 (53 days)] to connect to the local intrinsic nerve plexus. The sympathetic lumbar splanchnic nerves that innervate the inferior mesenteric plexus originate in segments L1-L3 and differ from the thoracic splanchnic nerves mainly by their minimal segmental "descent" (Figure 3.11).

Conclusion

The developmental patterns of the extrinsic innervation are repeated in the three subregions of the main ventral aortic branches, but with some region-specific features. These features include the formation of adrenal medulla near the CA, the concentration of para-aortic bodies near the IMA, and the delay in extrinsic innervation in the herniated parts of the midgut.

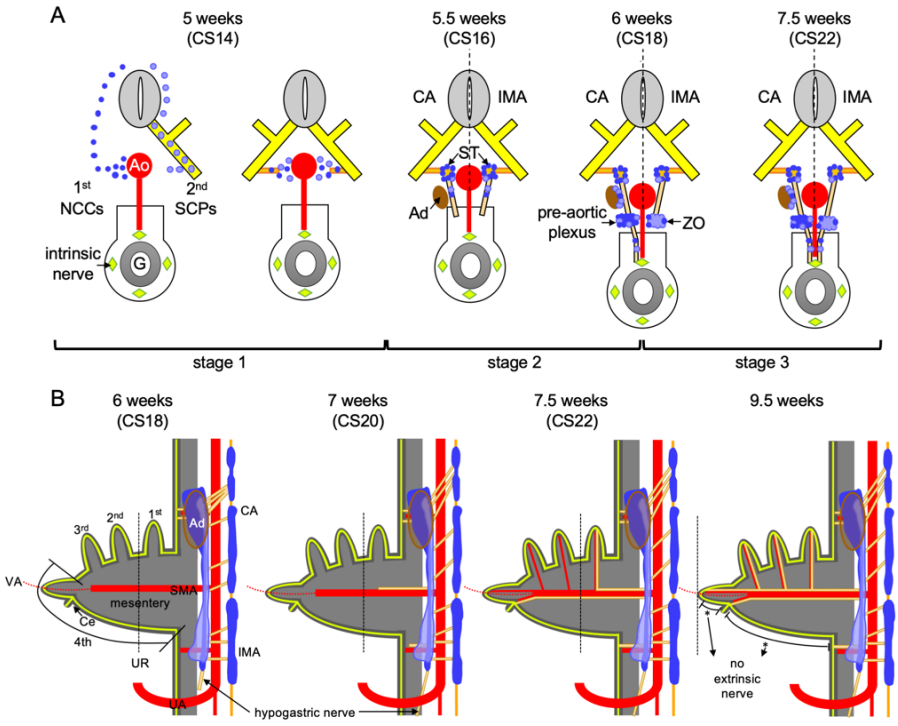

Figure 3.11 **Scheme of the development of the extrinsic innervation in the thoraco-abdominal body cavity.** Panel A shows transverse views with increasing age of the embryo. Starting at 5.5 weeks, the left side of each scheme represents the level of the CA and the right side that of the IMA. At 5 weeks NCCs (blue) or SCPs (light blue) migrate through the mesenchyme or along the ventral roots of spinal nerves (yellow), respectively, to the para-aortic region. Slightly later, nerve fibres extend medially as communicating branches (gold). At 5.5 weeks ganglionic cells either remain in the para-aortic region to form the sympathetic trunk (ST) or migrate further ventrally. Concomitantly, nerve fibres (beige) extend ventrally to form the thoracic and lumbar splanchnic nerves (left and right part of panel, respectively). Note that the adrenal glands (Ad; brown) have formed at the level of the CA. At 6 weeks, most SCP-derived ganglionic cells migrate towards the adrenal cortex to become the adrenal medulla or aggregate to form para-aortic bodies at the level of the IMA. At the level of the CA, pre-aortic nerve fibres extend further ventrally to connect to the intrinsic nerve fibres inside the stomach wall (light green diamonds). At 8 weeks, nerve fibres at the level of the IMA also connect to the intrinsic nerve fibres in the gut wall. Panel B shows the spatiotemporal distribution of the ganglionic cells and extrinsic nerve fibres along the ventral branches of the aorta. From 6 weeks onwards the opposing gradients of the cranially prominent adrenal medulla (blue) and the caudally prominent para-aortic bodies (lighter blue) form. Preganglionic nerve fibres form the thoracic and lumbar splanchnic nerves (beige), while periarterial extrinsic nerve fibres extend and connect with the intrinsic nerve fibres (light green lines). Lumbar nerves extend caudally across the aortic bifurcation into the lesser pelvis (arrow). Nerve fibres surrounding the SMA and IMA extend through the mesentery (grey) to connect to the intrinsic fibres of the 1st secondary intestinal loop, coecum, and hindgut at 8 weeks, and to those of the 2nd and 3rd secondary intestinal loops at 9.5 weeks. Note, however, that extrinsic nerves have not yet appeared in the mesentery of the colon at this stage (asterisks).

Supplemental figures

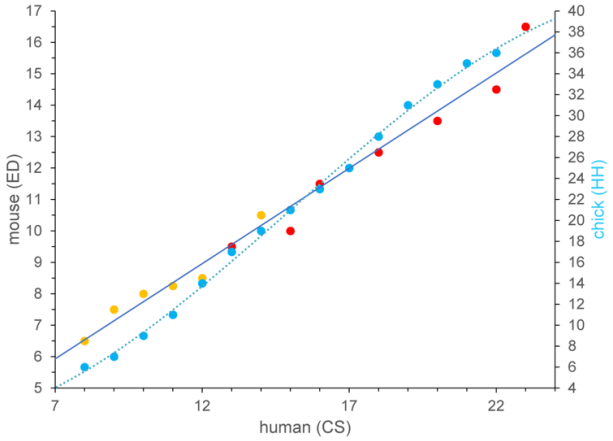

Figure S3.1 Correlation of Carnegie stages of human embryos with days of embryonic development in mouse (Buckingham et al., 2005, Krishnan et al., 2014) or Hamilton-Hamburger stages in chicken embryos (Kirby, 2007).

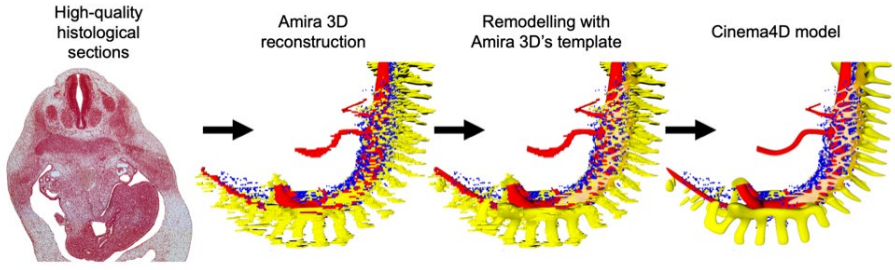

Figure S3.2 Brief procedure of 3D analysis and rendering.

Figure S3.3 Interactive 3D PDFs of the extrinsic innervation in the thoracoabdominal cavity of CS14 – CS16 embryos

Figure S3.4 Interactive 3D PDFs of the extrinsic innervation in the thoracoabdominal cavity of CS18 – CS20 embryos.

Figure S3.5 Interactive 3D PDFs of the extrinsic innervation in the thoracoabdominal cavity of CS22 – 9.5 weeks embryo and foetus.

Note! The interactive 3D-PDFs of the Supplemental Figures can be found in the digital version of the thesis on the USB stick, or directly downloaded from the journal website.

References

Anderson DJ. (1989) The neural crest cell lineage problem: neuropoiesis? *Neuron,* 3, 1-12.

Anderson RB, Stewart AL, Young HM. (2006) Phenotypes of neural-crest-derived cells in vagal and sacral pathways. *Cell Tissue Res,* 323, 11-25.

Bergner AJ, Stamp LA, Gonsalvez DG, et al. (2014) Birthdating of myenteric neuron subtypes in the small intestine of the mouse. *J Comp Neurol,* 522, 514-527.

Bickingham M, Meilhac S, Zaffran S. (2005) Building the mammalian heart from two sources of myocardial cells. *Nat Rev Genet,* 6, 826-35.

Buitrago-Delgado E, Nordin K, Rao A, Geary L, Labonne C. (2015) Shared regulatory programs suggest retention of blastula-stage potential in neural crest cells. *Science,* 348, 1332-5.

Burns AJ, Thapar N. (2006) Advances in ontogeny of the enteric nervous system. *Neurogastroenterol Motil,* 18, 876-887.

Chalazonitis A, Pham TD, Li ZL, et al. (2008) Bone morphogenetic protein regulation of enteric neuronal phenotypic diversity: Relationship to timing of cell cycle exit. *J Comp Neurol,* 509, 474-492.

Chan WH, Gonsalvez DG, Young HM, et al. (2016) Differences in CART expression and cell cycle behavior discriminate sympathetic neuroblast from chromaffin cell lineages in mouse sympathoadrenal cells. *Dev Neurobiol,* 76, 137-49.

Coupland RE. (1952) The prenatal development of the abdominal para-aortic bodies in man. *J Anat,* 86, 357-372.4.

Coupland RE. (1954) Post-natal fate of the abdominal para-aortic bodies in man. *J Anat,* 88, 455-464.

Delande J, Natarajan D, Vernay B, et al. (2014) Vascularisation is not necessary for gut colonisation by enteric neural crest cells. *Dev Biol,* 385, 220-229.

Dong M, Wang X, Chan AK, Burns AJ, Chan WY. (2006) Early Migration of Sacral Neural Crest Cells in Mouse Embryos. *Neuroembryology and Aging,* 4, 189-201.

Druckenbrod NR, Epstein ML. (2005) The pattern of neural crest advance in the cecum and colon. *Dev Biol,* 287, 125-33.

Durbec PL, Larsson-Blomberg LB, Schuchardt A, Costantini F, Pachnis V. (1996) Common origin and developmental dependence on c-ret of subsets of enteric and sympathetic neuroblasts. *Development,* 122, 349-358.

Dyson L, Holmes A, Li A, Kulesa PM. (2018) A chemotactic model of trunk neural crest cell migration. *Genesis,* 56, e23239.

Erickson CS, Lee SJ, Barlow-Anacker AJ, et al. (2014) Appearance of cholinergic myenteric neurons during enteric nervous system development: comparison of different ChAT fluorescent mouse reporter lines. *Neurogastroenterol Motil,* 26, 874-84.

Espinosa-Medina I, Outin E, Picard CA, et al. (2014) Parasympathetic ganglia derive from Schwann cell precursors. *Science,* 345, 87-90.

Fu M, Lui VC, Sham MH, Cheung AN, Tam PK. (2003) HOXB5 expression is spatially and temporarily regulated in human embryonic gut during neural crest cell colonization and differentiation of enteric neuroblasts. *Dev Dyn,* 228, 1-10.

Fu M, Tam PK, Sham MH, Lui VC. (2004) Embryonic development of the ganglion plexuses and the concentric layer structure of human gut: a topographical study. *Anat Embryol (Berl),* 208, 33-41.

Furlan A, Dyachuk V, Katriti ME, et al. (2017) Multipotent peripheral glial cells generate neuroendocrine cells of the adrenal medulla. *Science,* 357, eaal3753.

Furness JB, Callaghan BP, Rivera LR, Cho HJ. (2014) The enteric nervous system and gastrointestinal innervation: integrated local and central control. *Adv Exp Med Biol,* 817, 39-71.

Gershon MD. (1999) The Enteric Nervous System: A Second Brain. *Hosp Pract,* 34, 31-52.

Gianino S, Grider JR, Cresswell J, Enomoto H, Heuckeroth RO. (2003) GDNF availability determines enteric neuron number by controlling precursor proliferation. *Development,* 130, 2187-2198.

Hamburger V, Hamilton HL. (1951) A series of normal stages in the development of the chick embryo. *J Morphol,* 88, 49-92.

Hao MM, FoongJPP, Bornstein JC, et al. (2016) Enteric nervous system assembly: Functional integration within the developing gut. *Dev Biol,* 417, 168-181.

Hatch J, Mukouyama YS. (2015) Spatiotemporal mapping of vascularization and innervation in the fetal murine intestine. *Dev Dyn,* 244, 56-68.

Hikspoors JP, Soffers JH, Mekonen HK, et al. (2015) Development of the human infrahepatic inferior caval and azygos venous systems. *J Anat,* 226, 113-125.

Jessen KR, Mirsky R. (1991) Schwann cell precursors and their development. *Glia,* 4, 185-194.

Kastriti ME, Kameneva P, Kamenev D, et al. (2019) Schwann Cell Precursors Generate the Majority of Chromaffin Cells in Zuckerkandl Organ and Some Sympathetic Neurons in Paraganglia. *Front Mol Neurosci,* 12, 6.

Kesse WK, Parker TL, Coupland RE. (1988) The innervation of the adrenal gland. I. The source of pre- and postganglionic nerve fibres to the rat adrenal gland. *J Anat,* 157, 33-41.

Kirby ML. (2007) *Cardiac development,* New York, Oxford University Press.

Krishnan A, Samtani R, Dhanantwari, P, et al., (2014) A detailed comparison of mouse and human cardiac development. Pediatr Res, 76, 500-7.KRUEPUNGA, N., HIKSPOORS, J. P. J. M., MEKONEN, H. K., et al. 2018. The development of the cloaca in the human embryo. *J Anat,* 233, 724-739.

Kuntz A. (1910) The development of the sympathetic nervous system in mammals. *J Comp Neurol Psycho,* 20, 211-258.

Kuratani S, Kusakabe R, Hirasawa T. (2018) The neural crest and evolution of the head/trunk interface in vertebrates. *Dev Biol,* 444, S60-S66.

Langley JN. (1921) *The autonomic nervous system Part 1*. Cambridge, W. Heffer & sons Ltd, file available on Internet: https://ia800209.us.archive.org/6/items/cu31924024561908/cu31924024561908.pdf.

Lumb R, Tata M, Xu X., et al. (2018) Neuropilins guide preganglionic sympathetic axons and chromaffin cell precursors to establish the adrenal medulla. *Development*, 145, dev162552.

Nagashimada M, Ohta H, Li C, et al. (2012) Autonomic neurocristopathy-associated mutations in PHOX2B dysregulate Sox10 expression. *The Journal of Clinical Investigation,* 122, 3145-3158.

Nagata A, Hatta S, Ji X, et al. (2019) Return of the intestinal loop to the abdominal coelom after physiological umbilical herniation in the early fetal period. *J Anat,* 234, 456-464.

O'Rahilly R, Müller F. (1987) *Developmental stages in human embryos : including a revision of Streeter's "Horizons" and a survey of the Carnegie Collection,* Washington D.C., Carnegie Institution of Washington.

O'Rahilly R, Müller F. (2010) Developmental Stages in Human Embryos: Revised and New Measurements. *Cells Tissues Organs,* 192, 73-84.

O'Rrahilly R, Müller F. (2007) The development of the neural crest in the human. *J Anat,* 211, 335-351.

Okamoto E, Ueda T. (1967) Embryogenesis of intramural ganglia of the gut and its relation to Hirschsprung's disease. *J Pediatr Surg,* 2, 437-443.

Petersen J, Adameyko I. (2017) Nerve-associated neural crest: peripheral glial cells generate multiple fates in the body. *Curr Opin Genet Dev,* 45, 10-14.

Pham TD, Gershon MD, Rothman TP. (1991) Time of origin of neurons in the murine enteric nervous system: Sequence in relation to phenotype. *J Comp Neurol,* 314, 789-798.

Pooh RK, Shiota K, Kurjak A. (2011) Imaging of the human embryo with magnetic resonance imaging microscopy and high-resolution transvaginal 3-dimensional sonography: human embryology in the 21st century. *Am J Obstet Gynecol,* 204, 77.e1-77.e16.

Ruhrberg C, Schwarz Q. (2010) In the beginning: Generating neural crest cell diversity. *Cell Adh Migr,* 4, 622-30.

Saito D, Takahashi Y. (2015). Sympatho-adrenal morphogenesis regulated by the dorsal aorta. *Mech Dev,* 138, 2-7.

Sasselli V, Pachnis V, Burns AJ. (2012) The enteric nervous system. *Dev Biol,* 366, 64-73.

Serbedzija GN, Bronner-Fraser M, Fraser SE. (1992) Vital dye analysis of cranial neural crest cell migration in the mouse embryo. *Development,* 116, 297-307.

Serbedzija GN, Fraser SE, Bronner-Fraser M. (1990) Pathways of trunk neural crest cell migration in the mouse embryo as revealed by vital dye labelling. *Development,* 108, 605-612.

Serbedzija GN, Mcmahon AP. (1997) Analysis of Neural Crest Cell Migration in Splotch Mice Using a Neural Crest-Specific LacZ Reporter. *Dev Biol,* 185, 139-147.

Soffers JH, Hikspoors JP, Mekonen HK, Koehler SE, Lamers WH. (2015) The growth pattern of the human intestine and its mesentery. *BMC Dev Biol,* 15, 31.

Soldatov R, Kaucka M, Kastriti ME, et al. (2019) Spatiotemporal structure of cell fate decisions in murine neural crest. *Science,* 364, eaas9536.

Southwell BR. (2006) Staging of intestinal development in the chick embryo. *The Anatomical Record Part A: Discoveries in Molecular, Cellular, and Evolutionary Biology,* 288A, 909-920.

Streeter GL. (1951) *Developmental horizons in human embryos; age groups XI to XXIII,* Washington, Carnegie Institution of Washington.

Tam PK. (1986). An immunochemical study with neuron-specific-enolase and substance P of human enteric innervation—The normal developmental pattern and abnormal deviations in Hirschsprung's disease and pyloric stenosis. *J Pediatr Surg,* 21, 227-232.

Tiveron MC, Hirsch MR, Brunet JF. (1996) The Expression Pattern of the Transcription Factor Phox2 Delineates Synaptic Pathways of the Autonomic Nervous System. *J Neurosci,* 16, 7649-7660.

Ueda Y, Yamada S, Uwabe C, Kose K, Takakuwa T. (2016) Intestinal Rotation and Physiological Umbilical Herniation During the Embryonic Period. *The Anatomical Record,* 299, 197-206.

Uesaka T, Nagashimada M, Enomoto H. (2015) Neuronal Differentiation in Schwann Cell Lineage Underlies Postnatal Neurogenesis in the Enteric Nervous System. *J Neurosci,* 35, 9879-9888.

Uesaka T, Young HM, Pachnis V, Enomoto H. (2016) Development of the intrinsic and extrinsic innervation of the gut. *Dev Biol,* 417, 158-167.

Vaos GC. (1989) Quantitative assessment of the stage of neuronal maturation in the developing human fetal gut—A new dimension in the pathogenesis of developmental anomalies of the myenteric plexus. *J Pediatr Surg,* 24, 920-925.

Vega-Lopez GA, Cerrizuela S, Aybar MJ. (2017) Trunk neural crest cells: formation, migration and beyond. *Int J Dev Biol,* 61, 5-15.

Wallace AS, Burns AJ. (2005) Development of the enteric nervous system, smooth muscle and interstitial cells of Cajal in the human gastrointestinal tract. *Cell Tissue Res,* 319, 367-382.

Wilson YM, Richards KL, Ford-Perriss ML, Panthier JJ, Murphy M. (2004) Neural crest cell lineage segregation in the mouse neural tube. *Development,* 131, 6153-62.

Wright DE, Snider WD. (1996) Focal expression of glial cell line-derived neurotrophic factor in developing mouse limb bud. *Cell Tissue Res,* 286, 209-217.

Young HM, Hearn CJ, Ciampoli D., et al. (1998) A single rostrocaudal colonization of the rodent intestine by enteric neuron precursors is revealed by the expression of Phox2b, Ret, and p75 and by explants grown under the kidney capsule or in organ culture. *Dev Biol,* 202, 67-84.

Young HM, Hearn CJ, Farlie PG, et al. (2001) GDNF Is a Chemoattractant for Enteric Neural Cells. *Dev Biol,* 229, 503-516.

Zuckerkandl E. (1901) Über nebenorgane des sympathicus im retroperitonealraum des menschen. *Verh Anat Ges,* 15, 97-107.

Chapter 4
Extrinsic innervation of the pelvic organs in the lesser pelvis of human embryos

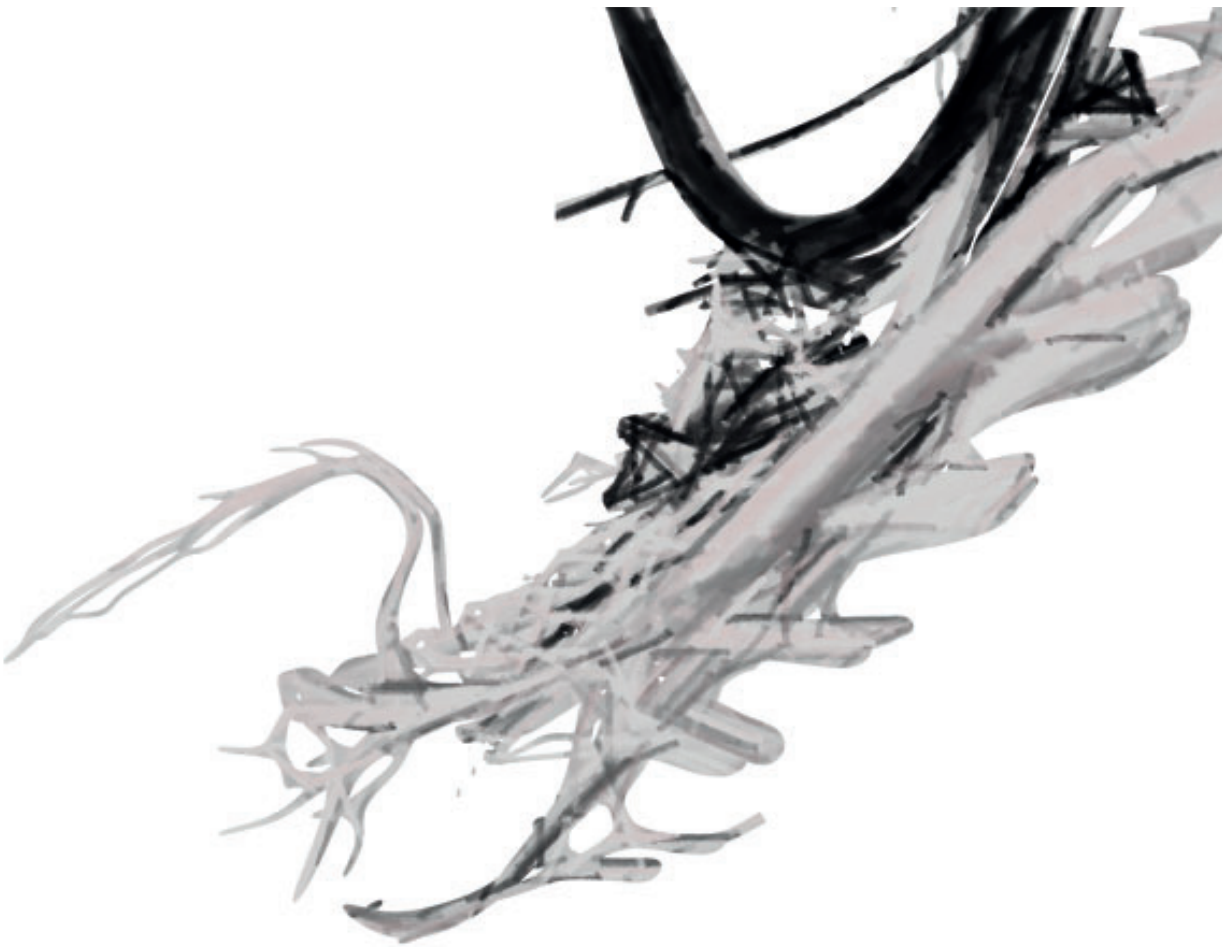

Nutmethee Kruepunga, Jill P.J.M. Hikspoors, Cindy J.M. Hülsman,
Greet M.C. Mommen, S. Eleonore Köhler and Wouter H. Lamers
Journal of Anatomy (2020); 237(4): 672-688

Abstract

Realistic models to understand the developmental appearance of the pelvic nervous system in mammals are scarce. We visualised the development of the inferior hypogastric plexus (IHP) and its preganglionic connections in human embryos of 4-8 weeks post-fertilisation using Amira 3D-reconstruction and Cinema 4D-remodelling software. We defined the embryonic lesser pelvis as the pelvic area caudal to both umbilical arteries and containing the hindgut. Neural crest cells (NCCs) appeared dorsolateral to the median sacral artery near vertebra S1 at ~5 weeks and had extended to vertebra S5 one day later. Once para-arterial, NCCs either formed sympathetic ganglia or continued to migrate ventrally to the pre-arterial region, where they formed large bilateral inferior hypogastric ganglionic-cell clusters (IHGCs). Unlike more cranial pre-aortic plexuses both IHGCs did not merge, because the "pelvic pouch", a temporary caudal extension of the peritoneal cavity, interposed. Although NCCs in the sacral area started to migrate later, they reached their pre-arterial position simultaneously with the NCCs in the thoracolumbar regions. Accordingly, the superior hypogastric nerve (SHN), a caudal extension of the lumbar splanchnic nerves along the superior rectal artery, contacted the IHGCs only one day later than the lumbar splanchnic nerves contacted the inferior mesenteric ganglion. The SHN subsequently splits up to become the superior hypogastric plexus. The IHGCs had two additional sources of preganglionic innervation, of which the pelvic splanchnic nerves arrived at ~6.5 weeks and the sacral splanchnic nerves only at ~8 weeks. After all preganglionic connections had formed, separate parts of the IHP formed at the bladder neck and distal hindgut.

Introduction

The pelvic organs, which occupy the lesser or "true" pelvis, are innervated by the autonomic nervous system. The caudal portion of the vagal neural crest cells is the major source of neural crest-derived cells (NCCs) of the intrinsic ENS (Durbec et al., 1996, Anderson et al., 2006, Simkin et al., 2013, Espinosa-Medina et al., 2017). However, studies in chicken (Le Douarin and Teillet, 1973, Burns and Le Douarin, 1998) and subsequently in rodents (Serbedzija et al., 1991, Anderson et al., 2006) have shown that NCCs that originate distal to vertebral level L1-2, which corresponds to somite 28 in chicken (Le Douarin and Teillet, 1973) and somite 24 in mice (Dong et al., 2006), contribute to the mature ENS of the colon. The timeline of the development and distribution of these sacral neural crest cells in mammals is described in most detail for rodents. In mice, these cells emigrate from the neural tube at embryonic day (ED) 9.0-9.5, aggregate in the para-aortic region at ED10.5-11.0, and form the pelvic ganglia ventrolateral to the hindgut at ED11.5-12.5. From here they enter the wall of the gut or base of bladder at ED13.5-14.0 and have colonized the entire postcoecal gut at ED14-14.5. Soon thereafter, differentiation into intramural ganglia and the formation of smooth muscle layers begins (Serbedzija et al., 1991, Kapur, 2000, Dong et al., 2006, Wang et al., 2011, Erickson et al., 2012). Vagal NCCs emigrate from the neural tube at ED8.0-8.5, enter the gut at ED9.5, arrive at the coecum at ED10.5, bypass the coecum via the dorsal mesentery to move into the postcoecal gut at ED12.5, reach the midpoint of the colon by ED13.5 and the hindgut at ED14.5 (Kapur et al., 1992, Durbec et al., 1996, Young et al., 1998, McKeown et al., 2001, Druckenbrod and Epstein, 2005, Nishiyama et al., 2012). These data imply that the sacral NCCs take 2-3x longer to move from the neural tube to the wall of the gut, but migrate ~2-fold faster through the postcoecal gut than the vagal NCCs.

A number of studies address sacral NCC migration (Kuntz, 1952, Kimmel and McCrea, 1958, Arango-Toro and Domenech-Mateu, 1993, Okamoto and Ueda, 1967) and pelvic nerve development (Browne, 1953, Pearson and Sauter, 1970, Arango-Toro and Domenech-Mateu, 1993, Kinugasa et al., 2008) in human embryos. From these studies, the general picture emerges that the development of the pelvic nervous system in humans is similar to that in rodents. Unfortunately, relatively few embryos were studied and the staging was rather imprecise. Perhaps even more limiting is the fact that these studies did not provide spatial models (apart from a single, elegant wax model of an 8-weeks old embryo in (Arango-Toro and Domenech-Mateu, 1993)). It is,

therefore, difficult to appreciate topographic relations between gut, nerves, and pelvic organs.

In the present study, we investigated the development of the inferior hypogastric plexus and its preganglionic connections with the central nervous system: the hypogastric, pelvic and sacral splanchnic nerves. Recently, the pelvic splanchnic nerves were shown to be developmentally and phenotypically sympathetic (Espinosa-Medina et al., 2016), defining all three inputs as sympathetic. For this reason, we carefully mapped the timeline of their appearance and contact with the bilateral pelvic ganglionic cell clusters. Another reason to map the development of the hypogastric plexus and nerves was the difference in the timelines of the vagal (cranial) and sacral (caudal) contributions to colonic innervation. We further defined the topographical boundaries of the lesser pelvis in the embryo.

Materials and methods

Embryos

This study was undertaken in accordance with the Dutch regulations for the proper use of human tissue for medical research purposes. Well-preserved anonymous human embryos and foetuses, donated for scientific research, of the historical collections of the Departments of Anatomy and Embryology, Leiden University Medical Centre (LUMC), the Amsterdam University Medical Centres, location Academic Medical Centre (AMC), and Radboud University, Nijmegen, The Netherlands, and of the University of Göttingen, Germany (Blechschmidt Collection; https://doi.org/10.3249/ugoe-publ-2) were studied (Table 4.1). In addition, digital images of carefully staged human embryos from the Carnegie collection (Washington D.C., USA) were included from the Digitally Reproduced Embryonic Morphology (DREM) project (http://virtualhumanembryo.lsuhsc.edu).

Table 4.1 **Metadata of human embryos and foetuses that were studied.** The estimated post-fertilisation ages of the embryos are based on (O'Rahilly and Muller, 2010). The additions "early", "mid" and "late" are meant to indicate that, within these stages, the development of the gut and enteric nervous system of "late" embryos was more advanced than that of "early" embryos. The corresponding age was chosen from the range of developmental days attributed to that stage (O'Rahilly and Muller, 2010). CS14 in particular is noted for its remarkable number of developmental events. Abbreviations: AC, alum cochineal (i.e., carmine); AMC, Academic Medical Centre; CS, Carnegie stage; DREM, Carnegie collection from the Digitally Reproduced Embryonic Morphology project; Göttingen, Department of Anatomy and Embryology, Göttingen; H&A, Haematoxylin and Azophloxine; H&E Haematoxylin and Eosin; LUMC, Leiden University Medical Centre; PAS, Periodic acid–Schiff stain; RadboudMC: Radboud Medical Centre.

Stage	Days	Embryo	Fixation	Staining	Plane	Source
CS10	28	S6330	Formalin	Ehrlich's H	Transv	DREM
CS11	29	S6344	Formalin	CA	Transv	DREM
CS12	30	S8943	Zenker's fix	H & E	Transv	DREM
CS13	32	S836	$HgCl_2$	CA	Transv	DREM
CS14-early	33	S2201	Formalin	H & A	Transv	AMC
CS14-mid	34	S5029	Formalin	H & A	Sagittal	AMC
CS14-mid	34	S168	Bouin's fix	H & E	Transv	LUMC
CS14-mid	34	1950-09-13		H & E	Sagittal	Göttingen
CS14-late	35	1958-12-22		H & E	Sagittal	Göttingen
CS14-late	35	1961-06-13		H & E	Transv	Göttingen
CS14-late	35	S6502	Souza's fix	H & E (or + Ag)	Transv	DREM
CS15-early	36	S721	Zenker's fix	H & E (or + Ag)	Transv	DREM
CS15-early	36	S79	Formalin	H & E	Transv	LUMC
CS15-early	36	1945-10-26		H & E	Transv	Göttingen
CS15-early	36	1957-10-31		H & E	Transv	Göttingen
CS15-late	37	S2213	Formalin	H & A	Transv	AMC
CS16	39	S5032	Formalin	H & A	Sagittal	AMC
CS16	39	S6517	Corrosive CH_3COOH	CA	Transv	DREM
CS16	39	S39	Formalin	H & E	Transv	LUMC
CS17	41	S6520	Corrosive CH_3COOH	CA (or + Ag)	Transv	DREM
CS18	44	S97	Bouin's fix	H & E	Transv	LUMC
CS18	44	S4430	Corrosive CH_3COOH	CA	Transv	DREM
CS19	46	S9325	Acetic formalin	Azan & Ag	Transv	DREM
CS20	49	S2025	Bouin's fix	H & A	Transv	AMC
CS20	49	S462	Formalin	CA	Transv	DREM
CS20	49	S34	Formalin & Bouin's fix	H & E	Sagittal	LUMC
CS21	51	S4090	Formalin	CA	Transv	DREM
CS22	53	S48	Formalin	H & E	Transv	LUMC
CS22	54	S983	Formalin	H & E	Transv	DREM
CS23	56	S4141	Formalin	H & A	Transv	AMC
CS23	56	S9226	Formalin	Azan	Transv	DREM
CS23	56	S88	Formalin & Bouin's fix	H or PAS or Azan	Sagittal	RadboudMC

Image acquisition, 3D reconstruction, and visualization

Human embryos between 4–8 weeks of post-fertilisation development were investigated. The modified O'Rahilly's criteria were used to define the Carnegie Stage

(CS) of development and post-fertilisation age [(O'Rahilly and Muller, 2010); Table 4.1]. A graph relating the Carnegie stages of human embryos to days of development in mice or Hamilton-Hamburger (HH) stages (Hamburger and Hamilton, 1951) in chicken are found in Supplemental Figure S4.1. Serial sections from the named historical collections were digitised with an Olympus BX51 or BX61 microscope and the Dotslide program (Olympus, Leiderdorp, The Netherlands) to provide high-resolution digital images. Serial sections of the Blechschmidt collection were digitized with a Zeiss Axio Scan.Z1 (Carl Zeiss Microscopy, Jena, Germany). All digital images were transformed into greyscale 'JPEG' format and imported into Amira3D (version 6.5; FEI Visualization Sciences Group Europe, Merignac Cedex, France). The imported images were aligned automatically with the least-squares function and then manually optimised by correction for the embryonic curvature with the aid of photographs and magnetic resonance images (MRI) of the same stages of human embryos (Pooh et al., 2011). Structures of interest were segmented manually and used to generate three-dimensional shapes with the Amira3D program. To eliminate the distracting noise in the Amira3D output due to section processing and stacking, Amira3D polygon meshes were exported via 'vrml export' to Cinema 4D (version R21; MAXON Computer GmbH, Friedrichsdorf, Germany) and remodelled using the Amira3D model as a template. Concurrent visualization of the Amira3D template and the remodelled Cinema4D model in Cinema 4D was used to verify the accuracy of the Cinema4D models (Supplemental Figure S4.2). The Cinema4D models were transferred via 'wrl export' to Adobe Acrobat version 9 (http://www.adobe.com) to generate interactive 3D Portable Device Format (PDF) files, which are a user-friendly format for 3D visualization (Supplemental Figures S4.3 and S4.4). We mostly refer in the text to the Figures to relate histology to developing structures, but encourage the reader to simultaneously inspect the interactive PDFs, because their rotational options ("live" images) allow a much better understanding of the complex local topography than the "still" pictures in the images. Note that the orientation of the 3D models is aligned according to the (vertical) axis through segments (vertebrae) T1 and L1.

Terminology

Intestinal development in avian (Southwell, 2006) and mammalian embryos (Soffers et al., 2015) proceeds in a similar fashion, with the midgut or primary loop extending into the coelomic cavity of the umbilical cord as the so-called "umbilical hernia". The main differences appear to be the formation in birds of only a single (duodeno-jejunal)

secondary loop and 2 coecal diverticula, whereas 4 secondary gut loops and a single coecal diverticulum form in mammals. In both avian and mammalian embryos the cells of the vagal neural crest colonise both “pre-umbilical” and “post-umbilical” parts of the gut, with the position of the vitelline duct forming the landmark between “pre-“ and “post-“. The sacral neural crest cells arise distal to vertebral level L1-2 in both birds and mammals (Le Douarin and Teillet, 1973, Dong et al., 2006) and only colonise the “post-umbilical” gut in a caudocranial gradient that becomes progressively steep during development (Le Douarin and Teillet, 1973, Burns and Le Douarin, 1998, Anderson et al., 2006). Whereas the avian vitelline duct remains present and patent until hatching (Esteban et al., 1991), the mammalian vitelline duct already disappears at ~CS15 in rodent (Lamers et al., 1987) and human (Soffers et al., 2015) embryos. Due to the disappearance of the vitelline duct in mammalian embryos, the cranial boundary of the post-umbilical gut can no longer be delineated accurately. Accordingly, the part of the gut colonized by sacral neural crest cells is variously referred to as hindgut (Young and Newgreen, 2001, Wang et al., 2011), post-coecal hindgut (McKeown et al., 2001), or colo-rectum (Young and Newgreen, 2001). In agreement with our accompanying study, we will identify the mammalian equivalent of the avian post-umbilical gut as the distal loop of the midgut and hindgut.

Some terminology is confusing because embryonic and definitive structures differ markedly in appearance. Relevant for the present study are the superior hypogastric nerve and plexus, the inferior hypogastric (ganglionic) cluster and plexus, and the hindgut and rectum. The superior hypogastric plexus acquires its definitive configuration upon the division of the single large splanchnic nerve into many smaller nerve strands during CS18-20. Similarly, we describe the inferior hypogastric plexus as a cluster of ganglionic cells until it becomes populated by nerves at CS20.

Our detailed study of the extrinsic innervation of the caudal part of the gut showed that the junction of the mid- and hindgut corresponded with the location of the stem of the inferior mesenteric artery (IMA) rather than the cranial end of its left colic branch. The stem of the IMA branches from the aorta at vertebral level T12-L1 during CS15 and has descended to L2-3 at CS20 (Evans, 1912). This level corresponds, in turn, with the cranial boundary of the sacral neural crest (Le Douarin and Teillet, 1973; Dong et al., 2006) and, as we will show, with the rectosigmoidal junction rather than the transverse colon in the adult. We will describe the development of the junction between mid- and hindgut trunk in more detail in a separate study.

Results

In Kruepunga et al. (accompanying study), we identified neural crest-derived ganglionic cells in the thoraco-lumbar region by their topography and intense staining properties. In this study, we investigated the appearance and migration of neural crest-derived cells in the caudal-most portion of the body, the lesser pelvis.

Boundaries of the lesser pelvis in the embryo

We define the lesser pelvis in the embryo as the pelvic area caudal to both umbilical arteries (Figure 4.1). The umbilical arteries branched away from the dorsal aorta at the level of lumbar vertebra 4 (L4), irrespective of the developmental stage of the embryo. On their course to the umbilical cord, the umbilical arteries passed the insertion of the Wolffian ducts into the urogenital sinus and the allantois laterally (Supplemental Figures S4.2 and S4.3). Until CS15-late (~37 days of development), the plane through both umbilical arteries (UA in Figure 4.1) was almost perpendicular to the frontal plane through the dorsal aorta. Between CS16 and CS23 (39-56 days of development), the angle between both planes gradually disappeared, concomitant with the unfolding of the caudal part of the body axis. The caudal unfolding involved the lumbar and sacral regions until CS17 and was confined to the sacral region between CS17 and 10 weeks of development (Kruepunga et al., 2018). A striking feature of the umbilical arteries was the absence of extrinsic enteric nerves on their ventral side (not shown). Up to and including CS15 (~37 days of development), the umbilical arteries, therefore, also impressed as a barrier between the abdominal and pelvic nerves, but concomitant with the local unfolding of the body axis, the bifurcation was crossed ventrally by the developing hypogastric nerve.

Mesenchymal cells caudolateral to the umbilical arteries started to condense to form the cartilaginous template of the hip bones at CS16 (Figure 4.1). The position of the hip bones also followed the unfolding process up to CS20, as can be deduced from the change in position of the pubococcygeal line through the pubic arch and vertebra S5 (blue lines in Figure 4.1). At 7.5 weeks (CS22), the proximal portion of the umbilical arteries, therefore, occupied the position of the common iliac arteries (Figure 4.1), which defines the upper boundary of the lesser pelvis in the adult. Of relevance for their landmark function, the umbilical arteries produced caudolateral, but no cranioventral branches. The marked curvature of the umbilical arteries in the sagittal plane at CS22, with the most caudal point lateral to the bladder trigone (the most

cranial region of the urogenital part of the cloaca (Kruepunga et al., 2018)) showed that the straightening of the body axis in the late embryonic period represented axial growth of the dorsal part of the body, which was matched ventrally by the development of the ventral body wall from the lower thoracic dermomyotomes (Mekonen et al., 2015) and the fundus of the bladder from the allantois (van der Putte, 2004, Kruepunga et al., 2018). We observed the configuration of the umbilical arteries as shown in panel E in another CS22 embryo, while the configuration as shown in panel F was seen all 4 CS23 embryos studied, showing that the formation of the infra-umbilical ventral body wall proceeds rapidly.

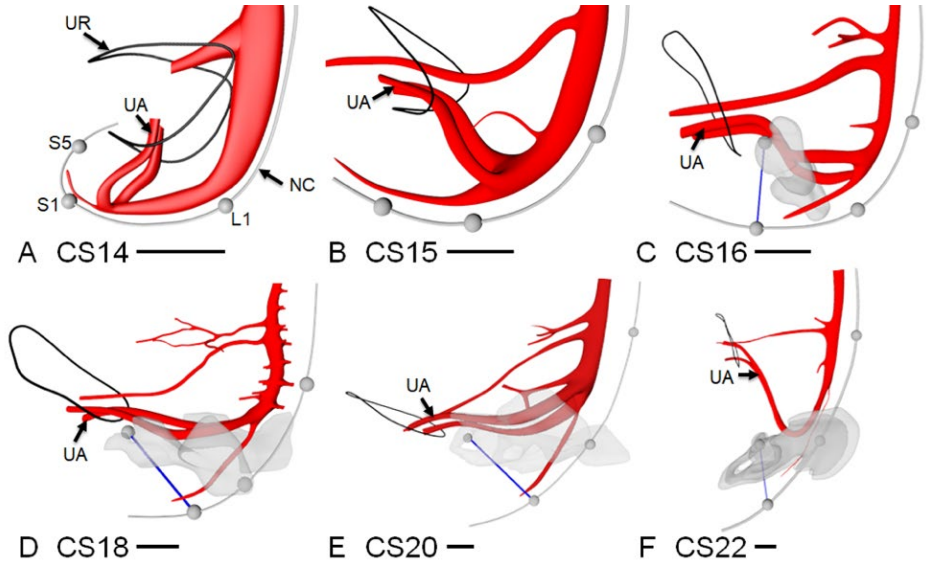

Figure 4.1 **The course of the umbilical arteries defines the upper boundary of the lesser pelvis.** Panels A-F show side views of the dorsal aorta and its major ventral branches between CS14 and CS22, with the notochord representing the embryonic curvature and the grey spheres marking segments L1, S1 and S5. At CS14 (33 days; panel A) the plane through the bifurcation of the umbilical arteries was orthogonal to a frontal plane through the aorta. As the caudal body axis unfolded (Kruepunga et al., 2018), the angle between both planes straightened to 160-170o at CS22. Concomitantly with the unfolding of the embryonic axis, the line through the subpubic arch and vertebra S5 unfolded from CS16 onwards (panels C-F). Note that the unfolding process plateaus in the lumbar region at CS17, but continues in the sacral region. Bars = 500 µm.

We reported earlier that one of the features that accompanied early herniation of the midgut (CS14 and CS15) was a thinning of the dorsal mesentery between the superior and inferior mesenteric arteries (Soffers et al., 2015, Hikspoors et al., 2019).

The thin base of the midgut mesentery and the thick base of the hindgut mesentery are well visible in Supplemental Figure S4.4 (asterisks in panels B and C). This feature persisted the next three weeks (Figures 4.3E and 4.4F-H) and demarcated the transition of the herniated colon and the non-herniating hindgut (CS16-20). At CS20, when the IMA had branched into the left colic and superior rectal arteries, the stem of the IMA pointed to the transition of herniated and non-herniated parts of the caudal gut (Supplemental Figure S4.3B). At CS23, a leftward-oriented colic loop with a thin mesentery started to form ventral to the left gonad. Caudally, the return of this loop to the midline co-located with the thickening and shortening of the dorsal mesentery, with the plane through both umbilical arteries described in the previous paragraph, and with the appearance of the superior hypogastric nerve at the intestinal base of the dorsal mesentery that will be described in the paragraph on the "Formation of the nerve fibre network of the inferior hypogastric plexus". These three features characterize the plane that represents the superior boundary of the lesser pelvis.

Formation of the inferior hypogastric ganglionic-cell cluster

In the pelvic area neural crest-derived cells were first found dorsolaterally to the median sacral artery near level S1 in CS15-early embryos (~36 days of development; blue dots in Figure 4.2A and blue arrows in Figure 4.2C). Topographically, these ganglionic cells were a caudal continuation of similarly located ganglionic cells in the lumbar region and, accordingly, passed the bifurcating umbilical arteries dorsally (Supplemental Figure S4.2A, CS14-early). At CS15-late (~37 days), the dorsolateral neural crest-derived cells had extended their presence to level S5 (blue dots in Figure 4.2F and blue arrows in Figure 4.2H,J). The most cranial portion of these cells began to consolidate as ganglia of the sympathetic trunk along the median sacral artery (blue arrows in Figure 4.2H). Furthermore, many scattered cells had now accumulated ventrally to the median sacral artery and laterally to the hindgut, where they occupied on both sides a triangular area with its base dorsally between S1 and S5, and its apex ventrally near the entrance of the common nephric portion of the Wolffian ducts into the urogenital sinus. These ganglionic cells were found caudal to the umbilical arteries and did, therefore, not extend into the abdominal cavity (Figure 4.2F). Their ventral extension was situated laterally to the pelvic pouch of the coelomic cavity. This pelvic pouch located in the urorectal septum and surrounded the hindgut ventrally and laterally down to the cloaca ((Kruepunga et al., 2018); Supplemental Figure S4.2B), so that the ventrolateral ganglionic cells were not in direct contact with the wall of the

hindgut. At CS16 (~39 days of development, Figure 4.3A-C), ganglionic cells had advanced further ventrally along the lateral side of the pelvic pouch to form the left- and right-sided, sagittally oriented inferior hypogastric ganglionic cell clusters (IHGCs; Figure 4.3B). The presence of the pelvic pouch explains why both IHGCs persisted as separate entities throughout subsequent development. More cranially, in a plane perpendicular to the notochord at level S1 and through the junction of mid- and hindgut, cells of the IHGCs that remained located mediodorsally to the hindgut connected to the well-developed superior hypogastric nerve (SHN in Figure 4.3A; asterisk in Figure 4.4A), which is the common caudal continuation of the left- and right-sided lumbar splanchnic nerves along the superior rectal branch of the inferior mesenteric artery. Strikingly, no caudal extensions of ganglionic cells toward the cloaca were seen. Ganglionic cells dorsolaterally to the median sacral artery had now aggregated to such an extent that they could be identified as the sacral sympathetic trunk (Figure 4.3A).

At CS18 (~44 days of development), the cell density in the IHGCs had further increased (Figure 4.3D) and came to resemble the preaortic ganglia seen more cranially (Kruepunga et al, accompanying study). Cranially, the continuity between the left and right ganglionic-cell clusters and the large medial superior hypogastric nerve was now firmly established (Figure 4.3D-F). While the dorsal boundary of the IHGCs retained its position dorsolateral to the hindgut, its ventral boundary advanced into the mesenchymal niche between pelvic coelomic pouch and urogenital sinus (Figure 4.3D-F). Laterally, these ganglionic cells were flanked by the levator muscle, which had become identifiable as a well-defined condensation of mesenchyme flanking the gut between S2 and S5 (LAM; transparent brown in Figure 4.3D). At CS20 (~49 days of development), the developmental events described for CS18 had continued to advance, with as major feature a quantitative increase in the density of ganglionic cells in both IHGCs (Figure 4.5A-C). In CS22 embryos (~53 days of development; Figure 4.5D-G), the left and right IHGCs were still separate, but each cluster had fragmented (blue dots in panels 4.5D and E). Its middle portion, which occupied the niche between the urogenital sinus ventrally and pelvic coelomic pouch at the level of the entrance of the Wolffian and Müllerian ducts into the urogenital sinus dorsally, had evolved as the biggest and densest (blue dots in panel 4.5E, blue arrows in panels 4.5F and G). Because each IHGC now also incorporated nerve fibres, it could be labelled the inferior hypogastric or pelvic plexus (blue dots and beige network in Figure 4.5D). The more cranial and caudal portions of the IHGCs formed small clusters near the ureteric

entrance into the bladder and around the lower part of the rectum, respectively (Figure 4.5D). Of interest, the caudal extension of the IHGC reached the rectal wall caudal to the pelvic coelomic cavity, which at this stage had started to regress in cranial direction (Hikspoors et al., 2019).

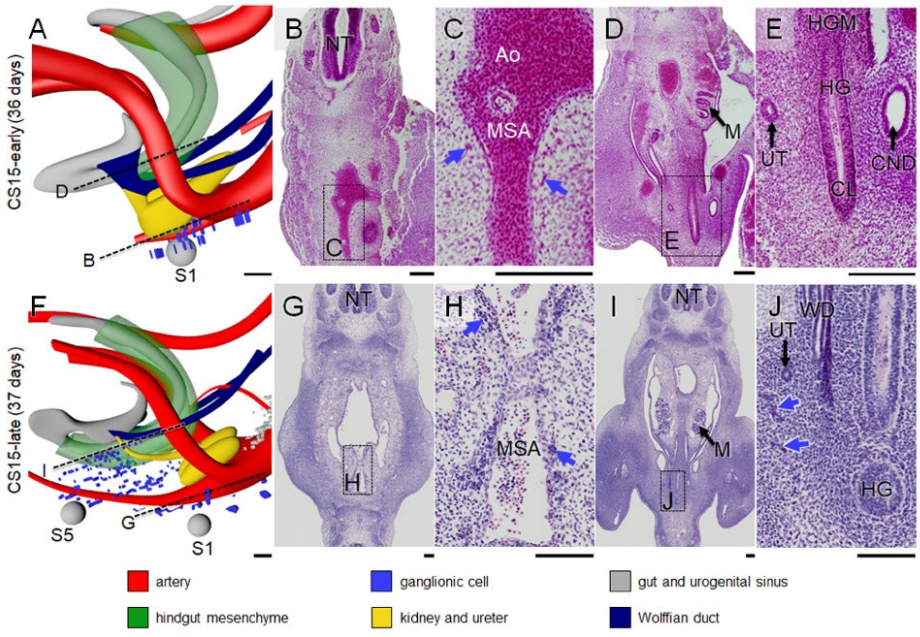

Figure 4.2 **Migration of neural crest-derived ganglionic cells at CS15.** Panels A and F show side views of the lesser pelvis of CS15-early and CS15-late embryos, respectively. Panels B, D, G, I show histological sections and panels C, E, H, J magnifications of the respective boxes. At CS15-early (panel A) ganglionic cells (blue dots in panel A, blue arrows in panel C) migrate ventrally to the para-arterial region at level S1 (grey sphere). One day later (CS15-late) such ganglionic cells have migrated further ventrally towards the hindgut (blue arrows in panel J) and further caudally to level S5. The median sacral artery is considered as the caudal extension of the dorsal aorta. Bars = 100 µm.

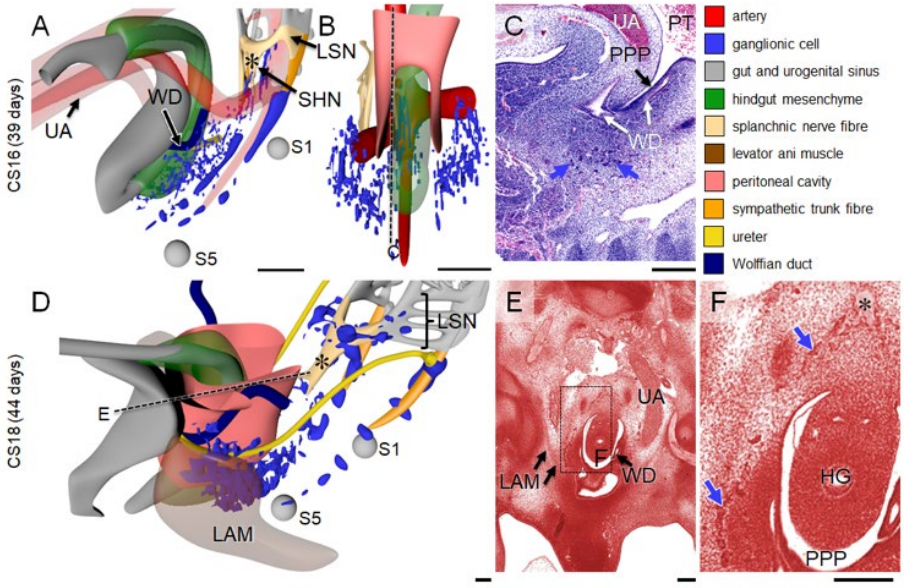

Figure 4.3 **Appearance of the inferior hypogastric ganglionic cell cluster.** Panels A and D show side views of the lesser pelvis of CS16 and CS18 embryos, respectively. Panel B shows a frontal view of the CS16 reconstruction to show that both IHGCs contact each other dorsal to the hindgut. Panels C and E show histological sections and panel F a magnified view of the box in E. At CS16 the bulk of ganglionic cells is present as bilateral clusters (blue dots in panels A, B and blue arrows in panel C) that have migrated ventrally as far as the entrance of the Wolffian ducts. The levator ani muscle formed at CS18 as a mesenchymal condensation lateral to IHGCs. Bars = 200 µm.

Formation of the nerve fibre network of the inferior hypogastric plexus

Nerve fibres were first observed in the lesser pelvis at CS16, when the superior hypogastric nerve formed as a median continuation of both lumbar splanchnic nerves along the superior rectal artery. This nerve formed cranial to the bifurcation of the umbilical arteries, but began to extend caudally across the bifurcation towards the cranial part of both IHGCs described in the previous section (asterisks in Figure 4.4A,E). In CS18 embryos, the superior hypogastric nerve had increased in diameter and length, so that it now passed the aortic bifurcation. This single nerve trunk (asterisks in Figure 4.4B,F) bifurcated just caudal to the umbilical arteries to form both hypogastric nerves that each connected to the corresponding IHGC. Nerve fibres were still absent from the IHGCs at this stage (Figure 4.3D-F). Subsequently (CS20), the superior hypogastric nerve at the intestinal base of the dorsal mesentery split into a bundle of smaller nerves that began to resemble the superior hypogastric plexus (asterisks in Figure

4.4C,G). Fragmentation of the nerve into a plexus continued through CS22 (asterisks in Figure 4.4D,H).

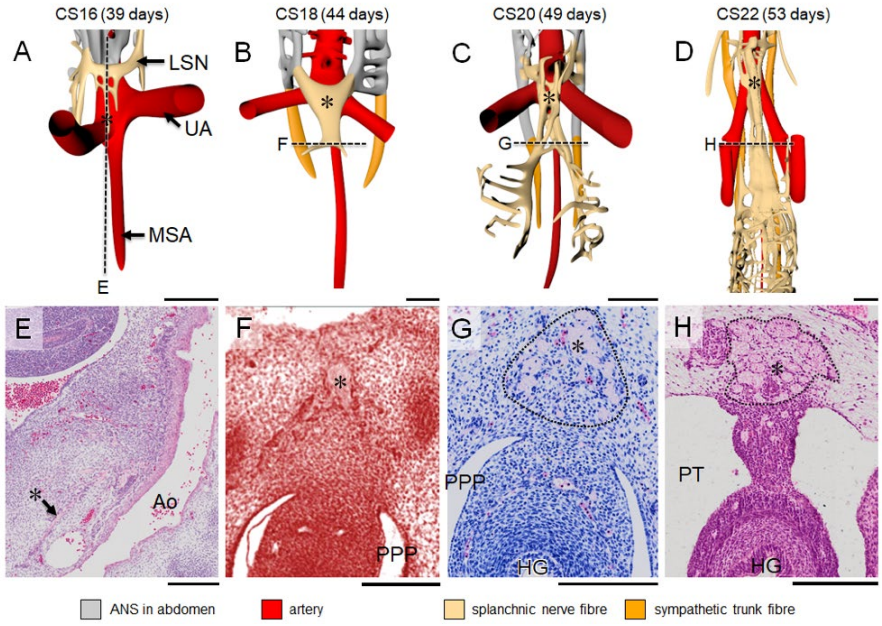

Figure 4.4 **The superior hypogastric nerve is a caudal extension of the lumbar splanchnic nerves.** Panels A-D show frontal views of nerve fibres and arteries in CS16 -CS22 embryos, while panels E-H show histological sections along the black dotted lines in panels A-D. At CS16 nerve fibres of the lumbar splanchnic nerves (LSN) extended caudally across the bifurcation of the umbilical arteries as the superior hypogastric nerve (SHN; asterisks in panels A,E). The SHN extended caudally as a single trunk that bifurcated caudally (asterisks in panels B,F) at CS18. From CS20 onwards the single SHN trunk split into multiple nerve fibres (asterisks in panels C,D,G,H, with the contour of the original nerve outlined as dots), that are known as the superior hypogastric plexus. Bars A-D = 500 µm, E-H = 200 µm.

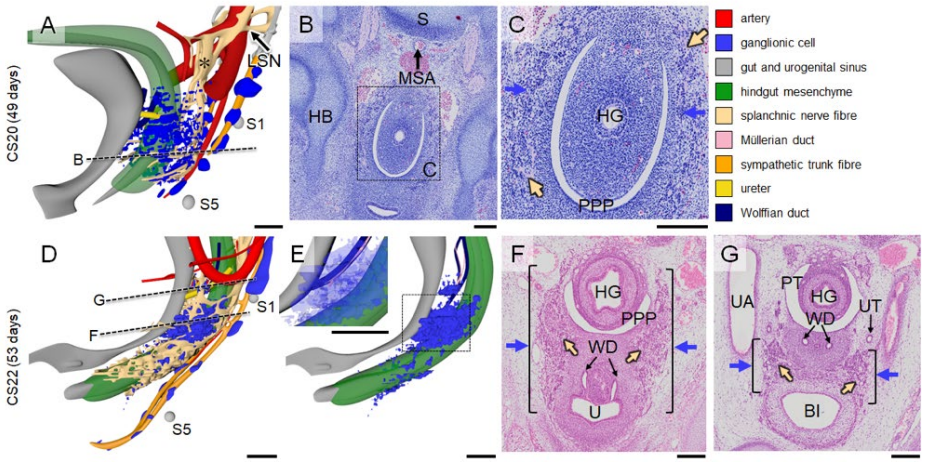

Figure 4.5 **Extension and incorporation of nerve fibres mark the formation of the inferior hypogastric plexus.** Panels A,D,E show oblique views of the lesser pelvis at CS20 (A) and CS22 (D,E). Panels B and F show histological sections and their magnified views (C,G) indicated by rectangles. At CS20, the lumbar splanchnic nerve (asterisk in panel A) continued caudally as the superior hypogastric plexus that extended into the IHGCs (beige and blue arrows in panel C, respectively). At CS22 the IHGCs (blue dots in panel E and blue arrows in panels F) were largest at the level of the entrance of the Wolffian duct into the urogenital sinus. The inferior hypogastric plexus formed cranial extensions along bladder neck (brackets in panels F,G) and caudal extensions into the perirectal mesenchyme (Figure 4.5D,E). Note that the mesenchyme nor the nerves reach the dorsal cloaca (grey tip extending beyond hindgut mesenchyme). Bars A,D,E = 500 µm, B,C,F,G = 200 µm.

Concomitantly, medial branches of sacral spinal nerves S2-4, known as the pelvic splanchnic nerves, extended medially towards the IHGCs at CS16 (yellow arrows in Figure 4.6A, C). The pelvic splanchnic nerves reached the IHGCs at CS18 (yellow arrows in Figure 4.6D, F) and lined up with nerves in the IHGCs in CS20 embryos (Figure 4.7A). The resulting network of fibres inside the left and right IHGCs had, therefore, transformed these clusters into the left and right inferior hypogastric plexuses (Figure 4.5A-C). Furthermore, nerve fibres from the sympathetic trunk had started to extend ventrally as the sacral splanchnic nerves and connected to the inferior hypogastric plexus at CS22 (orange arrowheads in Figure 4.8D,F,J).

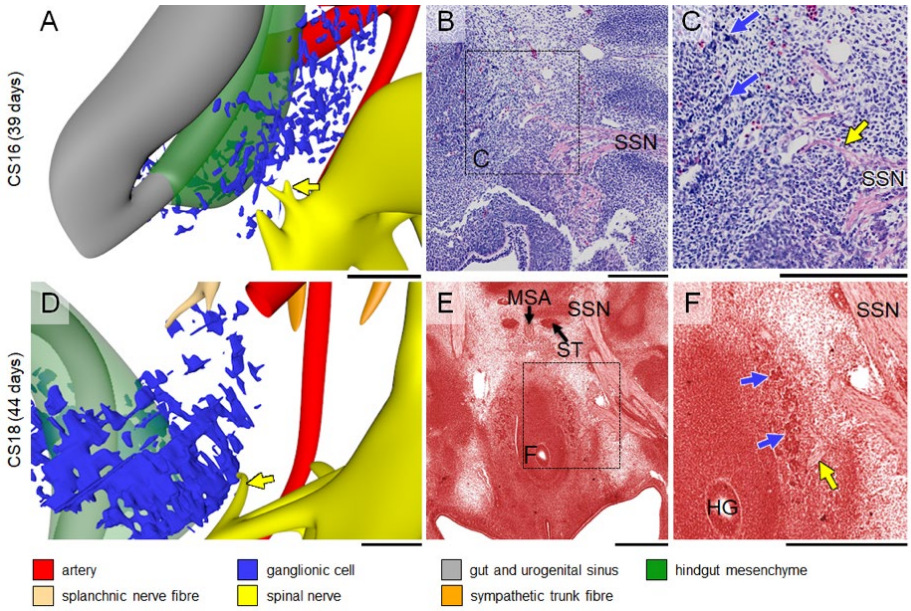

Figure 4.6 **Appearance of the pelvic splanchnic nerves.** Panels A,D show the pelvic splanchnic nerves as small medial branches (yellow arrows) of the sacral spinal nerves, while panels B,C,E,F show histological sections and magnified views indicated by rectangles. At CS16 the pelvic splanchnic nerves had not yet reached the IHGCs (blue dots in panel A and blue arrows in panel C), whereas at CS18 they had (yellow arrows in panels D and F). Bars A - D = 200 µm, E,F = 500 µm.

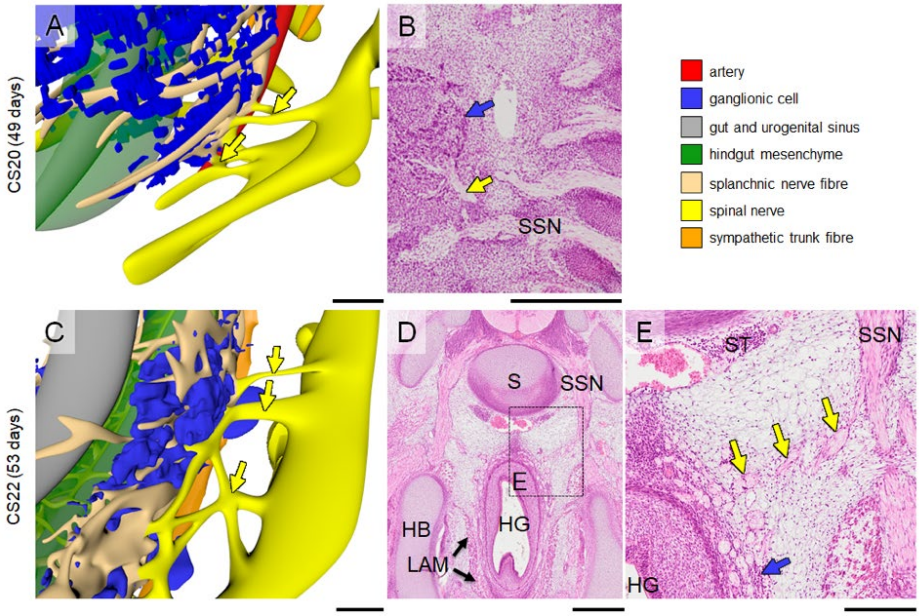

Figure 4.7 **Extension of the pelvic splanchnic nerves.** Panels A,C show pelvic splanchnic nerves, while panels B,D,E show histological sections and a magnified view (rectangle). At CS 20 and CS22 pelvic splanchnic nerves (yellow arrows in panels B and E) had penetrated into the inferior hypogastric ganglionic-cell clusters (IHGCs; blue dots in panels A,C and blue arrows in panels B and E). Bars A,C,E = 200 µm, B,D = 500 µm.

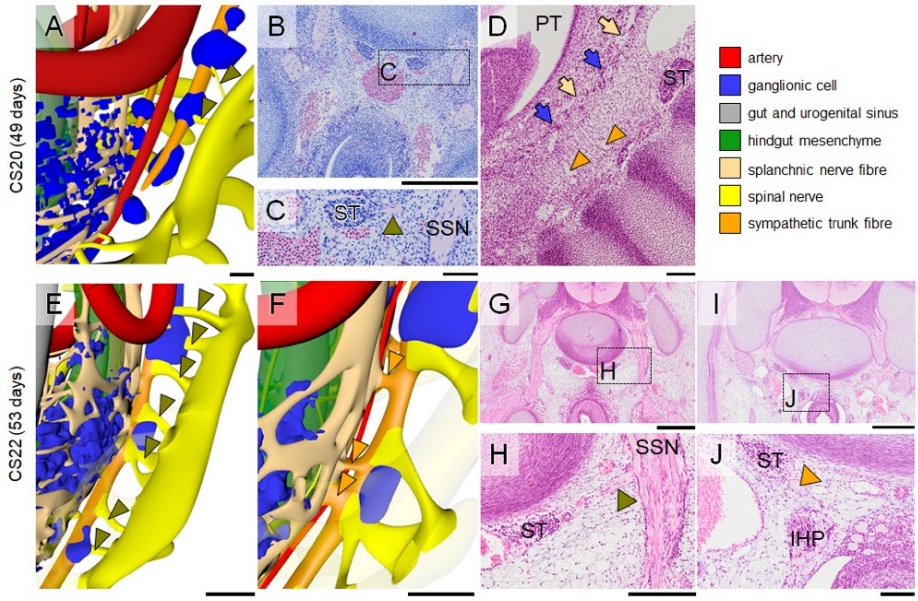

Figure 4.8 **Formation of sacral communicating branches and splanchnic nerves.** Panels A,E,F show connections between the sympathetic trunk ganglia and the sacral spinal nerves (communicating branches; olive green arrowheads in A, E) and with the inferior hypogastric plexus (sacral splanchnic nerves; orange arrowheads in F). Panels B-D and G-J show histological sections and their magnified views (rectangles). The communicating branches in panels C and H are indicated with olive-green arrowheads, while the sacral splanchnic nerves are indicated with an orange arrowhead (panel J). Bars A,E,F,H = 200 µm, B,G,I = 500 µm C,D,J,K = 100 µm.

The eighth embryonic week (CS20 - CS23) was characterized by a pronounced increase in size and density of the network of nerve fibres in the inferior hypogastric plexuses. At the end of the 8th week there were three groups of nerve fibres associated with the inferior hypogastric plexus: hypogastric nerves originating in the lumbar splanchnic nerves (segments L1, 2) and accompanying the superior rectal artery (Figure 4.4), pelvic splanchnic nerves originating in the sacral spinal nerves (segments S2-4; Figures 4.6 and 4.7), and sacral splanchnic nerves originating in the sympathetic trunks (originating from segments L1, 2, but passing through the sacral sympathetic trunk; Figure 4.8 and Supplemental Figure S4.3C). The nerve fibres of the inferior hypogastric plexus extended cranially to the developing muscular layer of the bladder fundus as vesical plexus and caudally to the distal hindgut (but not dorsal cloaca) as rectal plexus, while tiny fibres near the entrance of the Wolffian and Müllerian ducts extended into the wall of the urogenital sinus as uterovaginal or prostatic plexus (Supplemental Figure S4.3C). The bifurcation of the superior hypogastric plexus into a

left- and right-sided hypogastric nerves was located at the level of S1. In addition, many left-right connections between both sides of the inferior hypogastric plexus had formed on the dorsal side of the distal hindgut. The sacral spinal nerves clearly had medial extensions (pelvic splanchnic nerves) to the inferior hypogastric plexus (yellow arrows in Figure 4.7C,E) and ventral extensions that formed the pudendal nerve (Supplemental Figure S4.3C). In addition, extrinsic enteric nerve fibres (beige arrows) within the inferior hypogastric plexus had connected intrinsic enteric nerve fibres (light green arrows) in the urogenital and hindgut mesenchyme (Figure 4.9). While the network of nerve fibres in the wall of the hindgut was well defined (Figure 4.9C), such a network of nerve fibres was not present in the wall of e.g. the duodenum (Figure 4.9H). At CS22 and CS23, no differences in pelvic innervation between male and female embryos were apparent.

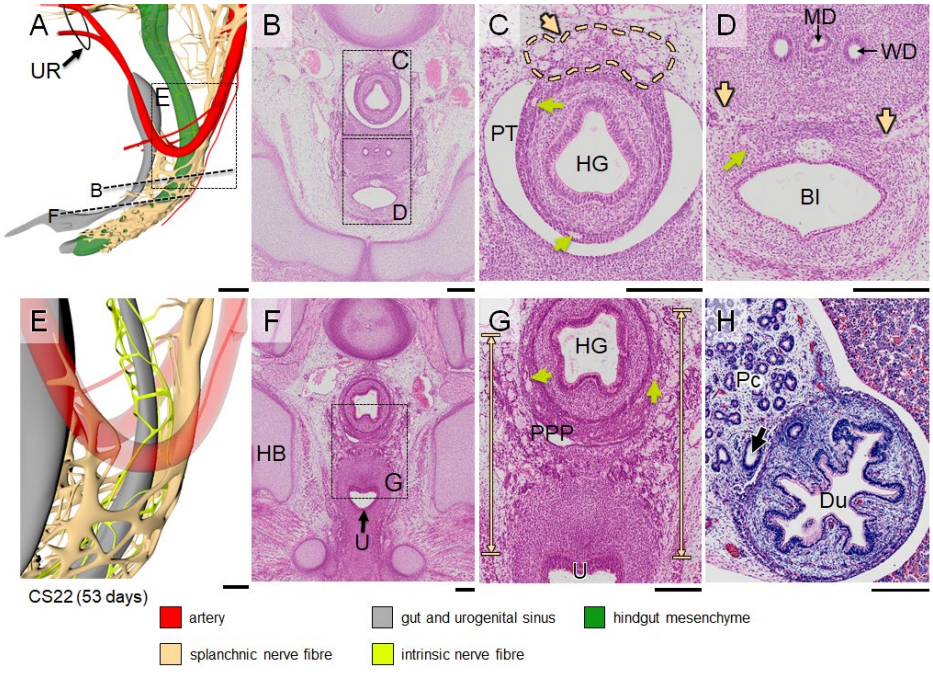

Figure 4.9 **Connection of extrinsic and intrinsic enteric nerve fibres in the lesser pelvis.** Panels A,E show nerve fibres in the lesser pelvis and a magnified view (rectangle). Panels B-D and F-G show histological sections from the levels indicated by dotted lines in panel A and magnified views (rectangles). Extrinsic enteric nerve fibres (beige arrows) extend into the mesenchymal cuffs of the hindgut, where intrinsic nerve fibres (light green arrows) form an intrinsic nervous network (panels C, G). In contrast, such well-developed nerves are near absent in the duodenum (panel H; arrow indicates common bile duct). Bars A = 500 µm, B-G = 200 µm.

Discussion

We studied the development of the extrinsic innervation in the lesser pelvis to illustrate and explain its spatiotemporal population with autonomic ganglionic cells and nerve fibres (for a pictorial summary, see Figures 4.10 and 4.11).

Boundaries of the lesser pelvis

The hip bone and sacrum are well established lateral boundaries of the lesser pelvis and can also be used as such in embryos, but landmarks for the cranial and caudal boundaries of the lesser pelvis are less evident. In the present study we have identified the umbilical arteries as landmark for its cranial boundary. Their position corresponds with the cranioventral brim of the hip bones. Two landmarks reveal the developmental changes in the hip and the lesser pelvis: the apparent rotation of the so-called "pubococcygeal line" between the inferior rim of the pubic symphysis and the caudal end of the sacrum (Fielding, 2002) and the changing proximal course of the umbilical arteries both show that the caudal spine and its surroundings straighten by the unfolding of their previously pronounced kyphosis (Figure 4.1) (Kruepunga et al., 2018). Based on the pronounced increase in width of the dorsal mesentery, the transition between mid- and hindgut co-localizes with the position of the umbilical arteries. This finding indicates that the transition between the herniating and non-herniating parts of the colon has to be located at the transition of sigmoid colon into rectum.

The caudal boundary of the lesser pelvis is formed by the muscles of the pelvic floor (external urethral sphincter, levator ani, and coccygeus), of which the sphincter and coccygeus muscles are remarkably well developed in 8-week embryos (see also (Tichý, 1989, Koch and Marani, 2007)). The boundary function of the LAM is also clear from the course of the nerves surrounding it: nerve fibres medial to the LAMs extend only inside the lesser pelvis, whereas nerve fibres on its lateral side (the pudendal nerve) extend to the mesenchymal structures outside the lesser pelvis (Supplemental Figure S4.3C).

Similarities and differences in the developing extrinsic innervation of the gut in the abdomen and lesser pelvis

A number of instructive schematic accounts of the development of the autonomic enteric innervation of thorax and abdomen are available, in particular for its intrinsic component (e.g. (Lake and Heuckeroth, 2013, Saito and Takahashi, 2015, Espinosa-

Medina et al., 2017, Dyson et al., 2018, Simkin et al., 2019)) and, albeit to a lesser extent, also for its extrinsic component (Hatch and Mukouyama, 2015, Uesaka et al., 2016)(Kruepunga et al., accompanying study). However, graphic accounts of the ENS in the lesser pelvis (e.g. (Wang et al., 2011)) are rare. Although the contribution of Schwann cell precursors (SCPs) to the chromaffin cells of the autonomic nervous system in the abdomen was recently estimated to be ~80% (Furlan et al., 2017, Kastriti et al., 2019) and that to the intrinsic neurons of the colon ~20% (Uesaka et al., 2015), we do not know at present if, and if so, to what extent SCPs contribute to the IHGCs. In addition, the identity of the sacral outflow was recently questioned and reclassified as sympathetic, that is, similar in structure and developmental origin to the thoracic and lumbar autonomic nervous system (Espinosa-Medina et al., 2016). We, therefore, compared the timing and sequence of appearance and differentiation of the building blocks (ganglionic cells and nerve fibres) that formed the abdominal and pelvic pre-aortic ganglia in human embryos.

Migratory timeline of neural crest-derived ganglionic cells (Figures 4.10 and 4.11)

Cell tracing studies showed that the ganglionic cells in the lesser pelvis arise from sacral neural crest cells in mammalian embryos (Serbedzija et al., 1991, Kapur, 2000, Anderson et al., 2006, Wang et al., 2011, Wiese et al., 2017). In human embryos, the thoracolumbar neural crest emerges during CS12 and the sacral neural crest during CS13, that is, with a ~2-day delay (O'Rahilly and Müller, 2007). If the dorsal aorta and median sacral artery can serve as homologous landmarks, neural crest cells at both locations first aggregate laterally to the dorsal aorta (para-aortic cluster) and then ventrally to the aorta (pre-aortic cluster). Thoracolumbar neural crest cells begin to migrate to the para-aortic region during CS13 (~31 days) and arrive at CS14-early (~33 days). These neural crest cells either settle there to form sympathetic ganglia 3 days later [CS15-early (~36 days)] or continue migration to arrive at the pre-aortic region 4 days later [CS15-late (~37 days)] and form the pre-aortic plexuses. Neural crest cells in the lesser pelvis arrive in the para-arterial region only at CS15-early (~36 days) to form sympathetic ganglia. However, the NCCs that continue to migrate ventrally need just ~1 day to reach the pre-arterial region at CS15-late (~37 days) and form the IHGC (equivalent to pre-aortic ganglia). This comparison shows that the timeline of the migration of ganglionic cells in the thoracolumbar and sacral region differs, but that the migratory pathway and time of arrival at their destination are very similar.

Differences in innervation of the neural crest-derived ganglionic-cell aggregates (Figures 4.10 and 4.11)

The pre-aortic plexuses in the thoracolumbar region are irregularly shaped median masses of neural crest-derived ganglionic cells that surround the roots of the ventral branches of the dorsal aorta. In addition, agglomerates of the SCP subgroup of neural crest-derived cells are found in association with the coeliac and inferior mesenteric plexuses as the (developing) chromaffin cells of the adrenal medulla and para-aortic bodies, respectively (Furlan et al., 2017, Kastriti et al., 2019). These two agglomerates differ in that the chromaffin-cells of the adrenal medulla are positioned dorsolaterally to the coeliac plexus, whereas those of the para-aortic bodies touch or merge in the midline (Supplemental Figure 4A,B), with very few para-aortic bodies found distal to the umbilical bifurcation (Coupland, 1952)(Kruepunga et al, accompanying study). The preganglionic nerve fibres that innervate the pre-aortic ganglionic-cell agglomerates arrive at CS15 late (~37 days of development; Figure 4.10). The IHGCs form at the same developmental stage as, and are contacted only slightly later (CS16; ~39 days) by the superior hypogastric nerve than the inferior mesenteric cluster by the lumbar splanchnic nerves (Kimmel and McCrea, 1958, Arango-Toro and Domenech-Mateu, 1993). In fact, our reconstructions show that the superior hypogastric nerve develops as an unpaired mediocaudal extension of the lumbar splanchnic nerves along the superior rectal artery (CS16-20), which explains the common origin of the lumbar splanchnic and superior hypogastric nerves in segments L1 and L2. At CS20, the superior hypogastric nerve has split up into several and at CS22 in many separate nerve fibres. This remarkable splitting up of a compact nerve into a distributed plexus may well explain its morphological variability and many alternate names in the adult (Davis, 1934).

Apart from the hypogastric nerves, the IHGC has two additional sources of preganglionic innervation, of which the pelvic splanchnic nerves arrive at CS18 (~44 days) and the sacral splanchnic nerves only at CS22 (~53 days). Phenotypically and developmentally, the prenatal pelvic splanchnic nerves were recently characterized as sympathetic rather than parasympathetic (Espinosa-Medina et al., 2016), so of comparable phenotype as the hypogastric and sacral splanchnic nerves. Our findings refine earlier timelines in human embryos (Kuntz, 1952, Kimmel and McCrea, 1958, Arango-Toro and Domenech-Mateu, 1993) and better allow comparison with data obtained in experimental animal models, such as mice. However, cause(s) and

consequence(s) of this phased innervation by phenotypically similar preganglionic nerves remain to be clarified.

Differences in topography of the abdominal and pelvic plexuses

Compared to the midline pre-aortic abdominal ganglia, the bilateral presence of the inferior hypogastric plexuses is striking. This pronounced topographic difference can be ascribed to the pelvic pouch, a caudal extension of the peritoneal cavity between the hindgut and the urogenital sinus that extends down to the muscular pelvic floor. The temporary presence of this narrow pouch in human embryos was first described by Cunéo and Veau, 1899 and confirmed by Tobin and Benjamin, 1945, and Uhlenhuth et al., 1948. It surrounds the ventral and lateral sides of the hindgut, leaving a wide dorsal mesentery. The pelvic pouch, like the nearby vaginal process in the groin, obliterates exclusively in hominids and not in quadrupeds. This process proceeds from caudal to cranial and begins in the 8th week (Kruepunga et al., 2018, Hikspoors et al., 2019) to reach its definitive position at ~11 weeks development (Tobin and Benjamin, 1945, Uhlenhuth et al., 1948, Fritsch, 1988). Obliteration of the pouch may protect bipedal hominids from rectal prolapse, which is quite common in quadrupeds (Pettan-Brewer and Treuting, 2011). Accordingly, a straight course of the sigmoid colon with a correspondingly short mesentery (both embryonic features) often co-occur with a persisting pelvic coelomic pouch and enterocele (Baessler and Schuessler, 2006). The presence of a dorsal mesentery allows extrinsic nerve fibres, which guide ganglionic cells towards and into the wall of the hindgut, to enter the wall of the hindgut dorsally (Erickson et al., 2012), but the ganglionic cells that eventually form the inferior hypogastric cluster, have to migrate laterally to the pelvic pouch, ureters and Wolffian ducts towards their future location (Figures 4.2-4). Even though present only temporally, the pelvic pouch, together with the dense mesenchyme surrounding the urogenital sinus, prevent the left- and right-sided ganglionic cells to form a single midline structure. Denonvilliers' fascia will form at the site of adhesion and fusion of the mesothelial layers of the pelvic pouch. This configuration also explains why, if possible, dissection anterior (ventral) to Denonvilliers' fascia is to be preferred over posterior dissection during a total mesorectal excision (Fang et al., 2019).

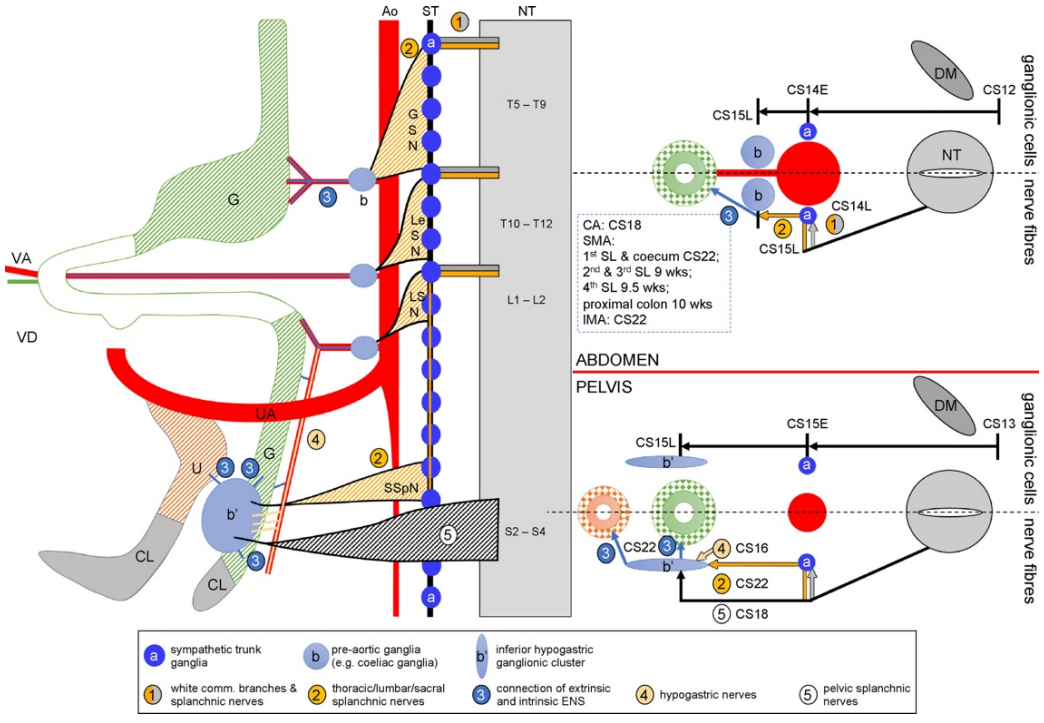

Figure 4.10 **Preganglionic innervation of pre-aortic plexuses; comparison of the thoracolumbar and pelvic areas.** The left panel shows a scher branches of the aorta and median sacral artery (red), the gastrointestinal tract (green) and cloaca (grey). The scheme shows t autonomic connections (coded in hatched orange: greater splanchnic nerves (GSN; T5-T9); lesser and least splanchnic nerves (LeS lumbar splanchnic nerves (LSN; L1-L2)) to the pre-aortic ganglia (grey-blue ovals "b"). Preganglionic nerves pass the sympathetic tru synapsing. The inferior hypogastric plexus ("IHP" in large grey-blue oval) is innervated by the superior hypogastric nerve ("4"); the nerves (SSpN; also coded in hatched orange); and the pelvic splanchnic nerves ("5"; S2-4; coded in hatched black). The right par timeline of the migration of the ganglionic cells (upper half of schemes) and that of the nerve fibres (lower half of schemes) in the scheme) and pelvis (lower scheme). Both schemes show that the ganglionic cells migrate equally fast to the pre-arterial locations in t pelvis, but that it takes the nerve fibres in the pelvic area longer to reach their targets.

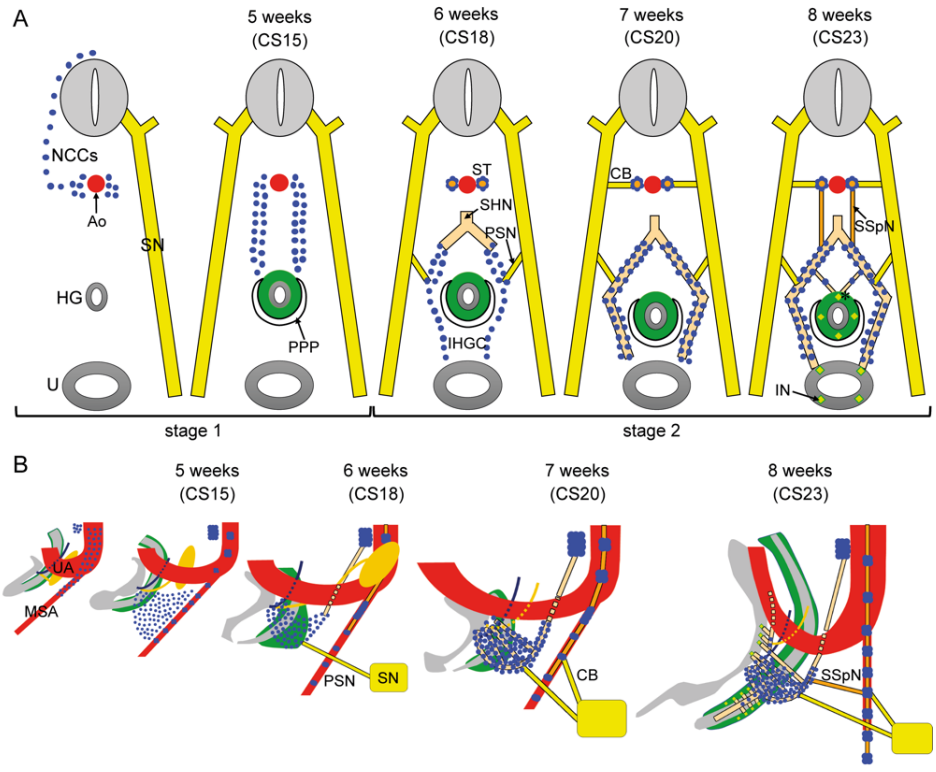

Figure 4.11 **Timeline of neural crest-cell migration to ganglionic cell clusters in, and preganglionic innervation of the inferior hypogastric plexus**. Panel A shows schematic transverse sections at different developmental timepoints. The development of the inferior hypogastric plexus can be divided into (1) migration of neural crest cells (blue dots) towards their para-arterial (CS14 and CS15) and pre-arterial positions (CS15 and CS16); and (2) association of nerve fibres with the inferior hypogastric ganglionic cell cluster. The first nerve to arrive is the superior hypogastric nerve at CS16, followed by the pelvic splanchnic nerves at CS18 and the sacral splanchnic nerves at CS22. By that time small nerve fibres had entered the gut wall via the dorsal mesentery of the hindgut and contacted intrinsic enteric nerves. Panel B shows schematic side views of the formation of the inferior hypogastric plexus. NCC-derived ganglionic cells migrate to the para- and pre-arterial positions in during CS14 and CS15, are contacted at CS16 by the superior hypogastric nerve, by the pelvic splanchnic nerves at CS18, and by the sacral splanchnic nerves at CS22. Starting at CS18, nerves penetrate the ganglionic-cell cluster to form the inferior hypogastric plexus, while nerves and ganglionic cells begin to extend from this plexus along the bladder wall and the caudal hindgut.

Limitations of the study

The present study provides detailed reconstructions of the autonomic nervous system in the developing pelvis in 6 human embryos between 5 and 8 weeks of with development. Although one can object that 6 models cannot visualize all of the ENS in

the developing embryo, we were able to provide a continuous account of the developmental appearance of relevant structures. A valid question is, nevertheless, whether all variation is accounted for. Although the answer is obviously “no”, differences between specimens could usually be explained as differences in degree of development rather than deviation from the expected morphology. The most important limitation of the present series is probably that the models still contain mistakes. Because the models are made in the software program Cinema4D, such mistakes can be corrected relatively easily.

Conclusion

The extrinsic innervation, both ganglionic cells and nerve fibres, in the lesser pelvis is organised in a similar fashion as that in its abdominal counterpart. Its three topographically separate preganglionic connections can be ascribed to differences in developmental timeline and its bilateral appearance to local peritoneal topography. Up to and including CS23 pelvic innervation is phenotypically indifferent with respect to sexual dimorphism.

Supplemental figures

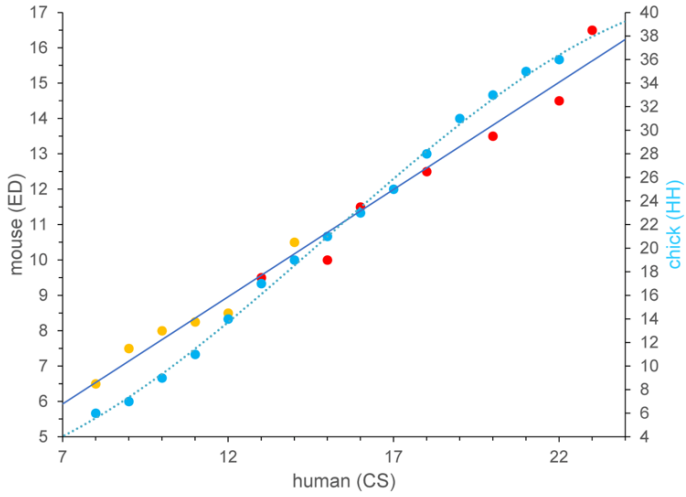

Figure S4.1 Correlation of Carnegie stages of human embryos with days of embryonic development in mouse (Buckingham et al., 2005, Krishnan et al., 2014) or Hamilton-Hamburger stages in chicken embryos (Kirby, 2007).

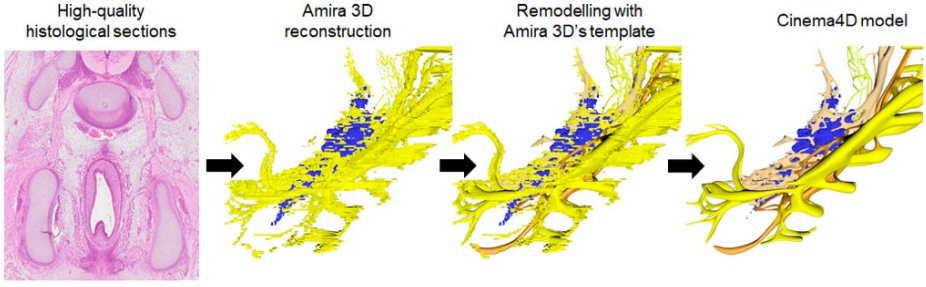

Figure S4.2 Brief procedure of 3D analysis and rendering.

Figure S4.3 3D PDFs of the lesser pelvis of a CS15-early, CS15-late, and CS16 human embryo.
Figure S4.4 3D PDFs of the lesser pelvis of a CS18, CS20, and CS22 human embryo.

Note! The interactive 3D-PDFs of the Supplemental Figures can be found in the digital version of the thesis on the USB stick, or directly downloaded from the journal website.

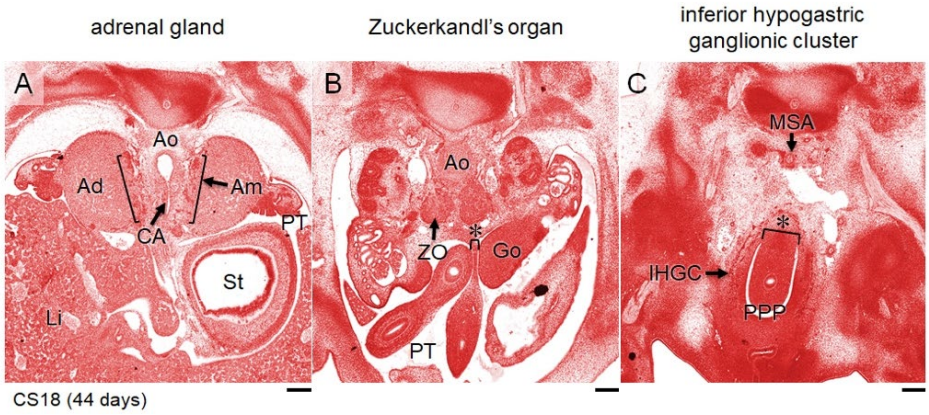

Figure S4.5 Topographic comparison of the levels of the adrenal gland, Zuckerkandl's organ and inferior hypogastric ganglionic-cell cluster in CS18.

References

Anderson RB, Stewart AL, Young HM. (2006) Phenotypes of neural-crest-derived cells in vagal and sacral pathways. *Cell Tissue Res,* 323, 11-25.

Arango-Toro O, Domenech-Mateu JM. (1993) Development of the pelvic plexus in human embryos and fetuses and its relationship with the pelvic viscera. *European journal of morphology,* 31, 193-208.

Baessler K, Schuessler B. (2006) Anatomy of the sigmoid colon, rectum, and the rectovaginal pouch in women with enterocele and anterior rectal wall procidentia. *Clin Anat,* 19, 125-9.

Browne MJ. (1953) A study of the sacral autonomic nerves in a chick and a human embryo. *The Anatomical Record,* 116, 189-203.

Buckingham M, Meilhac S, Zaffran S. (2005) Building the mammalian heart from two sources of myocardial cells. *Nat Rev Genet,* 6, 826-35.

Burns AJ, Le Douarin NM. (1998) The sacral neural crest contributes neurons and glia to the post-umbilical gut: spatiotemporal analysis of the development of the enteric nervous system. *Development,* 125, 4335.

Coup;and RE. (1952) The prenatal development of the abdominal para-aortic bodies in man. *Journal of Anatomy,* 86, 357-372.4.

Cuneo B, Veau V. (1899) De la signification morphologique des aponévroses périvésicales. *Journal de l'anatomie et de la physiologie,* 35, 235-245.

Davis AA. (1934) The Surgical Anatomy of the Presacral Nerve. *BJOG: An International Journal of Obstetrics & Gynaecology,* 41, 942-954.

Dong M, Wang X, Chan AK, Burns AJ, Chan WY. (2006) Early Migration of Sacral Neural Crest Cells in Mouse Embryos. *Neuroembryology and Aging,* 4, 189-201.

Druckenbrod NR, Epstein ML. (2005) The pattern of neural crest advance in the cecum and colon. *Dev Biol,* 287, 125-33.

Durbec PL, Larisson-Blomberg LB, chuchardt A, Costatini F, Pachnis V. (1996) Common origin and developmental dependence on c-ret of subsets of enteric and sympathetic neuroblasts. *Development,* 122, 349-58.

Dyson L, Holmes A, Li A, Kulesa PM. (2018) A chemotactic model of trunk neural crest cell migration. *Genesis,* 56, e23239.

Erickson CS, Zaitoun I, Haberman KM, Gosain A, Druckenbrod NR, Epstein ML. (2012) Sacral neural crest-derived cells enter the aganglionic colon of Ednrb−/− mice along extrinsic nerve fibers. *Journal of Comparative Neurology,* 520, 620-632.

Espinosa-Medina I, Jevans B, Boismoreau F, Chettouh Z, Enomoto H, Müller T, Birchmeier C, Burns AJ, Brunet J. (2017) Dual origin of enteric neurons in vagal Schwann cell precursors and the sympathetic neural crest. *Proceedings of the National Academy of Sciences,* 114, 11980.

Espinosa-Medina I, Saha O, Boismoreau F, Chettouh Z, Rossi F, Richardson WD, Brunet JF. (2016) The sacral autonomic outflow is sympathetic. *Science,* 354, 893-897.

Esteban S, Rayo JM, Moreno M, Sastre M, Rial RV, Tur JA. (1991). A role played by the vitelline diverticulum in the yolk sac resorption in young post-hatched chickens. *Journal of Comparative Physiology B,* 160, 645-648.

Evans HM. (1912) Development of the vascular system. *In:* KEIBEL, F. & MALL, F. P. (eds.) *Manual of human embryology.* Philadelphia: JP Lippincott Co.

Fang J, Zheng Z, Wei H. (2019) Reconsideration of the Anterior Surgical Plane of Total Mesorectal Excision for Rectal Cancer. *Diseases of the Colon & Rectum,* 62, 639-641.

Fielding JR. (2002) Practical MR Imaging of Female Pelvic Floor Weakness. *RadioGraphics,* 22, 295-304.

Fritsch H. (1988) Developmental changes in the retrorectal region of the human fetus. *Anatomy and embryology,* 177, 513-522.

Furlan A, Dyachuk V, Kastriti ME, Calvo-Enrique L, Abdo H, et al. (2017) Multipotent peripheral glial cells generate neuroendocrine cells of the adrenal medulla. *Science,* 357.

Hamburger V, Hamilton HL. (1951) A series of normal stages in the development of the chick embryo. *J Morphol,* 88, 49-92.

Hatch J, Mukouyama Y. (2015) Spatiotemporal mapping of vascularization and innervation in the fetal murine intestine. *Developmental Dynamics,* 244, 56-68.

Hikspoors JP, Kruepunga N, Mommen GMC., Peeters J, et al. (2019) The development of the dorsal mesentery in human embryos and fetuses. *Seminars in Cell & Developmental Biology,* 92, 18-26.

Kapur RP. (2000) Colonization of the Murine Hindgut by Sacral Crest-Derived Neural Precursors: Experimental Support for an Evolutionarily Conserved Model. *Developmental Biology,* 227, 146-155.

Kapur RP, Yost C, Palmiter RD. (1992). A transgenic model for studying development of the enteric nervous system in normal and aganglionic mice. *Development,* 116, 167-175.

Kastriti ME, Kameneva P, Kamenev D, Dyachuk V, et al. (2019) Schwann Cell Precursors Generate the Majority of Chromaffin Cells in Zuckerkandl Organ and Some Sympathetic Neurons in Paraganglia. *Frontiers in Molecular Neuroscience,* 12.

Kimmel DL,.Moorea LE. (1958) The development of the pelvic plexuses and the distribution of the pelvic splanchnic nerves in the human embryo and fetus. *Journal of Comparative Neurology,* 110, 271-297.

Kinogasa Y, Nikura H, Murakami G, Suzuki D, Saito S, Tatsum H, Ishii M. (2008) Development of the human hypogastric nerve sheath with special reference to the topohistology between the nerve sheath and other prevertebral fascial structures. *Clinical anatomy,* 21, 558-67.

Kirby ML.(2007). *Cardiac development,* New York, Oxford University Press.

Koch WF, Marani E. (2007) Early development of the human pelvic diaphragm. *Adv Anat Embryol Cell Biol,* 192, 1-111.

Krishnan A, Samitani R, Dhanantwari, P, Lee E, Yamada S, et al. (2014) A detailed comparison of mouse and human cardiac development. *Pediatr Res,* 76, 500-7.

Kruepunga N, Hikspoors JPJM, Mekonen HK, Mommen GM, Meemon K, Weerachtyanulkul W, Asuvapongpatana S, Kohler SE, Lamers WH. (2018) The development of the cloaca in the human embryo. *Journal of Anatomy,* 233, 724-739.

Kuntz, A. (1952) Origin and early development of the pelvic neural plexuses. *The Journal of comparative neurology,* 96, 345-57.

Lake JI, Heuckeroth RO. (2013) Enteric nervous system development: migration, differentiation, and disease. *American Journal of Physiology - Gastrointestinal and Liver Physiology,* 305, G1-G24.

Lamers WH, Spliet WG, Langemeyer RA. (1987) The lining of the gut in the developing rat embryo. *Anatomy and Embryology,* 176, 259-265.

Le Douarin NM, Teillet M. (1973) The migration of neural crest cells to the wall of the digestive tract in avian embryo. *Journal of Embryology and Experimental Morphology,* 30, 31.

Mckeown SJ, Chow CW, Young HM. (2001) Development of the submucous plexus in the large intestine of the mouse. *Cell Tissue Res,* 303, 301-5.

Mekonen HK, Hikspoors JP, Mommen G, Kohler SE, Lamers WH. (2015) Development of the ventral body wall in the human embryo. *Journal of Anatomy,* 227, 673-685.

Nishiyama C, Uesaka T, Manabe T, Yonekura Y, Nagasawa T, Newgreen DF, Young HM, Eenomoto H. (2012) Trans-mesenteric neural crest cells are the principal source of the colonic enteric nervous system. *Nat Neurosci,* 15, 1211-1218.

O'Rahilly R, Muller F. (2010) Developmental stages in human embryos: revised and new measurements. *Cells Tissues Organs,* 192, 73-84.

O'Rahilly R, Müller F. (2007) The development of the neural crest in the human. *Journal of Anatomy,* 211, 335-351.

Olamoto E Ueda T. (1967) Embryogenesis of intramural ganglia of the gut and its relation to Hirschsprung's disease. *Journal of Pediatric Surgery,* 2, 437-443.

Pearson AA, Sauter RW. (1970) Nerve contributions to the pelvic plexus and the umbilical cord. *The American journal of anatomy,* 128, 485-98.

Pettan-Brewer C, Treuting PM. (2011) Practical pathology of aging mice. *Pathobiol Aging Age Relat Dis,* 1.

Pooh RK, Shiota K, Kurjak A. (2011) Imaging of the human embryo with magnetic resonance imaging microscopy and high-resolution transvaginal 3-dimensional sonography: human embryology in the 21st century. *American Journal of Obstetrics and Gynecology,* 204, 77.e1-77.e16.

Saito D, Takahashi Y. (2015) Sympatho-adrenal morphogenesis regulated by the dorsal aorta. *Mechanisms of Development,* 138, 2-7.

Serbedzija GN, Burgan S, Fraser SE, Bronner-Fraser M. (1991) Vital dye labelling demonstrates a sacral neural crest contribution to the enteric nervous system of chick and mouse embryos. *Development,* 111, 857-66.

Simkin JE, Zhang D, Rollo BN, Newgreen DF. (2013) Retinoic acid upregulates ret and induces chain migration and population expansion in vagal neural crest cells to colonise the embryonic gut. *PLoS One,* 8, e64077.

Simkin JE, Zhang D, Stamp LA, Newgreen DF. (2019) Fine scale differences within the vagal neural crest for enteric nervous system formation. *Developmental Biology,* 446, 22-33.

Soffers JH, Hikspoors JP, Mekonen HK, Koehler SE, Lamers WH. (2015) The growth pattern of the human intestine and its mesentery. *BMC Developmental Biology,* 15, 31.

Southwell BR. (2006) Staging of intestinal development in the chick embryo. *The Anatomical Record Part A: Discoveries in Molecular, Cellular, and Evolutionary Biology,* 288A, 909-920.

Tichy M. (1989) The morphogenesis of human sphincter urethrae muscle. *Anatomy and Embryology,* 180, 577-582.

Tobin CE, Benjamin JA. (1945) Anatomical and surgical restudy of Denonvilliers fascia. *Surgery Gynecology & Obstetrics,* 80, 373-388.

Uesaka T, Nagashimada M, Enomoto H. (2015) Neuronal differentiation in schwann cell lineage underlies postnatal neurogenesis in the enteric nervous system. *J Neurosci,* 35, 9879-88.

Uesaka T, Young HM, Pachnis V, Emomoto H. (2016) Development of the intrinsic and extrinsic innervation of the gut. *Developmental Biology,* 417, 158-167.

Uhlenhuth E, Wolfe WM, Smith EM, Middleyon EB. (1948) The rectogenital septum. *Obstetrical & Gynecological Survey,* 3, 148-163.

Van der Putte SCJ. (2004) *The development of the perineum in the human : a comprehensive histological study with a special reference to the role of the stromal components,* New York, Springer.

Wang X, Chan AK, Sham MH, Burns AJ, Chan WY. (2011) Analysis of the sacral neural crest cell contribution to the hindgut enteric nervous system in the mouse embryo. *Gastroenterology,* 141, 992-1002 e1-6.

Wiese CB, Deal KK, Ireland SJ, Cantrell VA, Southard-Smith EM. (2017) Migration pathways of sacral neural crest during development of lower urogenital tract innervation. *Developmental Biology,* 429, 356-369.

Young HM, Hearn CJ, Ciampoli D, Southwell BR, Brunet JF, Newgreen DF. (1998) A single rostrocaudal colonization of the rodent intestine by enteric neuron precursors is revealed by the expression of Phox2b, Ret, and p75 and by explants grown under the kidney capsule or in organ culture. *Dev Biol,* 202, 67-84.

Youn HM, Newgreen D. (2001) Enteric neural crest-derived cells: Origin, identification, migration, and differentiation. *The Anatomical Record,* 262, 1-15.

Note added in proof

While our studies (Kruepunga et al, 2020a and 2020b) were under review, an instructive and elegant study on the developmental appearance of the extrinsic afferent and efferent innervation of the murine gut was published (Niu et al, 2020). The authors used the expression of genes that characterize different neuron phenotypes to identify vagal and spinal visceral afferent, and parasympathetic vagal and sympathetic efferent nerve tracts and ganglia. Their main findings were that the vagal afferent nerves extended caudally around the esophagus at embryonic day (ED) 10.5, reached the stomach at ED11.5, and split into gastric and celiac branches in the upper abdomen to colonize the walls of the stomach and upper intestine at ED12.5. The preganglionic parasympathetic efferent nerves that originate in the dorsal motor nucleus of the vagus nerve followed the vagal afferent fibers with a short delay. Niu et al.'s timeline differed by ~1 day from that published earlier (Baetge and Gershon, 1989; Ratcliffe et al, 2006, 2011) which, given the variation in timing of murine conception (see "answer to reviewers" in Hikspoors et al, 2022) may not represent a real difference. At ED12.5, sensory neurons originating in the dorsal root ganglia and passing through the preaortic sympathetic plexuses extended towards the gut to form the trajectories of the spinal visceral afferent nerves. By ED14.5, these fibers have reached the gut wall and merge with the gastric and celiac branches of the afferent vagus nerve. Spinal sensory, sympathetic and parasympathetic nerves enter the hindgut via the pelvic (hypogastric) ganglion. By ED16.5, the extrinsic innervation had extended throughout the gut.

Niu's study differs from ours in that they could describe the expanding extrinsic innervation of the gut based on differences in gene expression in the nerve fibers, whereas we had to rely on the basal morphology of the cell bodies and fibers. We, therefore, had to limit ourselves to the description of the vagus nerve as it extended along the esophagus (CS14; ~34 days post fertilization), and stomach (CS16; ~38 days) to the upper small intestine (CS18; ~43 days) (Hikspoors et al, in preparation). The spatiotemporal pattern of the vagal expansion as we observed it therefore corresponds well with that described by Niu et al. (2020).

We have considered the preaortic plexuses and the fibers reaching and emanating from them as (largely) sympathetic. Whereas Niu et al. describe only the "prevertebral" and "pelvic" ganglia, we describe the sympathetic trunks and their pre- and postganglionic nerves in detail. Furthermore, we describe the celiac and inferior mesenteric plexuses as the main preaortic plexuses in the abdomen, and the inferior

hypogastric (pelvic) plexus as the corresponding plexus in the lesser pelvis. The superior hypogastric plexus is initially represented by the "superior hypogastric nerve" that covers the superior rectal artery dorsally. This hypogastric nerve is clearly visible in Niu et al.'s Figures, but is not identified as such. Furthermore, their Figures show that the nerve fiber network in the outer wall of the hindgut clearly differs from that elsewhere in the gut, but this feature is also not acknowledged. The findings show that the emphasis in both studies is unexpectedly complementary.

Studying mice has a crucial advantage over studying humans in that well-designed experimental interventions do not raise ethical problems. The experiment that Niu et al carried out involved the cell-type-specific expression of the diphteria toxin gene to ablate vagal afferent or sympathetic efferent tracts. These elegant experiments showed that the vagal visceral afferent tracts serve as a scaffold to guide the preganglionic vagal efferent neurons to their target. Earlier, Coppola et al (2010) showed that the visceral afferents of the head provide such a scaffold for parasympathetic efferent axons.

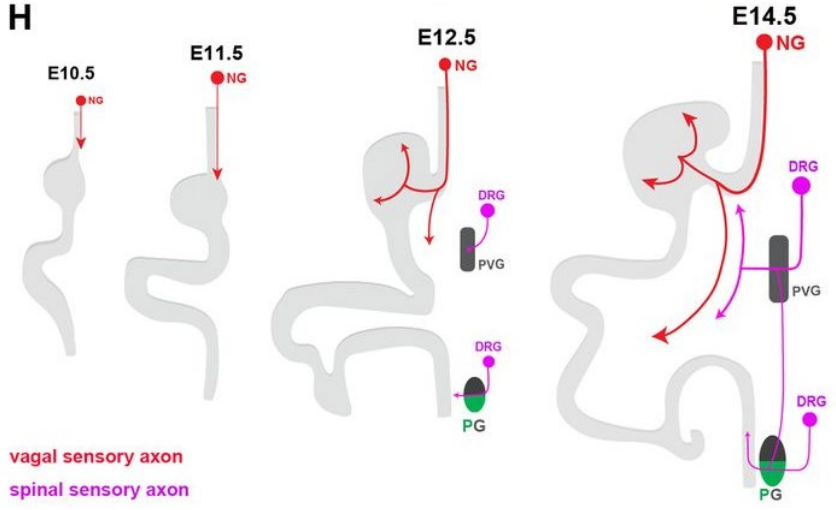

Figure 3H (Niu et al, 2020): Schematic summary of the development of extrinsic afferent innervation to the gut.

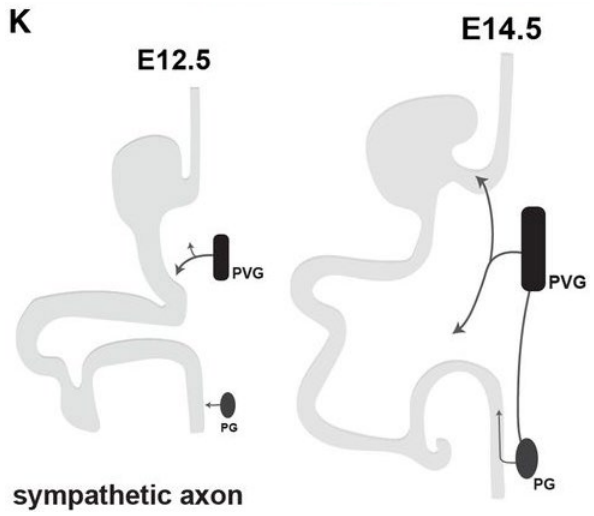

Figure 4K (Niu et al, 2020): Schematic summary of the development of gut-innervating sympathetic axons.

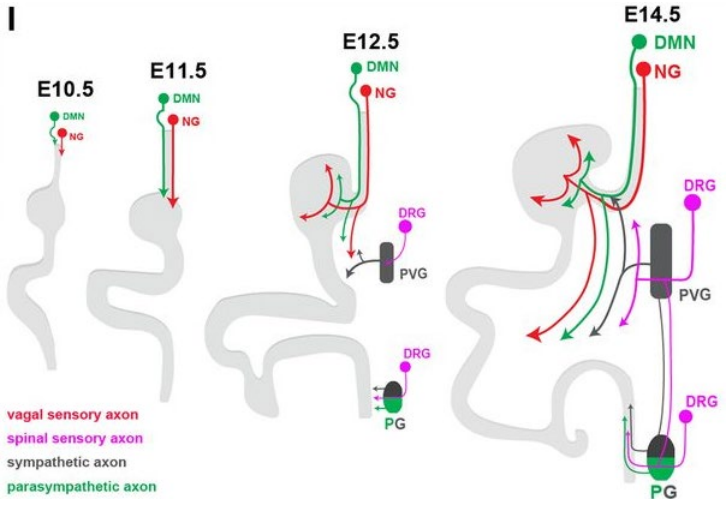

Figure 6I (Niu et al, 2020): Schematic summary of the extrinsic innervation of the gut from E10.5 to E14.5.

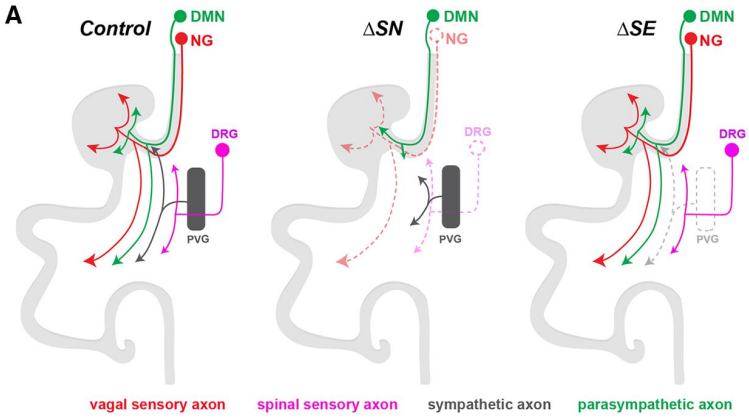

Figure 11 **(Niu et al, 2020): Hierarchical relationships among three types of extrinsic gut-innervating axons.**

References

Niu X, Liu L, Wang T, Chuan X, Yu Q, Du M, Gu Y, Wang L (2020) Mapping of extrinsic innervation of the gastrointestinal tract in the mouse embryo. Journal of Neuroscience 40(35), 6691-6708

Baetge G, Gershon MD. (1989) Transient catecholaminergic (TC) cells in the vagus nerves and bowel of fetal mice: relationship to the development of enteric neurons. Dev Biol 132:189–211.

Ratcliffe EM, Setru SU, Chen JJ, Li ZS, D'Autreaux F, Gershon MD. (2006) Netrin/DCC-mediated attraction of vagal sensory axons to the fetal mouse gut. J Comp Neurol 498:567–580.

Ratcliffe EM, Fan L, Mohammed TJ, Anderson M, Chalazonitis A, Gershon MD. (2011) Enteric neurons synthesize netrins and are essential for the development of the vagal sensory innervation of the fetal gut. Dev Neurobiol 71:362–373.

Coppola E, Rallu M, Richard J, Dufour S, Riethmacher D, Guillemot F, Goridis C, Brunet JF. (2010) Epibranchial ganglia orchestrate the development of the cranial neurogenic crest. Proc Natl Acad Sci USA 107:2066–2071.

Chapter 5
Development of the sympathetic trunk in human embryos

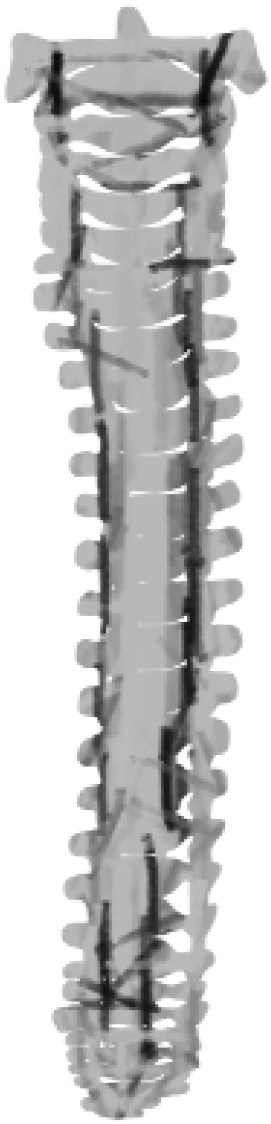

Nutmethee Kruepunga, Jill P.J.M. Hikspoors, Cindy J.M. Hülsman,
Greet M.C. Mommen, S. Eleonore Köhler and Wouter H. Lamers
Journal of Anatomy (2021); 239(1): 32-45

Abstract

Although the development of the sympathetic trunks was first described >100 years ago, the topographic aspect of their development has received relatively little attention. We visualised the sympathetic trunks in human embryos of 4.5-10 weeks post-fertilisation, using Amira 3D-reconstruction and Cinema 4D-remodelling software. Scattered, intensely staining neural crest-derived ganglionic cells that soon formed longitudinal columns were first seen laterally to the dorsal aorta in the cervical and upper thoracic regions of Carnegie stage (CS)14 embryos. Nerve fibres extending from the communicating branches with the spinal cord reached the trunks at CS15-16 and became incorporated randomly between ganglionic cells. After CS18, ganglionic cells became organised as irregular agglomerates (ganglia) on a craniocaudally continuous cord of nerve fibres, with dorsally more ganglionic cells and ventrally more fibres. Accordingly, the trunks assumed a “pearls-on-a-string” appearance, but size and distribution of the pearls were markedly heterogeneous. The change in position of the sympathetic trunks from lateral (para-aortic) to dorsolateral (prevertebral or paravertebral) is a criterion to distinguish the “primary” and “secondary” sympathetic trunks. We investigated the position of the trunks at vertebral levels T2, T7, L1 and S1. During CS14, the trunks occupied a para-aortic position, which changed into a prevertebral position in the cervical and upper thoracic regions during CS15, and in the lower thoracic and lumbar regions during CS18 and CS20, respectively. The thoracic sympathetic trunks continued to move further dorsally and attained a paravertebral position at CS23. The sacral trunks retained their para-aortic and prevertebral position, and converged into a single column in front of the coccyx. Based on our present and earlier morphometric measurements and literature data, we argue that differential growth accounts for the regional differences in position of the sympathetic trunks.

Introduction

The peripheral autonomic nervous system derives mostly from neural crest cells (NCCs) that arise concomitantly with neurulation in a cranio-caudal gradient at the junction of the neural tube and skin (Theveneau and Mayor, 2012, Pla and Monsoro-Burq, 2018). In human embryos NCCs appear in a cranio-caudal sequence between CS10 and CS15 [29-36 days of development (O'Rahilly and Müller, 2007, Kruepunga et al., 2020a)]. After delamination, these NCCs migrate ventrally to form, among others, dorsal root ganglia, sympathetic ganglia and pre-aortic nerve plexuses (Theveneau and Mayor, 2012, Vega-Lopez et al., 2017). The sympathetic trunks consist of a bilateral chain of ganglia and nerve fibres. Several studies have suggested that the sympathetic trunks and adrenal medulla share a common progenitor and constitute the sympathoadrenal lineage. The migratory route of the NCCs of the sympathoadrenal lineage, and the successive appearance of ganglionic cells and interganglionic nerve fibres of the sympathetic trunks, has been described in mammals, including humans, already a century ago (His, 1890, Kuntz, 1910, Streeter, 1912, Kuntz, 1920). However, the regulation of its putatively metameric configuration was established only relatively recently (Groen et al., 1987, Goldstein and Kalcheim, 1991a, Kasemeier-Kulesa et al., 2005). The complex peripheral deployment of neural crest cells to the sympathetic system is often not considered beyond the separation of the sympathoadrendal lineage into sympathetic trunks and adrenal medulla. As a consequence, many schematics illustrating this aspect are reduced to a transverse section of the embryo only (Huber, 2006, Lumb and Schwarz, 2015, Furlan et al., 2017).

An only partially understood topographical aspect of the developing sympathetic trunks is their position relative to the dorsal aortae. The sympathetic trunks form lateral to the aorta. In this para-aortic position, they are known as the “primary” sympathetic trunks. This position changes gradually to one between the aorta and vertebral column (prevertebral), or one lateral to the vertebral bodies (paravertebral). In the paravertebral position the trunks are referred to as “secondary” sympathetic trunks (Kuntz, 1920, Gibbins, 1994). The ganglionic cells of the primary trunks are still mitotically active (Rothman et al., 1978), but have already acquired an aminergic phenotype before their topographical position begins to change to the more dorsolateral prevertebral position (Cochard et al., 1979). The significance of this change in position is still poorly understood. One hypothesis states that the primary sympathetic trunks represent the phylogenetically older structure, from which neurons migrate dorsally to form the secondary sympathetic trunks (Gibbins, 1994). A more

recent report showed that shortly after arrival of the primary sympathetic trunks at the lateral side of the aorta, brain-derived neurotrophic factor (BDNF) secreted by approaching preganglionic nerve fibres in the spinal nerves induces the primary sympathetic ganglia to re-migrate dorsally (Kasemeier-Kulesa et al., 2015). Both accounts emphasize the importance of the different topography of the primary and secondary sympathetic trunks, but have not addressed the question whether the change in position is mediated by a functional change in the neurons of the trunks (e.g. their synthesis of the BDNF receptor TrkB) or the result of differential changes in growth of surrounding structures.

In our studies of the extrinsic innervation in the abdomen and lesser pelvis (Kruepunga et al., 2020a, Kruepunga et al., 2020b), we identified neural crest-derived ganglionic cells by their intense staining properties and topography (cf. also (Lutz, 1968)). In these studies, we did not address the appearance and organisation of neural crest-derived cells that form the sympathetic trunks. In particular, we did not assess the putatively metameric organisation of the sympathetic trunks along their longitudinal axis, the polarity of their organisation along the radial axis, and their topographical relation to surrounding tissues. We addressed these questions by producing detailed reconstructions of the sympathetic trunks and their surroundings in 9 embryos between 5 and 10 weeks of development. In addition, we quantified the distances between sympathetic trunks and surrounding landmarks to establish the time course and extent of the changes in topographic position of the developing sympathetic trunks.

Materials and methods

Embryos

This study was undertaken in accordance with the Dutch regulations for the proper use of human tissue for medical research purposes. Well-preserved anonymous human embryos and foetuses, donated for scientific research, of the historical collections of the Departments of Anatomy and Embryology, Leiden University Medical Centre (LUMC), the Amsterdam University Medical Centres, location Academic Medical Centre (AMC), Radboud University, Nijmegen, The Netherlands, and the University of Göttingen, Germany (Blechschmidt Collection; https://doi.org/10.3249/ugoe-publ-2) were studied (Table 5.1). In addition, digital images of carefully staged human embryos from the

Carnegie collection (Washington D.C., USA) were included from the Digitally Reproduced Embryonic Morphology (DREM) project (http://virtualhumanembryo.lsuhsc.edu).

Table 5.1 **Metadata of human embryos and foetuses used in the study.** The estimated post-fertilisation ages of the embryos are based on (O'Rahilly and Müller, 2010). The additions "early", "mid" and "late" are meant to indicate that, within these stages, the development of the gut and enteric nervous system of "late" embryos was more advanced than that of "early" embryos. The corresponding age was chosen from the range of developmental days attributed to that stage (O'Rahilly and Müller, 2010). CS14 is in particular noted for its remarkable number of developmental events. Abbreviations: AC, alum cochineal (i.e., carmine); AMC, Academic Medical Centre; CS, Carnegie stage; DREM, Carnegie collection from the Digitally Reproduced Embryonic Morphology project; Göttingen, Department of Anatomy and Embryology, Göttingen; H&A, haematoxylin and azophloxine; H&E haematoxylin and eosin; LUMC, Leiden University Medical Centre; PAS, periodic acid–Schiff stain; RadboudMC: Radboud Medical Centre.

Stage	Days	Embryo	Fixation	Staining	Plane	Source
CS13	32	S836	HgCl2	CA	Transv	DREM
CS14-early	33	S2201	Formalin	H & A	Transv	AMC
CS14-mid	34	S5029	Formalin	H & A	Sagittal	AMC
CS14-mid	34	S168	Bouin's fix	H & E	Transv	LUMC
CS14-mid	34	1950-09-13	Bouin's fix	H & E	Sagittal	Göttingen
CS14-late	35	1958-12-22	Bouin's fix	H & E	Sagittal	Göttingen
CS14-late	35	1961-06-13	Bouin's fix	H & E	Transv	Göttingen
CS14-late	35	S6502	Souza's fix	H & E (or + Ag)	Transv	DREM
CS15-early	36	S721	Zenker's fix	H & E (or + Ag)	Transv	DREM
CS15-early	36	S79	Formalin	H & E	Transv	LUMC
CS15-early	36	1945-10-26	Bouin's fix	H & E	Transv	Göttingen
CS15-early	36	1957-10-31	Bouin's fix	H & E	Transv	Göttingen
CS15-late	37	S2213	Formalin	H & A	Transv	AMC
CS16	39	S5032	Formalin	H & A	Sagittal	AMC
CS16	39	S6517	Corrosive CH3COOH	CA	Transv	DREM
CS16	39	S39	Formalin	H & E	Transv	LUMC
CS17	41	S6520	Corrosive CH3COOH	CA (or + Ag)	Transv	DREM
CS18	44	S97	Bouin's fix	H & E	Transv	LUMC
CS18	44	S4430	Corrosive CH3COOH	CA	Transv	DREM
CS19	46	S9325	Acetic formalin	Azan & Ag	Transv	DREM
CS20	49	S2025	Bouin's fix	H & A	Transv	AMC
CS20	49	S462	Formalin	CA	Transv	DREM
CS20	49	S34	Formalin & Bouin's fix	H & E	Sagittal	LUMC
CS21	51	S4090	Formalin	CA	Transv	DREM
CS22	53	S48	Formalin	H & E	Transv	LUMC
CS22	54	S983	Formalin	H & E	Transv	DREM
CS23	56	S4141	Formalin	H & A	Transv	AMC
CS23	56	S9226	Formalin	Azan	Transv	DREM
CS23	56	S88	Formalin & Bouin's fix	H or PAS or Azan	Sagittal	RadboudMC
9 weeks	63	S89	Formalin	H & E or Azan	Transv	LUMC
9.5 weeks	67	S57	Formalin	H & E	Transv	LUMC
10 weeks	70	S1507		H & A	Transv	AMC

Image acquisition, 3D reconstruction, and visualization

Human embryos between 4.5-10 weeks post-fertilisation were investigated. The modified O'Rahilly criteria were used to define the Carnegie stage (CS) of development and post-fertilisation age [(O'Rahilly and Müller, 2010); Table 5.1]. Serial sections from the aforementioned collections were digitised with an Olympus BX51 or BX61 microscope and the Dotslide program (Olympus, Leiderdorp, The Netherlands) to provide high-resolution digital images. Serial sections of the Blechschmidt collection were digitized with a Zeiss Axio Scan.Z1 (Carl Zeiss Microscopy, Jena, Germany). All digital images were transformed into greyscale 'JPEG' format and imported into Amira (version 2019.4; FEI Visualization Sciences Group Europe, Merignac Cedex, France). The imported images were aligned automatically with the least-squares function and then manually corrected for their embryonic curvature with the aid of photographs and magnetic resonance images (MRI) of the same stages of human embryos (Pooh et al., 2011). The criteria used to identify agglomerates of scattered neural crest cells were cell staining properties (intensely basophilic), cell density, and cell distribution. Developing nerve fibres were characterized by their intensely acidophilic staining property and filamentous distribution. These criteria allowed for sensitive and accurate segmentation throughout early development (Supplemental Figure S5.1). In later stages, the borders of the neural agglomerates and their connecting nerve fibres became more distinct. Based on these criteria structures of interest were identified and segmented manually to generate three-dimensional images with the Amira program. To exclude the distracting noise from section processing and stacking in the Amira output, Amira polygon meshes were exported via 'vrml export' to Cinema 4D (version R21; MAXON Computer GmbH, Friedrichsdorf, Germany) and remodelled using the Amira model as a template. Synchronous visualization of the Amira template and the remodelled Cinema4D model in Cinema 4D was used to validate the accuracy of the Cinema4D models (Supplemental Figure S5.2). The Cinema4D models were transferred via 'wrl export' to Adobe Acrobat version 9 (http://www.adobe.com) to generate interactive 3D Portable Device Format (PDF) files, which are a user-friendly format for 3D visualization (Supplemental Figures S5.3 and S5.4). We mostly refer in the text to the Figures to relate histology to developing structures, but encourage the reader to simultaneously inspect the interactive PDFs, because their rotational options ("live" images) allow a much better understanding of the complex local topography than the "still" pictures in the images.

Measurements

All morphometric analyses were performed in Amira. The data were subsequently analysed in Microsoft Excel (Microsoft Corporation, Washington, USA). Analyses included topographic position of sympathetic ganglionic cells and nerve fibres, and distances between 4 landmarks. These landmarks were the middle of the floor plate of the spinal cord, the notochord, the centres of the sympathetic ganglia, and the middle of the dorsal side of the aorta. The segmental positions were determined perpendicular to the embryonic axis (notochord). The first cervical level was defined as the first segment in this study.

Results

Formation of the sympathetic trunks

The sympathetic trunks form from scattered, intensely staining neural crest cell-derived ganglionic cells (Kuntz, 1920, Furlan and Adameyko, 2018). No cells with these characteristics are found near the dorsal aortae of a well-preserved CS13 embryo. Such cells do, however, appear laterally to the dorsal aorta in the lower cervical and upper thoracic levels at CS14-early (~33 days of development). In the next few days (CS14-late; ~35 days), the number of ganglionic cells increases greatly (Figure 5.1A). In the lower cervical and upper thoracic region these scattered ganglionic cells form longitudinal columns between the entrance of a spinal nerve into the dermomyotome laterally and the aorta medially (Figure 5.2A, F), while others are found more ventrally to the pre-aortic region (not shown, but described at length in our earlier studies (Kruepunga et al., 2020a, Kruepunga et al., 2020b). The sympathetic trunk at CS14 consists of ganglionic cells only (blue dots in Figure 5.1A and blue arrows in Figure 5.2F), although nerve fibres from spinal nerves are already extending medially towards the forming columns of ganglionic cells to form the so-called “communicating branches” (cf. Figure 5.2 in (Kruepunga et al., 2020a)). These nerve fibres reach and become incorporated in the sympathetic trunk between CS15-late and CS16 (37-39 days). The sympathetic trunks at this stage are, therefore, composed of randomly distributed ganglionic cells intermingled between nerve fibres (blue dots and orange cords in Figure 5.1B; blue and orange arrows, respectively, in Figure 5.2G). From CS18 onwards (44 days) ganglionic cells manifest themselves as irregular agglomerates (ganglia) along a continuous cord of nerve fibres.

Simultaneously with the patterning of sympathetic trunks along the craniocaudal axis, ganglionic cells and nerve fibres separate along the dorsoventral axis. Compared to the random distribution of ganglionic cells and nerve fibres in the forming trunks of CS15-16 embryos (Figures 5.1B and 5.2G), the ganglionic cells have aggregated on the dorsal side of the sympathetic trunks, whereas the nerve fibres concentrate more ventrally from CS18 onward (blue dots and orange cords in Figures 5.1C-F; blue and orange arrows, respectively in Figure 5.2H-J). This configuration is often described as ganglionic cells becoming organised in a pearl-necklace-like fashion along the nerve fibres, but it should be noted that both size and distribution of the pearls are markedly heterogeneous (Figures 5.1 and 5.2).

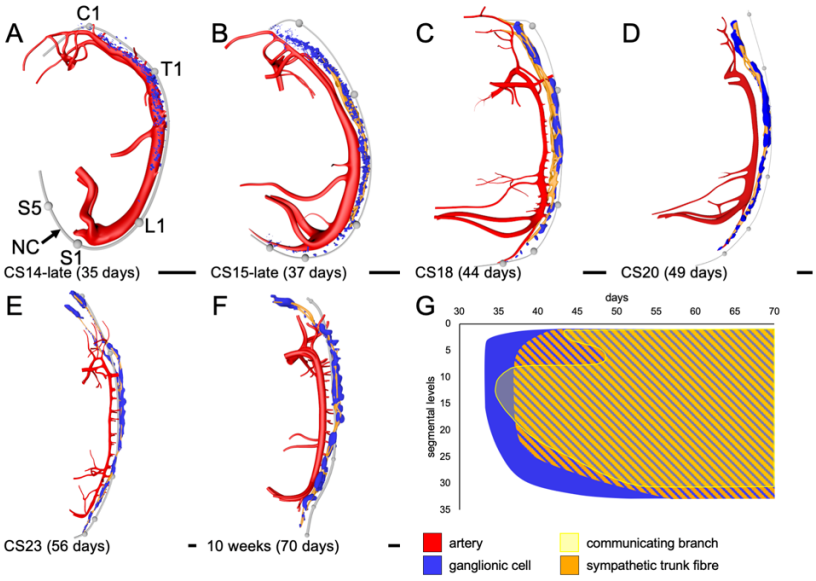

Figure 5.1 **Spatiotemporal distribution of the ganglionic cells and the nerve fibres of the sympathetic trunks.** Panels A-F (left-sided views) show left-sided views of the topographic distribution of the sympathetic trunks along the aorta and notochord (NC; grey). The spheres on the notochord represent the first cervical (C1), first thoracic (T1), first lumbar (L1), first sacral (S1), and fifth sacral (S5) segmental levels. Segmental levels are determined by counting the spinal ganglia. Spinal ganglia are not shown in the images, but are included in the reconstructions. Panel G shows the spatiotemporal distribution of ganglionic cells (blue), sympathetic trunk fibres (orange), and communicating branches (transparent yellow). At CS14-late (~35 days; panel A) dispersed ganglionic cells (blue) are present between C3 and T8. Subsequently (CS15-late, ~37 days; panel B), ganglionic cells extend cranially to reach C1 and caudally to reach S1 levels. Concomitantly, nerve fibres (yellow) have formed between C4 and L1. One week later (CS18, ~44 days; panel C), ganglionic cells have extended caudally to S5, whereas nerve fibres reach S5 (panel E) only 2 weeks later. These data are summarized in panel G. Bar = 500 µm. Note that the sympathetic trunks of the coccygeal region are not shown in panels E and F, because the pertinent sections were not available.

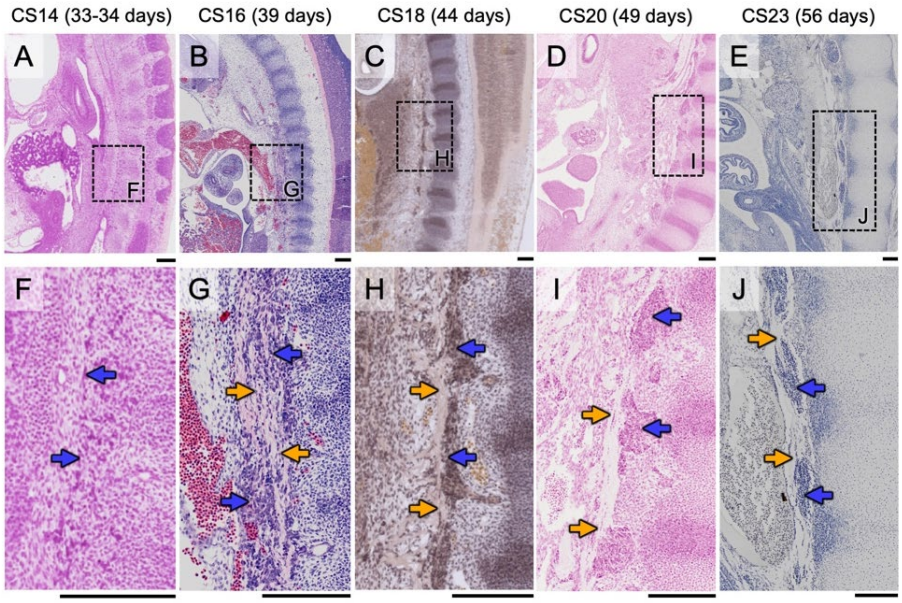

Figure 5.2 **Organisation of the ganglionic cells and the nerve fibres in the sympathetic trunks.** Panels A-E are overviews of sagittal sections that show the locations of the magnified areas (rectangles) in panels F-J. The magnifications show the distribution of ganglionic cells (blue arrows) and nerve fibres (yellow arrows) forming the sympathetic trunk. At CS14 (33-34 days; panel F) the sympathetic trunks consist of diffuse ganglionic cells only (blue arrows). Two stages later (CS16; ~39 days; panel G) nerve fibres (yellow arrows) become identifiable. At this stage, ganglionic cells and nerve fibres are distributed randomly within the sympathetic trunks (panel G). At CS18 (~44 days; panel H), the sympathetic trunks begin to assume a pearls-on-a-string appearance, while this configuration is clearly established at CS20 (~49 days). The pearls are represented by the segmental aggregations of ganglionic cells into ganglia that mainly locate to the dorsal side of the sympathetic trunks, whereas the strings are nerve fibres that are exclusively found on the ventral side of the trunks. Note that the ganglia match with the vertebrae in the cranial portion of panel D, but with the intervertebral disk caudally. The sympathetic trunks retain the pearls-on-a-string appearance at CS23 (~56 days; panel J), but ganglia now occupy a more central position in the trunks. Bars = 200 µm.

Spatiotemporal appearance of the components of the sympathetic trunks

Sympathetic trunks consisting of ganglionic cells become identifiable at CS14-early (~33 days). At CS14-late (~35 days), these ganglionic cells are found between cervical somite 3 and thoracic somite 8 (C3-T8), that is, across ~15 segments. Two days later (CS15-late) ganglionic cells have reached C1 cranially. Caudally, the ganglionic cells reach L2 at CS15-early (~36 days), S1 at CS15-late (~37 days), S5 at CS16 (~39 days) and the coccygeal region at CS22 (~53 days; Figure 5.1). The rate of caudal extension of the

sympathetic cells, therefore, gradually declines from ~6 segments per day at the end of CS14, via 4 segments per day during CS15, to 2 segments during CS16, and much slower in the caudal-most part (blue surface in Figure 5.1G). Nerve fibres are first seen in the sympathetic trunk at CS15-late (37 days) between C4 and L1 (Figure 5.1B; vertical leg of hatched orange surface in Figure 5.1G), which is ~2 days after the ganglionic cells have made their appearance. The nerve fibres have arrived at C1 at CS17 (41 days), so extend ~1 segment per day. The ganglionic cells, therefore, reach the cranial end of the vertebral column ~4 days ahead of the nerve fibres (Figure 5.3). Accordingly, they are found migrating along the future internal carotid arteries before nerve fibres are present (Figure 5.3B). Caudally, the ganglionic cells reach L5 at CS18 (44 days), S3 at CS20 (49 days) and the coccygeal region around CS22-CS23 (53-56 days; Figure 5.4), which represents a linear extension of ~0.6 segment per day (oblique lower leg of hatched orange surface in Figure 5.1G). The nerve fibres of the sympathetic trunk extend, therefore, much slower along the body axis than the ganglionic cells, but at a constant pace.

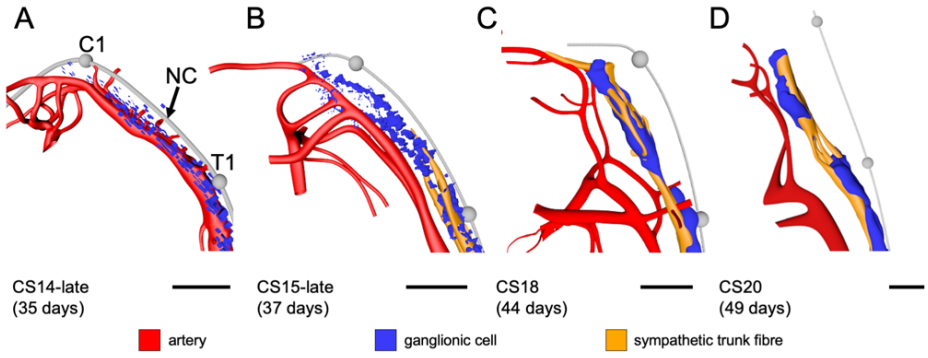

Figure 5.3 **Cranial expansion of the sympathetic trunks.** Panels A-D show left-sided views of the cranial end of the sympathetic trunks between 5 and 7 weeks of development. At 5 weeks the main group of ganglionic cells (blue) have reached C3 cranially, although a few ganglionic cells have already passed C1. Ganglionic cells accumulate cranially in the next 3 days (panel B). In contrast nerve fibres (yellow) emerge later and extend more slowly in cranial direction than the ganglionic cells. They arrive at C4 at 37 days and need another week to reach C1 (panel C). Meanwhile, ganglionic cells have arrived at the base of the skull. Note that nerve fibres in panel D were reconstructed only up to level C1. Bar = 500 µm.

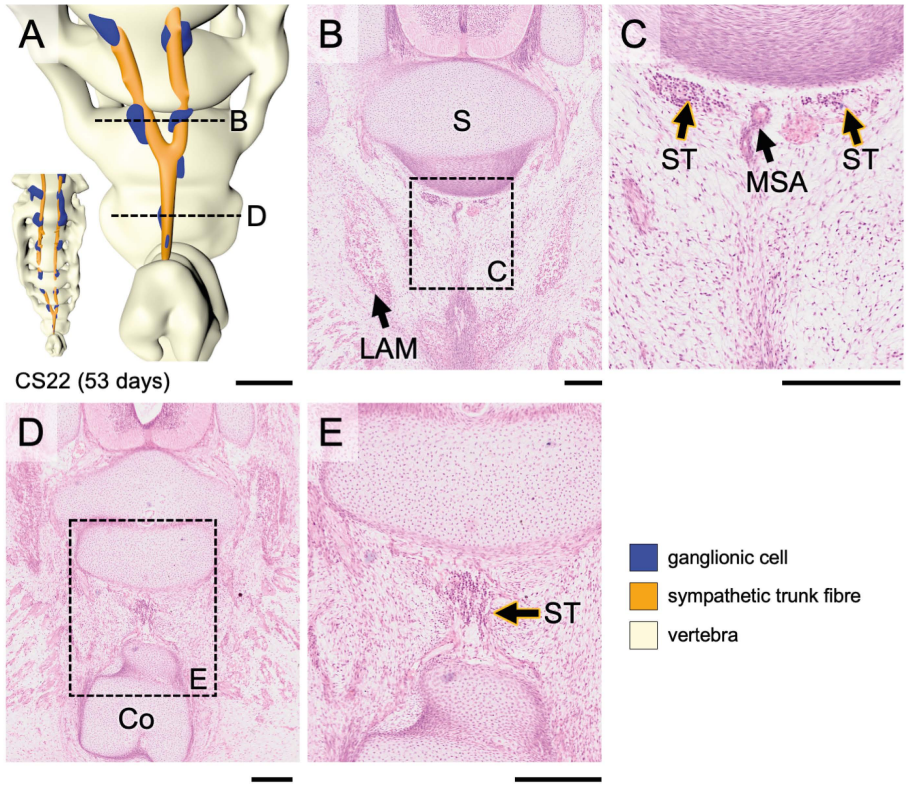

Figure 5.4 **Caudal portion of the sympathetic trunks.** Panel A shows a ventral view of the caudal part of the sympathetic trunks with sacrum and coccyx at CS22. Panels B and D show transverse histological sections of the sympathetic trunks at the levels indicated by dashed lines in panel A, whereas magnifications of the boxed areas in panels B and D are shown in panels C and E. At CS22 the sympathetic trunks (ST) in the sacral region (panel C) consist of two columns of ganglionic cells and nerve fibres lateral to the median sacral artery (MSA). Caudally, both sympathetic trunks (ST in panel E) converge into a single trunk with ganglia (panel A) in front of the coccygeal vertebrae (Co). The medial sacral artery is not present at this level. Bar A = 500 µm and bars B – E = 200 µm.

Regional differences in the configuration of the sympathetic trunks

As the ganglionic cells and the nerve fibres become organised in a pearl-necklace-like fashion between CS15-late and CS18 (37-44 days), the ganglia remain markedly heterogeneous both with respect to size and distribution (Figures 5.1 and 5.3). The most cranial, or superior cervical ganglion (SCG) of the sympathetic trunk forms, for example, far away from, and is larger than the adjacent inferior cervical (stellate) ganglion at the thoracic inlet. Both ganglia are further apart than more caudal ganglia

(Figures 5.1 and 5.3; (Rubin, 1985)). It should be noted, however, that a separate middle cervical ganglion was not observed. The distance between the superior and inferior cervical ganglia increases with development, in particular after CS18 (Figures 5.1 and 5.3), which correlates temporally with the formation of the neck. At CS22 (~53 days) the sympathetic trunks in the lumbar and sacral region consists of the standard two columns of ganglionic cells and nerve fibres lateral to the median sacral artery and ventral to the vertebral column (Figure 5.4A-C), but both trunks converge into a single column of ganglionic cells and nerve fibres in front of the coccygeal vertebrae. Usually, a single unpaired precoccygeal ganglion is described as the ganglion impar (Paterson, 1890), but we observed 2 small unpaired ganglionic agglomerates (Figure 5.4A,D,E). The medial sacral artery is not present at this level.

Nervous connections of the sympathetic trunks

Each sympathetic trunk forms one cranial and two main segmental nervous connections. The cranial part of the sympathetic trunk contacts the vagus nerve at CS15-late. We observed ganglionic cells (blue arrows in Figure 5.5B) along the internal carotid artery (ICA) between the sympathetic trunk (ST; black arrow) and the nodose ganglion (white-lined, olive-coloured dotted contour) of the vagus nerve (orange dotted contour; Figure 5.5B,C). Like the communicating branches, we do not know the direction of nerve signalling. We did not follow the migratory route of ganglionic cells along the ICA in the older embryos. Earlier studies have shown that ganglionic cells that migrate in the wall of the ICA populate the cranial ganglia (Streeter, 1912, Andres and Kautzky, 1955).

The first connection consists of segmentally organised nerve connections between the spinal nerves and sympathetic trunks, which are known as the communicating branches (golden arrowheads in Figure 5E,F; (Kruepunga et al., 2020a)). The first communicating branches are tiny nerve fibres between vertebral levels T3-T4 at CS14-late [35 days; Figure 5.2 in (Kruepunga et al., 2020a)]. Between CS15 and CS18 (37-44 days) communicating branches are present between C8 and L2 (Figure 5.1G). Interestingly, communicating branches, which join the developing superior cervical ganglion, are also present at segments C1 and C2, but not between C3 and C7 until CS18-late and older embryos. At CS20 (~49 days), such communicating branches are present from level C1 cranially to S1 caudally. Segmental level S4 is reached at CS22 (53 days) (transparent yellow area in Figure 5.1G, Supplemental Figures S5.3 and S5.4). Communicating branches, therefore, reach the sympathetic trunks at the same time as,

or shortly after nerve fibres appear in the trunks themselves. The staining of the embryos does not allow differentiation between white and grey communicating branches.

Splanchnic nerves pass through, but do not synapse in the ganglia of the sympathetic trunk. In Figure 5.5 (beige arrows in panels E and F) they can be seen between the sympathetic trunk and the pre-aortic coeliac plexus. The splanchnic nerves start to extend ventrally as scattered ganglionic cells at CS15-late (37 days), but have reached the pre-aortic ganglia at this stage only at the level of the coeliac trunk. We have described the spatiotemporal development of the splanchnic nerves in our studies on the autonomic innervation of the abdominal and pelvic intestines (Kruepunga et al., 2020a, Kruepunga et al., 2020b).

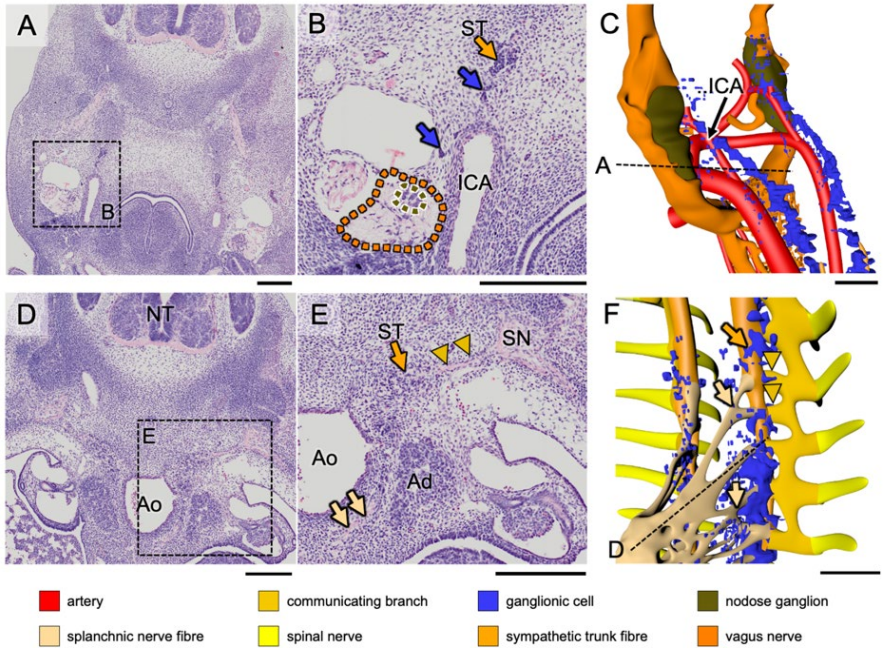

Figure 5.5 **Nervous connections of the sympathetic trunks.** Panels A, B, D and E show transverse histological sections of the sympathetic trunks and their connections at the level of the nodose ganglion of the vagus (A-C) and at the level of the celiac plexus (D-F), with the plane of the sections indicated by the dashed lines in panels C and F. In the upper row, ganglionic cells (blue arrows in panel B) migrate along the internal carotid artery (ICA) towards the nodose ganglion (olive colour code in panels B and C, with white lining in panel B) that is itself embedded in vagus nerve fibres (darker orange colour code in panels B,C. with black lining in panel B). In the lower row, a column of the sympathetic trunk (ST, black) appears to function as a hub: spinal nerves (SN) extend medially towards the sympathetic trunk as communicating branches (yellow arrowheads in panels E,F) or pass the sympathetic trunk and continue ventrally as a splanchnic nerve (beige arrows in panels E,F). Bars = 200 µm.

Change in topography of the sympathetic trunks

It is well established that the sympathetic trunks change their topographical position relative to the vertebral column with ongoing development (Kuntz, 1920, Gibbins, 1994, Kasemeier-Kulesa et al., 2015). The cited studies use the change in position of the trunks from lateral ("para-aortic") to dorsolateral (prevertebral or paravertebral) relative to the aorta as a criterion to mark the transition from primary to secondary sympathetic trunks. At CS14-late (35 days), the scattered ganglionic cells are considered to occupy a para-aortic position (Figure 5.6A). At CS15-late (37 days), the sympathetic trunks in the cervical and upper thoracic region have acquired a prevertebral position between the aorta ventrally and the vertebral column dorsally. The developing trunks in the lumbar and sacral region still occupy a para-aortic position. The lower thoracic and lumbar sympathetic trunks acquire a prevertebral position at CS18 (Figure 5.6C). Between CS18 and CS23 (44-56 days), only the position of the thoracic sympathetic trunk continues to move further dorsally to a paravertebral position (Figure 5.6C-E). The columns of the sympathetic trunk in the sacral region remain positioned lateral to the median sacral artery (morphologically the caudal continuation of the dorsal aorta) and in front of the sacrum between CS23 and 10 weeks. Their position is, therefore, considered as both para-aortic and prevertebral (Supplemental Figure S5.5).

To quantify the change in the position of the sympathetic trunks relative to the vertebral bodies, we measured 4 distances between landmarks surrounding the sympathetic trunks, including the middle of the floor plate of the spinal cord, the notochord (the vertebral column becomes identifiable only at CS15-late), the centres of the sympathetic trunks, and the middle of the dorsal aortic wall. All distances were measured at 4 vertebral levels: T2, T7, L1, and S1 (Figure 5.7A). The distances between the floor plate of the spinal cord and the notochord (line AB, Figure 5.7B) increase at a similar rate at all measured vertebral levels. The distance increases between CS16 and CS18, plateaus temporarily between CS18 and CS23, to increase again thereafter. The line connecting the notochord and the dorsoventral position of the centres of the sympathetic trunks (line BE, Figure 7C) hardly changes until CS21, after which the thoracic lines decline abruptly, in agreement with the change in position of the sympathetic trunks to paravertebral. At the lumbar and sacral levels, however, this distance hardly changes until CS23, after which it increases between weeks 9 and 10. The data in panels B and C indicate overall vertebral growth at the lumbar and sacral levels without change in position of the trunks. The distance between the left and right

columns of the sympathetic trunk (line CC, Figure 5.7D) and that between the sympathetic trunks and the dorsal aortic wall (line CD, Figure 5.7E) change with a similar pattern: steady growth between CS15 and 9 weeks, which is most pronounced in the upper thoracic region and slowest in the sacral region, with T7 and L1 again taking intermediate positions. At all vertebral levels, growth accelerates in the 10th week.

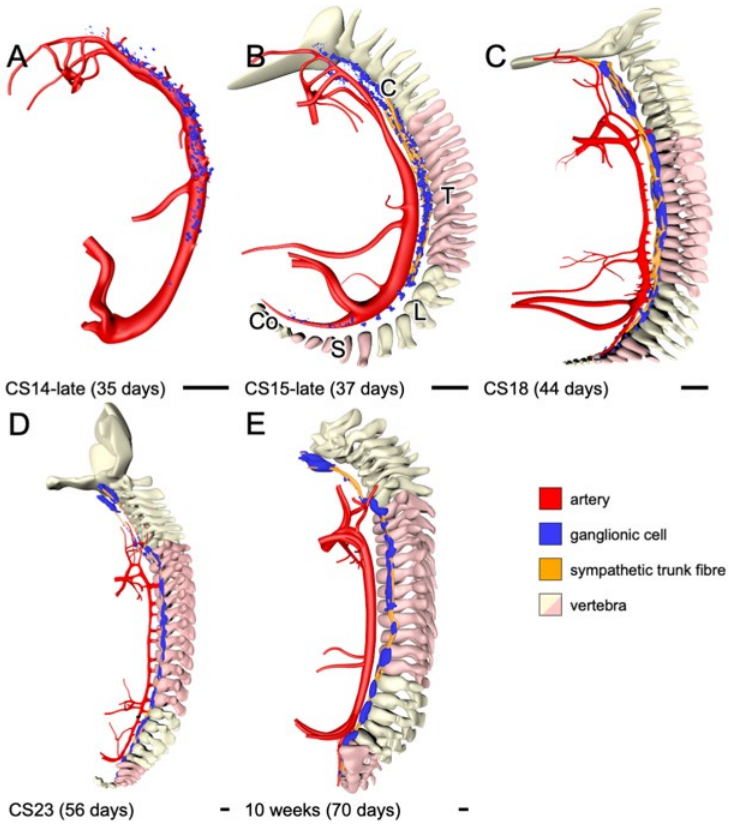

Figure 5.6 **Changes in the topographical position of the sympathetic trunks.** Panels A-E show left-sided views of the topography of the sympathetic trunks relative to the aorta and vertebral column. At CS14-late (~35 days) and before a vertebral column can be recognized, the ganglionic cells (blue) at the cervical (C) and thoracic (T) levels occupy a para-aortic position. At CS15, the mesenchymal condensations of the vertebrae have appeared (panel B; (Mekonen et al., 2015)). At this stage, sympathetic ganglionic cells and nerve fibres at the cervical, thoracic, and lumbar levels have acquired a position between aorta and vertebral column (prevertebral). Only the sympathetic trunks in the thoracic region shift further dorsally to acquire a paravertebral position at CS23 and an even more distinct paravertebral position at 10 weeks (upper pink region in panels C-E). In contrast, the sympathetic trunks in the sacral region retain their para-aortic and simultaneously prevertebral position (lower pink region in panel C-E; cf. black-lined rectangles in Figure 8). Bars = 500 µm.

To quantify the change in the position of the sympathetic trunks relative to the vertebral bodies, we measured 4 distances between landmarks surrounding the sympathetic trunks, including the middle of the floor plate of the spinal cord, the notochord (the vertebral column becomes identifiable only at CS15-late), the centres of the sympathetic trunks, and the middle of the dorsal aortic wall. All distances were measured at 4 vertebral levels: T2, T7, L1, and S1 (Figure 5.7A). The distances between the floor plate of the spinal cord and the notochord (line AB, Figure 5.7B) increase at a similar rate at all measured vertebral levels. The distance increases between CS16 and CS18, plateaus temporarily between CS18 and CS23, to increase again thereafter. The line connecting the notochord and the dorsoventral position of the centres of the sympathetic trunks (line BE, Figure 5.7C) hardly changes until CS21, after which the thoracic lines decline abruptly, in agreement with the change in position of the sympathetic trunks to paravertebral. At the lumbar and sacral levels, however, this distance hardly changes until CS23, after which it increases between weeks 9 and 10. The data in panels B and C indicate overall vertebral growth at the lumbar and sacral levels without change in position of the trunks. The distance between the left and right columns of the sympathetic trunk (line CC, Figure 5.7D) and that between the sympathetic trunks and the dorsal aortic wall (line CD, Figure 5.7E) change with a similar pattern: steady growth between CS15 and 9 weeks, which is most pronounced in the upper thoracic region and slowest in the sacral region, with T7 and L1 again taking intermediate positions. At all vertebral levels, growth accelerates in the 10th week.

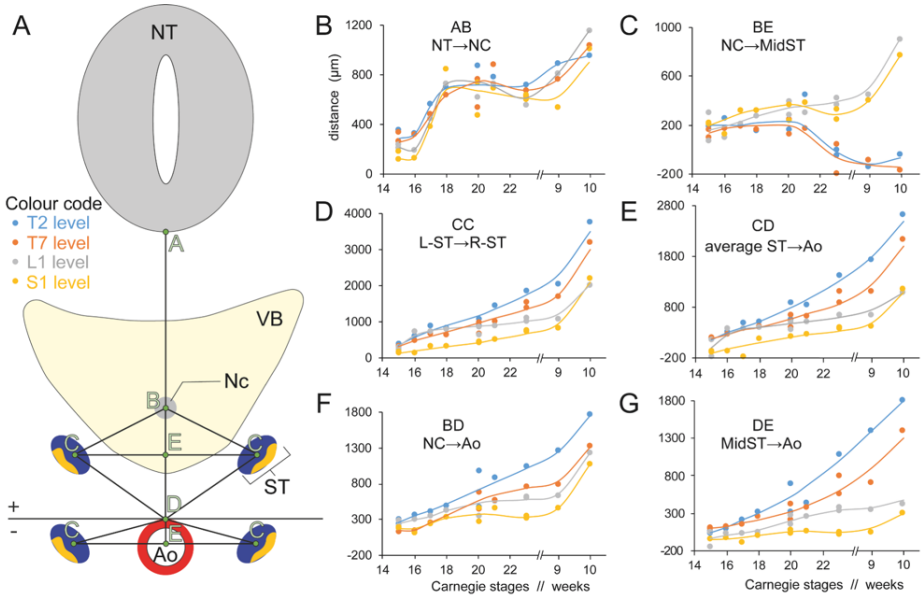

Figure 5.7 **Changes in topographical position of the sympathetic trunks along the vertebral column.** Panel A shows the landmarks and distances measured or calculated. Panels B-G show the distances indicated by landmarks in panel A at 5 different vertebral levels: T2 (blue lines), T7 (orange lines), L1 (grey lines) and S1 (yellow lines). Note that distances acquire negative values when the sympathetic trunks (landmark C) pass the horizontal line through landmark D, which happens when landmark C lies lateral rather than dorsolateral to the aorta. The distances between the floor plate of the spinal cord and the notochord (line AB, panel B) change in a comparable fashion at all measured vertebral levels: a rise between CS16 and CS18, a plateau between CS18 and CS23, and then again a rise. The distance between the notochord and the middle of the bilateral sympathetic trunks (line BE, panel C) shows little change until CS21, after which the thoracic lines decline abruptly, due to a dorsal relocation of the sympathetic trunks relative to the vertebrae. The lumbar and sacral lines, instead, show little change in position until they rapidly increase in length between weeks 9 and 10. The distance between both sympathetic trunks (line CC, panel D) and average distances (left and right) between the sympathetic trunks and aorta (line CD, panel E) change according to a similar pattern: steady growth between CS15 and 9 weeks, which is faster cranially than caudally, followed by an acceleration between 9 and 10 weeks. The distance between the aorta and the middle of the bilateral sympathetic trunks (line BD, panel F) or the notochord (line DE, panel G) increases with different characteristics along the vertebral column: at the thoracic level there is a smooth increase in distance between CS15 and 9 weeks, after which growth accelerates, but more caudally, the growth rate increasingly resembles that seen in panel B, indicating that the vertebrae grow more homogeneously in all directions at the lumbar and sacral levels. Abbreviation: VB; vertebral body.

The distance between the aorta and the notochord (line BD, Figure 5.7F) or the aorta and the middle of the bilateral sympathetic trunks (line DE, Figure 5.7G) increases with different characteristics along the vertebral column: at the thoracic level there is a

smooth increase in distance between CS15 and 9 weeks, after which growth accelerates; more caudally, the growth rate increasingly resembles that seen in Figure 5.7B, further supporting the conclusion from panels B and C that the caudal vertebrae expand more homogeneously in all directions. In aggregate, these findings show that differential growth causes the sympathetic trunks in the thoracic region to change position in dorsolateral direction relative to the aorta, whereas the sacral region experiences more homogeneous growth so that the original position of the sympathetic trunks is virtually retained. The data further show that only the thoracic sympathetic trunks assume a paravertebral position, and that this change in position occurs between CS20 and CS23, that is, during the 8th week of development. The outcome of these measurements is presented schematically in Figure 5.8.

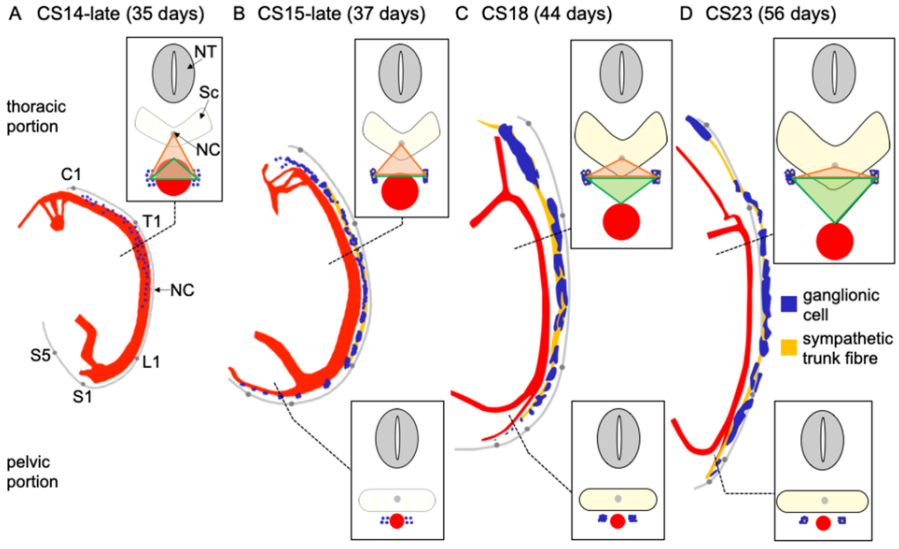

Figure 5.8 **Regional patterns in the changing topography of the sympathetic trunks.** Panels A-D shows the topography of developing sympathetic trunks between 5 and 8 weeks of development. The dotted lines indicate segmental level T1 and S1, and the boxed subpanels the corresponding schematic sections. The upper row of boxes shows the thoracic cross sections and the lower row the sacral ones. To demonstrate the topographical change in sympathetic trunks, two triangles were drawn. Both triangles share their bases in the centres of both sympathetic trunks. The ventral triangles (green) have their apices on the dorsal wall of the aorta, whereas the dorsal triangles (orange) have them on the notochord. The scheme shows that the sympathetic trunks change their position from para-aortic at 5 weeks of development to paravertebral at 8 weeks of development in the thorax, but that no change in position occurs at the sacral level. Figure 5.7 demonstrates that the cranio-caudal difference in position occurs in the 8th week of development between vertebrae T7 and L1.

Discussion

The sympathetic trunk is part of the sympatho-adrenal lineage. Descriptions and illustrations of the migratory pathway and developmental appearance of the cells of the sympathetic trunks are often limited to the thoracic level, where the lineage is first identifiable and where the developing adrenal medulla is also present (Saito and Takahashi, 2015, Furlan et al., 2017, Chan et al., 2018). In the present study, we have studied the appearance of ganglionic cells and nerve fibres in the sympathetic trunks separately, using their morphological characteristics in the stained sections. We observed that the sympathetic trunks become recognizable as a chain of ganglionic cells in the cervical and upper thoracic levels of CS14 embryos. Although the time of first appearance of the sympathetic trunks was similar in our study and earlier reports (Kuntz, 1920, Woźniak et al., 2009), we localized the segmental level at which these early trunks formed as the lower cervical and upper thoracic levels, whereas Wozniak cs identified the mid-thoracic levels (Woźniak et al., 2009), and Kuntz the lower thoracic and upper lumbar levels (Kuntz, 1920). We based our assessment of the segmental levels on whole-body reconstructions of embryos and counting of the spinal ganglia in these reconstructions, whereas the method to assess segmental levels was not reported in the earlier studies (Kuntz, 1920, Woźniak et al., 2009). The elongation of the trunks is fast in cranial direction, but proceeds at a progressively slower pace in caudal direction to reach the coccygeal level only at CS22-23. The nerve fibres of the trunks and the communicating branches with the spinal nerves were established during CS15 and CS16. The typical pearls-on-a-string appearance of ganglia and nerve fibres became established during CS18, with the beads being markedly heterogenous in size, and irregular in appearance and distribution. Coincident with the formation of the neck, the cranial part of the trunks with the superior cervical ganglion became markedly longer after CS18. Furthermore, the trunks assumed a markedly more dorsolateral (prevertebral) position cranially than caudally, which was found to be due to differential growth of the surrounding mesenchyme (Figure 5.8).

Spatiotemporal changes in the developing sympathetic trunks

In standard textbooks, the ganglia of the sympathetic trunks are very homogeneous in size and distribution along the sympathetic trunks. This representation classically underlies the elegant pearls-and-necklace metaphor. The metaphor is also misleading, however, since we show that the pearls are markedly irregular in shape and

distribution along the necklace (Figure 5.8). The formation of the sympathetic trunk can be divided into three main steps. When the neural crest cells move ventrally to their para-aortic position, they pass in a metameric fashion through the cranial half of somites, only to re-aggregate again into a continuous chain of ganglionic cells lateral to the aorta [Figure 5.2; (Kulesa et al., 2009, Gammill and Roffers-Agarwal, 2010)]. Next, the sympathetic trunks extend non-metamerically along the entire post-cranial length of the embryo and produce nerve fibres (orange colour code in Figure 5.1). Trunk extension and production of nerve fibres starts in the lower cervical and thoracic regions, and extends from there in cranial and caudal directions, with extension and fibre formation progressing faster cranially than caudally (Figure 5.1). The relatively slow neuronal development in the pelvic region was also observed for other extrinsic nerve fibres that form in this region (Kruepunga et al., 2020a). Segmentation of the trunks into agglomerates of ganglionic cells and areas almost devoid of ganglionic cells is the final step in sympathetic trunk formation. This distribution of the sympathetic ganglia becomes more-or-less periodical in appearance at 7 weeks of development, but does not correlate well with segments or vertebrae (Figure 5.1D; cf. (Fernholm, 1971) for mouse embryos). The re-segmentation is also markedly irregular, with larger, seemingly fused ganglia and smaller, so-called intermediate ganglia (Figure 5.2I; (Wrete, 1959, Groen et al., 1987)). Re-segmentation is reportedly dependent on somitic segmentation (Goldstein and Kalcheim, 1991b, Gammill and Roffers-Agarwal, 2010), but may also be dependent on local factors (Kasemeier-Kulesa et al., 2005), and perhaps be related to the segmental distribution of preganglionic sympathetic nerves or communicating branches (Kasemeier-Kulesa et al., 2015).

Differential growth as cause of the succession of the primary and secondary sympathetic trunks

The succession of the primary by the secondary sympathetic trunks is mainly based on a change in topographical position. The para-aortic “primary” sympathetic trunks are the early craniocaudal strands of neural crest cells (Huber, 2006, Kameda, 2014), while the “secondary” or definitive sympathetic trunks occupy a more dorsolateral and, therefore, pre- or even paravertebral position (Kuntz, 1920, Gibbins, 1994). The ganglionic cells of the primary trunks still divide, but express an aminergic phenotype (Rothman et al., 1978, Cochard et al., 1979), suggesting that they already represent an early phase of differentiation. More recently, it was reported that the ganglionic cells of the primary sympathetic trunk acquired the paravertebral position of the secondary

trunk by backtracking along their original migratory pathway due to chemotactic attraction by preganglionic axons exiting the spinal cord (Kasemeier-Kulesa et al., 2015). In the present study we showed that regional differences in growth rate also contribute to the change in position of the sympathetic trunks. Obviously, both processes are not mutually exclusive.

While our observations suggest a role for vertebral growth, we wondered why the observed changes were limited to the thoracic region. In the 8th and 9th weeks, the midthoracic vertebrae stand out in being more advanced in the development of their neural arches than more cranial or caudal vertebrae (Mekonen et al., 2017). Interestingly, midthoracic development is also more advanced on the ventral side of the vertebrae. Between CS17 and CS19, a subcoelomic mesenchymal body of considerable size develops between the vertebral bodies and ribs dorsally, and the parietal pleura ventrally, only to rapidly disappear during CS20 and CS21 to allow expansion of the pleural cavity (Frick, 1949, Salzer, 1960). The removal of the subcoelomic mesenchyme by apoptosis also begins in the midthoracic region and does not seem to be dependent on the presence of lungs (Salzer, 1960, Norden et al., 2010). Furthermore, the rib cage rapidly widens and deepens starting at CS20, in particular in the midthoracic region (Okuno et al., 2019, Mekonen et al., 2015). These observations show that the midthoracic region is a leading centre of the development of the vertebral column and suggest that differential growth along the vertebral column is an important determinant of the dorsoventral position of the sympathetic trunk on the vertebral bodies. This timeline contrasts with the growth patterns of the lumbar and especially the sacral area, which only begin to accelerate in the 10th week of development. This finding is in line with our earlier observation that growth and closure of the neural arch of the sacral vertebrae is delayed relative to more cranial vertebrae, but resumes between 9 and 10 weeks of development (Mekonen et al., 2017)

The cranio-caudal difference in the position of the sympathetic trunks has thus far attracted relatively little attention due to the focus of studies on the thoracic region (see our Introduction). To address this issue, we show trunks and aorta schematically in Figure 5.8, which is based on the measurements shown in Figure 5.7. The lateral views of the sympathetic trunks and dorsal aorta clearly show that the distance between both structures is greatest cranially and smallest caudally, and the difference becomes more pronounced with development. The boxed schematic drawings reveal that the most pronounced regional growth differences in the thoracic region (top row of

rectangles) are present in the area between the bilateral sympathetic trunks on the one hand and the vertebrae (orange-coded triangles) or dorsal aorta (green-coded triangles) on the other hand. In fact, the base of the orange-coded triangle became ~2.5-fold wider between CS15 and CS21 in the thoracic area ("CC" in Figure 5.7D), but hardly increased in height in this period ("BE" in Figure 5.7C). After CS21, however, its height dropped dramatically to negative values in the thoracic area, which shows that the sympathetic trunks were acquiring a more dorsal position than the notochord. In contrast, the height of the orange-coded triangle remained unchanged in the lumbar and sacral area (Figure 5.7C). The green-coded triangle starts out with negative values because of the para-aortic position of the trunks, but increases steadily, in particular in the thoracic region. If the medial sacral artery can be taken as the caudal continuation of the dorsal aorta, the sympathetic trunks in front of the sacrum (bottom row of rectangles) maintain their original para-aortic position throughout life. The scheme, finally, indicates that the vertebrae grow, but the growth spurt after the 8th week of development has no effect on the topographical position of the sympathetic trunks.

Conclusion

Neural crest cells initially migrate and then form diffusely distributed sympathetic trunks in a para-aortic position. Differential growth of structures surrounding the sympathetic trunks then relocates the position of the sympathetic trunks to pre- or paravertebral. Simultaneously, the diffuse sympathetic ganglionic cells aggregate into ganglia with relatively ganglionic cell-free stretches in between.

Supplemental figures

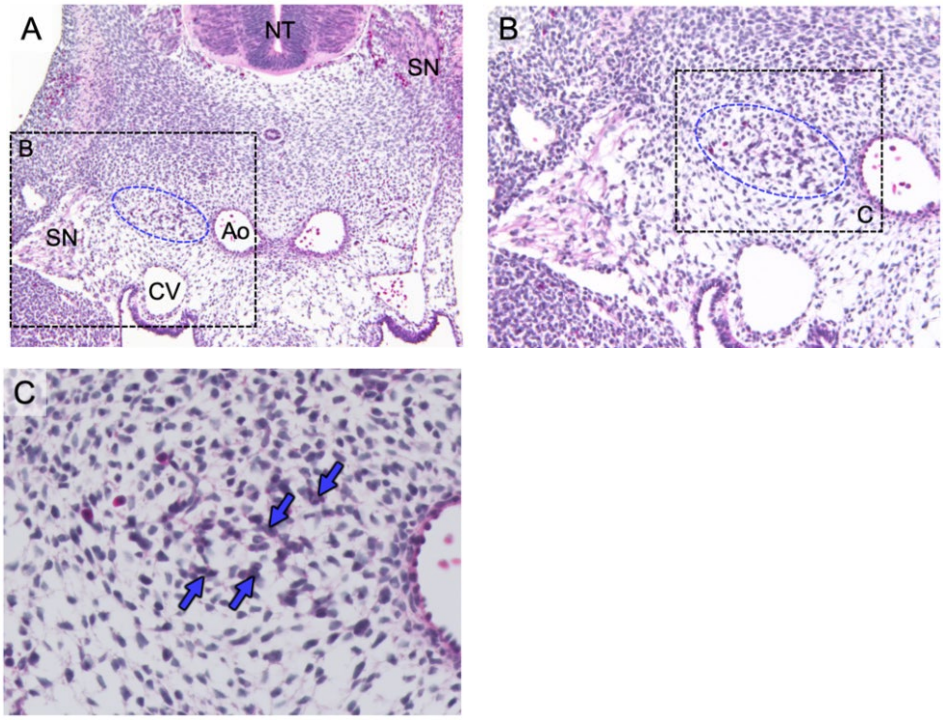

Figure S5.1 Morphological criteria to identify agglomerates of neural crest cells in early human embryos. The embryo was staged as Carnegie stage 14. The sections were stained with haematoxylin and azophloxine. The images were acquired on a Leitz microscope with 10x, 20x, or 40x objectives. Neural crest cells were strongly basophilic spindle-shaped cells, while nerve fibres were strongly acidophilic. In addition to the staining properties and shape of the cells, cell density and distribution proved critical criteria to identify and segment agglomerates of neural crest cells lateral and dorsolateral to the dorsal aorta (ellipse and circle, respectively). Cell density and distribution criteria were most informative when used at 10x or 20x magnification. Abbreviations: Ao, aorta; CV, cardinal vein; NC, notochord; NT, neural tube; SN, spinal nerve.

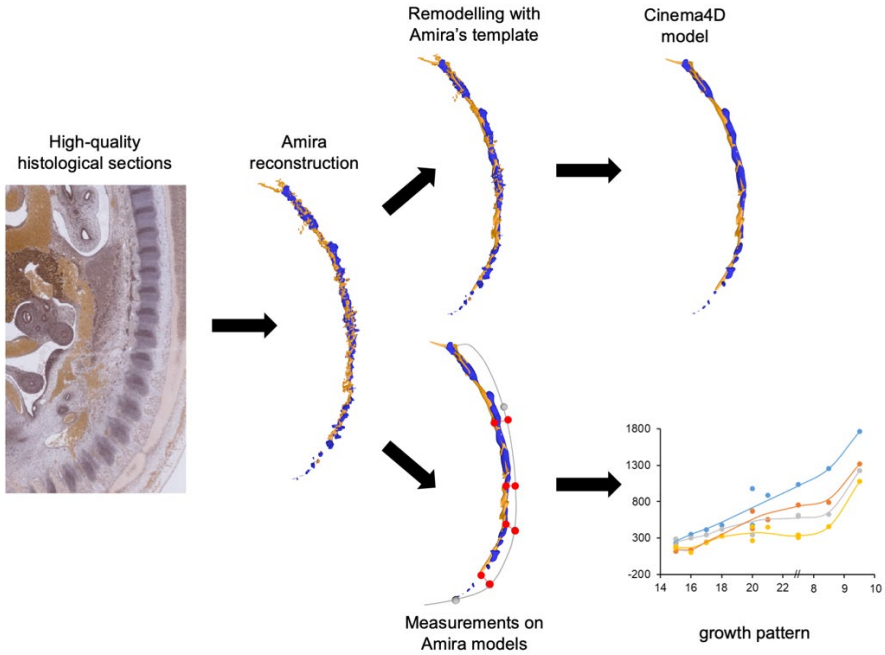

Figure S5.2 **Brief procedure of 3D analysis and rendering.**

Figure S5.3 **Interactive 3D pdfs of the sympathetic trunks of CS14 – CS18 embryos.**
Figure S5.4 **3D PDFs of the lesser pelvis of a CS18, CS20, and CS22 human embryo.**

Note! The interactive 3D-PDFs of the Supplemental Figures can be found in the digital version of the thesis on the USB stick, or directly downloaded from the journal website.

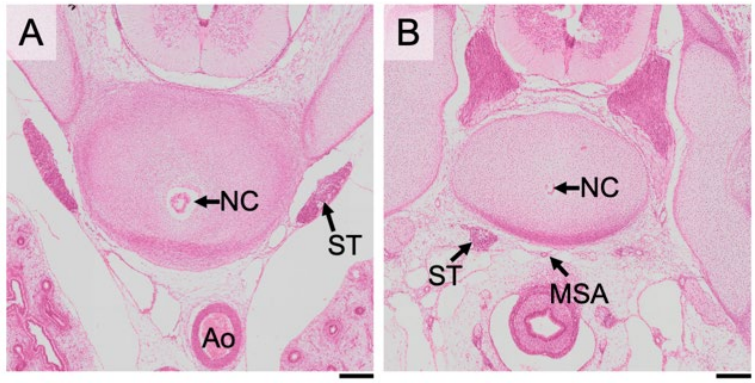

Figure S5.5 Comparison of the topography of sympathetic trunks at the thoracic (A) and sacral (B) regions in a 9 week foetus. Abbreviations: Ao, aorta; MSA, medial sacral artery; NC, notochord; ST, sympathetic trunk. Bar: 500 µm.

References

Andres KH, Kautzky R. (1955) [Early development of the cervical and cranial autonomic ganglia in man]. *Z Anat Entwicklungsgesch,* 119, 55-84.

Chan WH, Anderson CR, Gonsalvez DG. (2018) From proliferation to target innervation: signaling molecules that direct sympathetic nervous system development. *Cell and Tissue Research,* 372, 171-193.

Cochard P, Goldstein M, Black IB. (1979) Initial development of the noradrenergic phenotype in autonomic neuroblasts of the rat embryo in vivo. *Developmental Biology,* 71, 100-114.

Fernholm M. (1971) On the development of the sympathetic chain and the adrenal medulla in the mouse. *Zeitschrift für Anatomie und Entwicklungsgeschichte,* 133, 305-317.

Frick H. (1949) Über den Abschluß der Verbindung zwischen Pleura und Perikard bei menschlichen Embryonen. *Z Anat Entwickl geschichte,* 114, 230-241.

Furlan A, Adameyko I. (2018) Schwann cell precursor: a neural crest cell in disguise? *Developmental Biology,* 444, S25-S35.

Furlan A, Dyachuk V, Kastriti ME, et al. (2017) Multipotent peripheral glial cells generate neuroendocrine cells of the adrenal medulla. *Science,* 357.

Gammill LS, Roffers-Agarwal J. (2010) Division of labor during trunk neural crest development. *Developmental Biology,* 344, 555-565.

Gibbins I. (1994) Comparative Anatomy and Evolution of the Autonomic Nervous System. In *Comparative Physiology and Evolution of the Autonomic Nervous System* (eds Nilsson S, Holmgren S), pp. 1-68. Chur, Switzerland: Harwood Academic Publisher.

Goldstein RS, Kalcheim C. (1991a) Normal segmentation and size of the primary sympathetic ganglia depend upon the alternation of rostrocaudal properties of the somites. *Development,* 112, 327.

Goldstein RS, Kalcheim C. (1991b) Normal segmentation and size of the primary sympathetic ganglia depend upon the alternation of rostrocaudal properties of the somites. *Development,* 112, 327-34.

Groen GJ, Baljet B, Boekelaar AB, Drukker J. (1987) Branches of the thoracic sympathetic trunk in the human fetus. *Anatomy and embryology,* 176, 401-11.

His W (1890) Histogenese und Zusammenhang der Nervenelemente. *American Journal of Psychology,* 3, 544.

Huber K. (2006) The sympathoadrenal cell lineage: Specification, diversification, and new perspectives. *Developmental Biology,* 298, 335-343.

Kameda Y. (2014) Signaling molecules and transcription factors involved in the development of the sympathetic nervous system, with special emphasis on the superior cervical ganglion. *Cell Tissue Res,* 357, 527-48.

Kasemeier-Kulesa JC, Kulesa PM, Lefcort F. (2005) Imaging neural crest cell dynamics during formation of dorsal root ganglia and sympathetic ganglia. *Development,* 132, 235-245.

Kasemeier-Kulesa JC, Morrison JA, Lefcort F, Kulesa PM. (2015) TrkB/BDNF signalling patterns the sympathetic nervous system. *Nature Communications,* 6, 8281.

Kruepunga N, Hikspoors J, Hülsman CJM, Mommen GMC, Köhler SE, Lamers WH. (2020a) Development of extrinsic innervation in the abdominal intestines of human embryos. *J Anat,* 237, 655-671.

Kruepunga N, Hikspoors J, Hülsman CJM, Mommen GMC, Köhler SE, Lamers WH. (2020b) Extrinsic innervation of the pelvic organs in the lesser pelvis of human embryos. *J Anat,* 237, 672-688.

Kulesa PM, Lefcort F, Kasemeier-Kulesa JC. (2009) The migration of autonomic precursor cells in the embryo. *Autonomic Neuroscience,* 151, 3-9.

Kuntz A. (1910) The development of the sympathetic nervous system in mammals. *Journal of Comparative Neurology and Psychology,* 20, 211-258.

Kuntz A. (1920) The development of the sympathetic nervous system in man. *Journal of Comparative Neurology,* 32, 173-229.

Lumb R, Schwarz Q. (2015) Sympathoadrenal neural crest cells: The known, unknown and forgotten? *Development, Growth & Differentiation,* 57, 146-157.

Lutz G. (1968) Die Entwicklung des Halssympathicus und des Nervus vertebralis. *Zeitschrift für Anatomie und Entwicklungsgeschichte,* 127, 187-200.

Mekonen HK, Hikspoors JP, Mommen G, Köhler SE, Lamers WH. (2015) Development of the ventral body wall in the human embryo. *J Anat,* 227, 673-85.

Mekonen HK, Hikspoors JP, Mommen G, Kruepunga N, Köhler SE, Lamers WH. (2017) Closure of the vertebral canal in human embryos and fetuses. *Journal of Anatomy,* 231, 260-274.

Norden J, Grieskamp T, Lausch E, et al. (2010) Wt1 and Retinoic Acid Signaling in the Subcoelomic Mesenchyme Control the Development of the Pleuropericardial Membranes and the Sinus Horns. *Circulation Research,* 106, 1212-1220.

O'Rahilly R, Müller F. (2007) The development of the neural crest in the human. *J Anat,* 211, 335-51.

O'Rahilly R, Müller F. (2010) Developmental Stages in Human Embryos: Revised and New Measurements. *Cells Tissues Organs,* 192, 73-84.

Okuno K, Ishizu K, Matsubayashi J, et al. (2019) Rib Cage Morphogenesis in the Human Embryo: A Detailed Three-Dimensional Analysis. *Anat Rec (Hoboken),* 302, 2211-2223.

Paterson AM. (1890) Development of the sympathetic nervous system mammals. *Philosophical Transactions of the Royal Society of London. (B.),* 181, 159.

Pla P, Monsoro-Burq AH. (2018) The neural border: Induction, specification and maturation of the territory that generates neural crest cells. *Dev Biol,* 444 Suppl 1, S36-s46.

Pooh RK, Shiota K, Kurjak A. (2011) Imaging of the human embryo with magnetic resonance imaging microscopy and high-resolution transvaginal 3-dimensional sonography: human embryology in the 21st century. *American Journal of Obstetrics and Gynecology,* 204, 77.e1-77.e16.

Rothman TP, Gershon MD, Holtzer H. (1978) The relationship of cell division to the acquisition of adrenergic characteristics by developing sympathetic ganglion cell precursors. *Developmental Biology,* 65, 322-341.

Rubin E (1985) Development of the rat superior cervical ganglion: ganglion cell maturation. *The Journal of Neuroscience,* 5, 673.

Saito D, Takahashi Y. (2015) Sympatho-adrenal morphogenesis regulated by the dorsal aorta. *Mechanisms of Development,* 138, 2-7.

Salzer GM. (1960) Die Topogenese der Pleurahöhlen. *Z Anat Entwickl geschichte.,* 122, 232-240.

Streeter GL. (1912) The Sympathetic Nervous System (part 4 of The Development of the Nervous system). In *Manual of Human Embryology* (eds Keibel F, Mall FP), pp. 144-156. Philadelphia: J.B. Lippincott Co.

Theveneau E, Mayor R. (2012) Neural crest delamination and migration: From epithelium-to-mesenchyme transition to collective cell migration. *Developmental Biology,* 366, 34-54.

Vega-Lopez GA, Cerrizuela S, Aybar MJ. (2017) Trunk neural crest cells: formation, migration and beyond. *Int J Dev Biol,* 61, 5-15.

Woźniak W, Grzymisławska M, Lupicka J. (2009) The first appearance of sympathetic ganglia in human embryos at stage 13. *Folia Morphol (Warsz),* 68, 215-7.

Wrete M. (1959) The anatomy of the sympathetic trunks in man. *J Anat,* 93, 448-59.

Chapter 6
General discussion

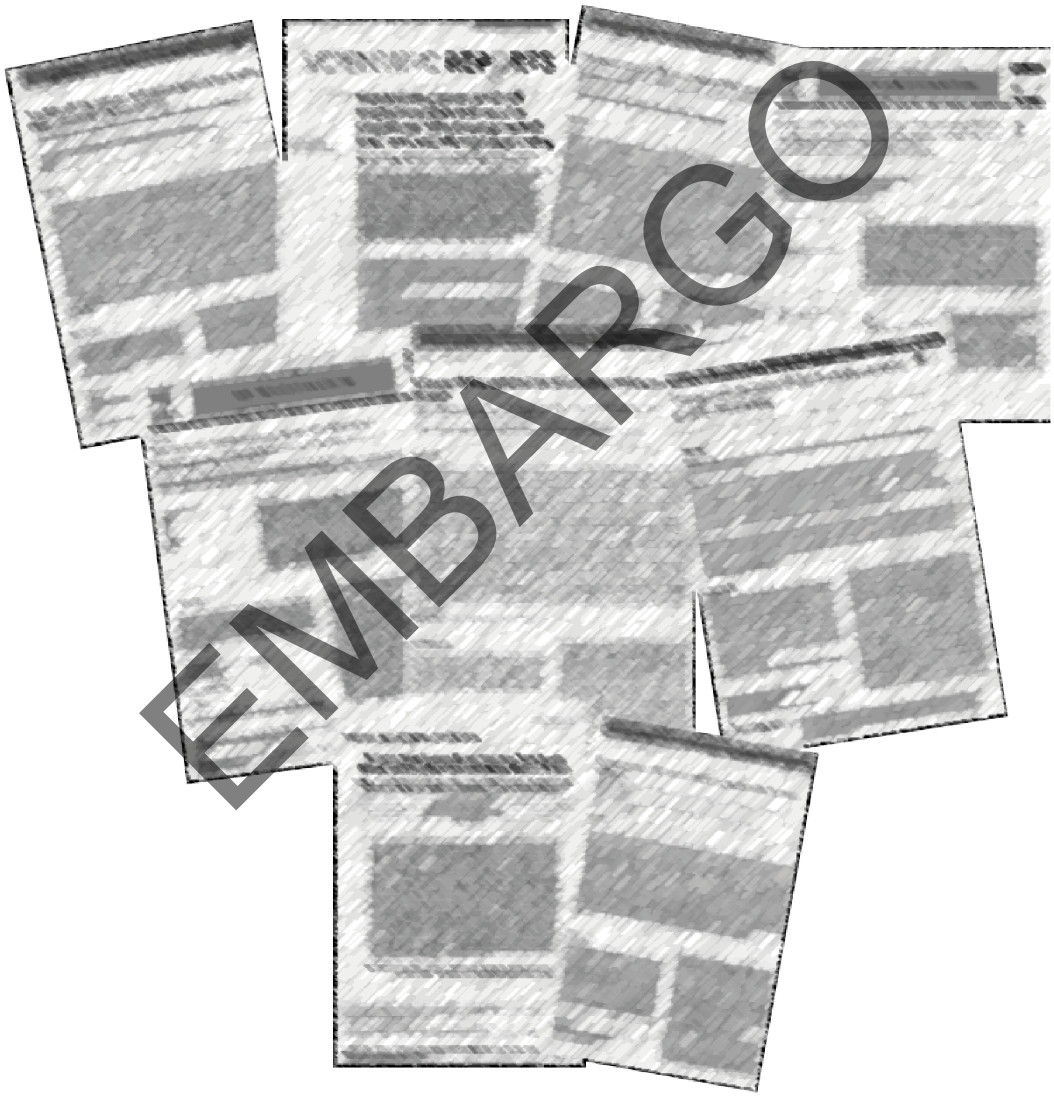

Chapter 7
Impact

Our studies have enhanced the understanding of the development of the caudal part of the body, in particular the gut. We have analysed 3D reconstructions of serial sections of human embryos and foetuses between 4 - 10 weeks of development. Visually, we emphasized the development of the gut, the vertebrae, the arteries, autonomic nervous structures, and some mesenchymal tissues in these 3D reconstructions. Informative pictures of relevant caudal structures of embryos and foetuses have, therefore, been visualised. The 3D modelling also allowed us to quantify growth of these structures relative to neighbouring structures and to growth of the embryo as a whole. The products of our reconstructions, therefore, confer a realistic "biography" on each of the structures mentioned above.

Educational impact

Several output tools can be used to enhance a clear understanding of 3D models and their developmental features. Firstly, such 3D-models can be used to compare or to confront definitive adult structures with their developmental ancestors or precursors. 3D modelling is a powerful tool to visualize the developmental path from an embryonic to an adult structure, which can be exported in a variety of formats. The key problem of teaching or learning developmental anatomy is that no realistic images are available for interrogation. In this sense, developmental anatomy differs from gross (adult) anatomy, which can be demonstrated on cadavers. Developmental morphology is commonly described with the help of drawings in which other processes cannot or have not been included and, hence, require imagination. In our approach, the first format that supports our descriptions digitally is the 3D PDF format which allows readers to inspect our models or their constituting parts from all sides. This format is as easily available for classrooms as lecture handouts. With this tool, students can interrogate the reconstruction database on their own computers in a similar way as they would use the lecture handouts. Although the 3D PDF format allows inspection of 3D embryonic structures, it does not allow students to directly compare different stages of development. We have investigated, therefore, whether printing our models physically would benefit students' understanding. Since we introduced physical 3D models of embryos in our classes, students gave feedback that such models allow them to understand changes in embryonic structures mentioned during lectures more easily than the 3D-PDF models alone. Our motto is "Better visualisation results in better understanding of (developmental) anatomy". In addition to digital and physical models,

therefore, we are presently testing other visualisation methods that may further enhance the transfer of knowledge.

Medical impact

Congenital malformations are among the more popular applications of developmental anatomy. We posit that comprehensive descriptions of developmental phenomena may lead to more accurate pathogenic models of congenital malformations. More accurate descriptions of normal development often entail better and potentially testable pathogenic mechanisms, and a better understanding of the associated dysfunction will probably result in a better repair procedure. Our study focused on the development in caudal body region where anorectal malformations are a common congenital anomaly. Most manifestations of this congenital malformation involve the cloacal subdivision. It has been described for years as being caused by the improper downgrowth of the urorectal septum or lateral folds. Our study described in chapter 2 suggests that the malformation is caused by the dysregulation of growth in the ventral and dorsal compartments of the cloaca. That study showed that the ventral cloaca is a growth area, whereas development of the dorsal cloaca is regressive and fails to show growth. In fact, our series of reconstructions strongly suggests that the formation of the urorectal septum results from the different growth modes in the dorsal and ventral parts of the cloaca. The changing shape of the vertebral column suggests that the early growth differences are also seen in the adjacent tissues. In persisting cloaca (no separation between dorsal and ventral components of the cloaca), dorso-ventral differences in growth are absent or less pronounced and only the ectodermal anal canal, if present, appears to represent the exit of the gut. The rectal fistulae, when present, do not develop randomly, but typically provide access to derivatives of the urogenital sinus, and suggest persisting continuity between the dorsal and ventral parts of the cloaca. Our data, therefore, suggest that the cause of cloacal malformations has to be sought in differential growth between the dorsal and ventral sides of the caudal end of the body (see Chapter 2, Figure 8). We would suggest that the focus of research should be a more detailed analysis of differential growth in the (human) embryo and a far more detailed description of the manifestations of anorectal malformations. We hypothesize that such data will further our understanding of anorectal malformations and, by knowing better what structures remain functionally intact, improve the outcome of surgical repair.

Samenvatting - Dutch summary

Samenvatting - Dutch summary

Gegeven de nog immer dalende aandacht voor de voorgeboortelijke ontwikkeling van de mens in het medisch curriculum, en de mogelijke rol daarbij van het ontbreken van ook maar enigermate natuurgetrouwe afbeeldingen van de organen van embryonen gedurende cruciale fasen in hun ontwikkeling heeft de Maastrichtse onderzoeksgroep "Ontwikkelingsanatomie van de mens" zich tot doel gesteld deze leemte te vullen. Het onderste deel van het lichaam, met name buik en kleine bekken, komt er in de gangbare tekstboeken bekaaid vanaf. Het onderzoek van de ontwikkeling van de cloaca, de extrinsieke innervatie van midden- en achterdarm, en de ontwikkeling van de grensstreng dat in dit proefschrift wordt beschreven is derhalve bedoeld om bij te dragen aan een topografische atlas van de mens in wording. Onze doelstelling is om iedere belangwekkende structuur van een biografie te voorzien. Onzes inziens faciliteert zo'n biografie van anatomische structuren, mits nauwkeurig en daardoor begrijpelijk, het eigen maken ('leren') ervan en vormt het een goede basis voor het ontwikkelen van functioneel effectieve interventies.

In **hoofdstuk 1** ("Introduction") worden de uitdagingen voor de boven uiteengezette doelstelling kort besproken. Het voorgeboortlijke anatomie van de mens lijkt ingewikkelder dan die van de volgroeide mens doordat structuren en organen groeien, maar niet allemaal even snel, m.a.w. de groei is differentieel en niet proportioneel. De resulterende veranderingen in vorm moeten in een tijdlijn worden vastgelegd, waarbij de veranderingen niet alleen in woorden, maar ook in ruimtelijke afbeeldingen zichtbaar moeten worden gemaakt. Om de (zelf-)studie te bevorderen moeten deze gegevensdragers zo mogelijk interactief te benaderen zijn. Ook moeten tekst en afbeeldingen gemakkelijk aan te passen zijn om de presentatie regelmatig te kunnen actualiseren.

Hoofdstuk 2 beschrijft de ontwikkeling van de cloaca in de mens. In 'lagere' gewervelde dieren is de cloaca ('riool') een ruimte waarop de achterdarm, de urinewegen, en de geslachtsgangen uitmonden, en van waaruit de respectieve producten uitgescheiden worden. Hoe de cloaca in zoogdieren onderverdeeld wordt in een urogenitale en een anorectale passage is nog steeds controversieel. Gebrek aan eenstemmigheid bestaat met name over de afgrenzing en daardoor de rol van het weefselschot tussen beide passages. Wij hebben dit probleem opnieuw bestudeerd met een kwantitatieve driedimensionale benadering in humane embryonen tussen 4

en 10 weken ontwikkeling (6-12 weken zwangerschapsduur). Digitale kopieën van de in dunne plakken gesneden embryonen die de basis voor ons onderzoek vormen, zijn afkomstig van de historische verzamelingen van de anatomische instituten van de Universiteit van Leiden, Amsterdam, Nijmegen en Göttingen. Voor reconstructie van de plakken tot driedimensionale structuren werd het Amira software pakket gebruikt, terwijl de ruwe oppervlakken van deze reconstructies met het Cinema4D software pakket werden gladgestreken. Afstanden tussen oriëntatiepunten werden met de Amira software berekend. Onze belangrijkste bevindingen zijn dat er een uitgesproken groeiverschil is tussen de snelgroeiende middelste en voorste delen van de cloaca en het langzaam tot niet groeiende bovenste en achterste deel. De ingang van de Wolffse gangen naar de cloaca bleek een stabiel oriëntatiepunt met een zich niet wijzigende positie ten opzichte van heiligbeenwervel S3. Door de geringe groei van het bovenste deel van de cloaca lijkt het alsof de ingang van de Wolffse gangen zich naar boven beweegt, terwijl de vrijwel afwezige groei van het achterste deel van de cloaca ertoe leidt dat de ingang van de achterdarm zich van boven naar achter in cloaca verplaatst. Deze positieverandering van de achterdarm van één die in het verlengde van de cloaca ligt naar één die haaks op de cloaca staat heeft de tijdelijk bestaande plooien van Rathke tot gevolg. Door de blijvende voor-achterwaartse groeiverschillen recht het gekromde uiteinde van het embryo zich en neemt het bindweefselschot tussen het groeiende voorste deel van de cloaca, de urogenitale sinus ('holte'), en de achterdarm een toenemend verticale positie aan. Dit schot staat bekend als het urorectale septum van Tourneux, en scheidt de urogenitale sinus en de achterdarm. De voor-achterwaartse groeiverschillen verdelen de cloacale membraan eveneens in een goed ontwikkeld voorste deel, de urethrale plaat, en een klein en dun achterste deel, de cloacale membraan in engere zin. Dat achterste deel scheurt op ~6.5 weken ontwikkeling open, en verschaft de urogenitale sinus en het anorectum een uitgang naar buiten. Het losse pericloacale bindweefsel groeit eveneens sneller aan de voor- dan achterzijde, hetgeen leidt tot de vorming van de genitale zwelling ('tuberculum genitale'). Het achterste deel van de cloaca verliest zijn holte vrijwel geheel rond 7 weken ontwikkeling. Of dit deel van de cloaca verdwijnt dan wel vanaf de 8ste week weer tot bloei komt is nog niet vastgesteld.

Vergeleken met het intrinsieke autonome zenuwstelsel van de darm is de ontwikkeling van het extrinsieke deel nog nauwelijks in kaart gebracht, ofschoon dat deel van het zenuwstelsel histologisch goed herkenbaar is. In hoofdstuk 3 hebben wij

deze ontwikkeling voor de buik beschreven. Het extrinsieke zenuwstelsel van de darm ontstaat uit kleine, intens kleurende neurale lijstcellen die zich eerst naar het gebied ter weerszijde van de lichaamsslagader begeven. Vervolgens begeven zij zich naar het gebied vóór deze slagader, om aldaar een uitgebreid netwerk van zenuwcellen en -vezels rondom de stam van de darmslagaders te vormen. Van hieruit breiden de autonome zenuwen zich uit langs deze slagaders richting de darmwand en maken tenslotte contact met het intrinsieke deel van het autonome zenuwstelsel. De zgn. 'Schwann cell precursors', een ondergroep neurale lijst cellen die zich op zenuwvezels verplaatsen, ontwikkelen tot de bijniermergcellen ter hoogte van de bovenste darmslagader en tot de meer compacte 'lichamen van Zuckerkandl' ter hoogte van de onderste darmslagader. Het extrinsieke autonome zenuwstelsel van de darm breidt zich achtereenvolgens uit langs de bovenste darmslagader, vervolgens de middelste en tenslotte een kleine week later langs de onderste. Afgezien van een tak naar de blinde darm breiden de extrinsieke zenuwen zich pas uit langs de middelste darmslagader als de bijbehorende darmlissen zich vanuit de zgn. fysiologische navelbreuk terug naar de buikholte hebben begeven (~9.5 weken ontwikkeling). Mogelijk wordt de groei van dit deel van het autonome zenuwstelsel dus afhankelijk van de aanwezigheid van de darm in de buikholte. De ingroei van het intrinsieke autonome zenuwstelsel van de darm leidt tot differentiatie van de darmwand. Als we deze differentiatie als afgeleid kenmerk van de ingroei van intrinsieke zenuwcellen kunnen aanmerken, volgt de extrinsieke innervatie de interne met een vertraging van ~2 weken.

Natuurgetrouwe afbeeldingen van de ontwikkeling van het autonome zenuwstelsel in het kleine bekken zijn schaars. In **hoofdstuk 4** laten we de ontwikkeling van het onderste 'hypogastrische' netwerk ('plexus') zien en de verbindingen ervan met het lokale ruggenmerg en de grensstreng. We hebben het embryonale kleine bekken gedefinieerd als het gebied onder de beide navelstrengslagaders. Het embryonale bekken komt topografisch dus goed overeen met wat in de volwassen anatomie het hypogastrische gebied heet. Neurale lijst cellen zijn vanaf 5 weken ontwikkeling schuin achter de middelste heiligbeenslagader ter hoogte van de 1ste heiligbeenwervel te vinden, en een dag later ook ter hoogte van de 5de heiligbeenwervel. Naast deze slagader aangekomen vormen de neurale lijstcellen het onderste deel van de grensstreng of bewegen naar het gebied vóór de slagader, alwaar ze aan beide zijden de onderste 'hypogastrische' opeenhoping van ganglioncellen vormen. Anders dan bij de hoger gelegen autonome zenuwnetwerken vóór de lichaamsslagader, blijven beide

hypogastrische opeenhopingen van elkaar gescheiden, omdat ertussen een tijdelijke uitstulping van de lichaamsholte aanwezig is. Hoewel de neurale lijstcellen in het kleine bekken zich later in de ontwikkeling naar voren beginnen te verplaatsen dan de neurale lijstcellen in de buik, komen zij tegelijkertijd op hun positie vóór de slagader aan. De bovenste hypogastrische zenuw, een uitbreiding naar onderen van de autonome darmzenuwen in de onderbuik langs de bovenste achterdarmslagader, bereikt de onderste hypogastrische zenuwcelopeenhoping slechts een dag later dan de takken naar vóren van dezelfde autonome darmzenuwen in de onderbuik het netwerk van zenuwcellen rond de onderste darmslagader bereiken. De bovenste hypogastrische zenuw splitst zich daarna op in een aantal takken die het bovenste hypogastrische netwerk zullen gaan vormen. Door de ingroei van vezels van de bovenste hypogastrische zenuw, op ~6.5 en ~8 weken ontwikkeling gevolgd door takken uit respectievelijk het lokale ruggenmerg en de grensstreng, wordt de onderste hypogastrische zenuwcelophoping omgevormd tot een netwerk van zenuwcellen en -vezels. Vervolgens wordt dit onderste hypogastrische netwerk opgedeeld in delen op de blaashals en het onderste deel van de achterdarm. De cloaca lijkt geen eigen autonome zenuwvoorziening te hebben.

Hoewel de ontwikkeling van de grensstreng al >100 jaar geleden beschreven is hebben de topografische aspecten ervan relatief weinig aandacht gekregen. In hoofdstuk 5 beschrijven wij onze bevindingen. Verspreid liggende, intens kleurende, van de neurale lijst afkomstige zenuwcellichamen vormen beiderzijds van de lichaamsslagader langgerekte celkolommen in het hals en bovenste borstkastgebied van ~5 weken oude embryonen. Zenuwvezels die de grensstreng met het ruggenmerg verbinden bereiken de grensstrengen na ~5.5 weken ontwikkeling en komen willekeurig tussen de zenuwcellen te liggen. Na ~6 weken ontwikkeling gaan de zenuwcellen onregelmatig gevormde celophopingen vormen op een van boven naar onderen continue streng zenuwvezels. Aan de achterzijde van deze streng zitten meer cellichamen en aan de voorzijde meer zenuwvezels. Tezamen vormen ze het beeld van een parelketting, maar de grootte en de verdeling van de parels zijn onderling opmerkelijk verschillend. De positieverandering van beide grensstrengen van naast naar schuin boven de lichaamsslagader (van ‘pre-’ naar ‘paravertebraal’) is een maatstaf om de ‘primaire’ van de ‘secondaire’ grensstrengen te onderscheiden. Om deze maatstaf te toetsen hebben we de topografische positie van de grensstrengen op wereldniveaus T2, T7, L1, en S1 vastgesteld. Na ~5 weken ontwikkeling bezetten de

strengen een positie naast de lichaamsslagader. Deze positie verandert in nek en boven in de borstkas in de 6de week, onder in de borstkas na 6 weken, en in het lendengebied na 7 weken naar 'prevertebraal'. De grensstrengen van de borstkas migreren nog verder naar achteren langs de wervelkolom naar een paravertebrale positie op ~8 weken ontwikkeling. In het kleine bekken behouden de grensstrengen hun positie naast de sacrale slagader. Ons baserend op de huidige en eerdere metingen en op de literatuur concluderen we dat het verschil tussen primair en secundair alleen het effect van differentiële groei in de verschillende delen van de wervelkolom en zijn omgeving weerspiegelt.

In **hoofdstuk 6** (General Discussion) tenslotte bespreken wij hoe differentiële groei kan leiden sterk gekronkelde topografische grenzen van structuren. We geven de grens tussen romp en bekken als voorbeeld, maar bespreken, omdat vvornoemde grens weinig onderzocht is, de veel uitgebreider onderzochte grens tussen romp en hoofd. Op basis van deze literatuurstudie komen we tot de definiëring van ontwikkelingsanatomie als het beschrijven van de volwassen anatomie aan de hand van een biografie van de wording van deze structuren. Wij denken dat die wijze van presenteren kan leiden tot nieuwe, meer functionele grenzen. Equivalenten van dit voorstel kan men volop in de dagbladen vinden – een bespreking van opvattingen of bevindingen van een auteur bevat vrijwel altijd ook een korte biografie van die auteur. Tenslotte bespreken wij hoe wij de kennis die wij met deze onderzoeklijn verwerven in het onderwijslandschap kunnen invoeren. In de in dit proefschrift beschreven artikelen gaan wij uit van verklarende teksten en interactieve 3D-PDFs als output, maar waarschijnlijk zijn andere leermiddelen, zoals fysieke 3D-modellen, evenzeer nodig om het 3-dimensionale aspect van ontwikkelingsanatomie op studenten over te brengen.

Tenslotte wordt in **hoofdstuk 7** de potentiële impact van dit proefschrift en het daarin beschreven onderzoek besproken. Wij maken onderscheid in wetenschappelijk impact (publicaties en daarna citaties) en onderwijskundige impact (meer uitgebreid in hoofdstuk 6 besproken). Onder het kopje 'medische impact' komen de consequenties van het onvoldoende begrijpen van de ontwikkeling van structuren aan de orde. Wij pleiten voor modellen waarin de consequenties van storingen in differentiële groei een grotere rol spelen.

Acknowledgements

Acknowledgements

I once had a dream that I would like to graduate abroad. That seemed impossible after I had decided to start my PhD in Thailand. When all of you read this message, it means that you all make my dream came true. I, therefore, have many words to say "thank you" for this memory.

Firstly, my lovely professors "Wout and Leo". For Wout, I would like to say thank you for this opportunity which you gave me to do research in Maastricht. It was a magnificent time for me to learn academic and non-academic skills. I don't know the word I should use but you give me an unforgettable memory. For Leo, I cannot exactly define your role. I think you are a good teacher and caring person. You gave me both academic and non-academic things. I remember very well that you gave me many packages of Thai food with English recipes because my weight was decreasing significantly. I should stop here before I cry, but thank you so much.

Secondly, my advisors, Dr. Uthaiwan, Dr. Somluk and Dr. Wattana. For Dr. Uthaiwan, I would like to say thank you so much. You are always my great teacher. You did me a favour to serve as an advisor for my bachelor project. You tried to find many people to help me with my project. You offered me my first step in academic life and supported me when I needed it. Drs. Somluk and Wattana, I would like to thank for all the support both of you always gave me. It is now more than a decade ago that I started my bachelor project. You gave me unconditional support to do research in an area that was out of your field at that time. I could not have come this far without the help of both of you. Both of you also taught me a lot of things in scientific and real life, and you still support me as a colleague in the department.

Thirdly, my great teachers, Mrs. Thanuttha and Mrs. Wanpen. For me, you are my great teachers who gave me advice. Both of you are my guides when I do not have any answer what I should do. Mrs. Thanuttha, you were my inspiration to study Biology, although we always discussed the choice between animals and plants. Mrs .Wanpen, you were a mother for me, who always had suggestions when my life was tough.

Fourthly, my great team mates, Jill and Cindy. Jill, you were my friend who managed everything in our lab. You always had manuals or solutions for everything when it was needed. You always discussed with me when I could not find an answer. I have really

appreciated to learn to know you and be team member. Don't cry Jill ☺. To Cindy, I would like to say thank you, because you did not leave me alone in a big room where I was presenting something in front of my computer and you saw it. I am happy that you are continuing the development of the caudal part of the body that I started. I am waiting to see how your findings in female embryos compare to mine in male embryos. I do not know what more I can say to both of you. One thing I would like is to just stay in touch. I hope we can collaborate to make developmental anatomy alive and innovative.

Fifthly, my second home, the Department of Anatomy & Embryology at Maastricht University. My feeling for this department is that it is my second home. You all made my life easier when I was here. I got warmth from all of you, funny stories from Thomas and Johan, Dutch words from Leon, and inspiration for my trips from Sandra and Nicole. You made me feel comfortable in Maastricht where everything is different in my experience. I would like to say thank you for all you have given me for almost 4 years in Maastricht. Keep in touch.

Sixthly, TSAM (Thai students association in Maastricht including P'Lek, P'Som-O, P'Pui, Ice, New, Yada and Jul). Thank you all for the parties, food and warmth in Maastricht. Ploingam, I would like to say thank you from my heart. You are always besides me when things were difficult. Mrs .Anong, thank you for the meals and cheerful power you gave me during these years. The most memorable thing in my mind is the day that my bag was stolen. You helped me so much. You made my life easier in Maastricht.

Seventhly, my family. I know that you cannot understand what I have written down here, but I know you can feel what I mean. Thank you all for giving me unconditional support.

Lastly, myself. Thank you so much for the hidden power. It gave me a lot of energy to fulfil this dream. Everyone now knows you can do it. You can pass through your comfort zone to become a better you. You have done it, NK.

Thank you for this great memory
"Dank u wel"
NAC

Curriculum Vitae

Curriculum vitae

Nutmethee Kruepunga, NAC, was born on March 30th, 1990 in Bangkok, Thailand. In 2008, he received his secondary school diploma from Donmuang Chaturachinda School in Bangkok. After completing secondary school, he moved to Kasetsart University for his bachelor degree of Science in Biology and graduated with first class honours. In 2012, he decided to continue his doctoral study in Anatomy and Structural Biology at the Faculty of Science, Mahidol University, Bangkok, Thailand. During his stay at both universities, he was supported by the Development and Promotion of Science and Technology talents project (DPST). In his bachelor and doctoral projects, he prepared and studied 3D reconstructions of embryos, starting with chick embryos during his bachelor study and changing to human embryos during his doctoral research. In December 2015, the DPST project also granted him an internship at the Department of Anatomy & Embryology, Maastricht University, the Netherlands for a year. Therefore, his life moved to the Netherlands that month. In Maastricht University, he started his investigation in the caudal part of human embryos by 3D reconstruction. After the year had ended, he got the opportunity to become a PhD candidate in the Department of Anatomy & Embryology, Maastricht University. In May 2017, he defended his Thai PhD thesis in Bangkok, came back to Maastricht to complete his thesis there. Between December 2015 and December 2019, he won the best poster presentation of the Nederlandse Anatomen Vereniging, the best paper of 2018 award" of the Journal of Anatomy for the article entitled "The development of the cloaca in the human embryo", and was invited as a guest speaker on this topic at The Anatomical Society Winter meeting at Lancaster University, United Kingdom. Moreover, his cloaca story was mentioned as a key reference in Gray's Anatomy 42th edition. Currently, he is a lecturer at Department of Anatomy, Faculty of Science, Mahidol University. He obtained a New Researcher Grant from Mahidol University to carry out 3D reconstructions and image analysis in human embryos.

List of publications

Hikspoor JP, **Kruepunga N**, Mommen GM, Köhler SE, Anderson RH, Lamers WH. (2022). A pictorial account of the human embryonic heart between 3.5 and 8 weeks of development. Commun Biol. 5, 226.

Yurasakpong L, Nantasenamat C, Janta S, Eiamratchanee P, Coey J, Chaiyamoon A, **Kruepunga N**, Senarai T, Langer MF, Meemon K, Suwannakhan A. (2022). The decreasing prevalence of thyroid ima artery: a systematic review and machine learning assisted meta-analysis. Ann Anat. 239, 151803.

Prasatkaew W, **Kruepunga N**, Yurasakpong L, Korkong R, Ardsawang S, Ronglakorn S, Sananpanich K, Suksri S, Suwannakhan A. (2021). A reverse form of Linburg-Comstock variation with demonstration of 3D interactive portable document format. Surg Radiol Anat. 44, 227-232.

Kruepunga N, Hikspoors JP, Hülsman CJ, Mommen GM, Köhler SE, Lamers WH. (2021). Development of the sympathetic trunks in human embryos. J Anat. 239, 32-45.

Yurasakpong L, Yammine K, Limpanuparb T, Janta S, Chaiyamoon A, **Kruepunga N**, Meemon K, Suwannakhan A. (2021). The prevalence of the azygos lobe: a meta-analysis of 1,0233,083 subjects. Clin Anat. 34, 872-83.

Kruepunga N, Hikspoors JP, Hülsman CJ, Mommen GM, Köhler SE, Lamers WH. (2020). Development of extrinsic innervation in the abdominal intestines of human embryos. J Anat. 237, 655-71.

Kruepunga N, Hikspoors JP, Hülsman CJ, Mommen GM, Köhler SE, Lamers WH. (2020). Extrinsic innervation of the pelvic organs in the lesser pelvis of human embryos. J Anat. 237, 672-88.

Chandee N, **Kruepunga N**, Leckchaoum T, Thintharua P, Weerachatyanukul W, Asuvapongpatana S. (2020). Late administration of caffeine affects cardiac maturation in chick embryos: a combined two and threedimensional morphogenetic and gene analyses. Eur J Anat. 24(3), 211-20.

Hikspoors JP, **Kruepunga N**, Mommen GM, Peeters JM, Hülsman CJ, Köhler SE, Lamers WH. (2019). The development of the dorsal mesentery in human embryos and fetuses. Seminars in cell & developmental biology 92, 18-26.

Kruepunga N, Hakvoort TB, Hikspoors JP, Köhler SE, Lamers WH. Anatomy of rodent and human livers: What are the differences?. (2019). Biochimica et Biophysica Acta (BBA)-Molecular Basis of Disease. 1865, 869-78.

Kruepunga N, Hikspoors JP, Mekonen HK, Mommen GM, Meemon K, Weerachatyanukul W, Asuvapongpatana S, Eleonore Köhler S, Lamers WH. (2018). The development of the cloaca in the human embryo. J Anat. 233, 724-39.
"The best paper of 2018 in Journal of Anatomy"

Hikspoors JP, Peeters MM, Mekonen HK, **Kruepunga N**, Mommen GM, Cornillie P, Köhler SE, Lamers WH. (2017). The fate of the vitelline and umbilical veins during the development of the human liver. J Anat. 231, 718-35.

Mekonen HK, Hikspoors JP, Mommen G, **Kruepunga N**, Köhler SE, Lamers WH. (2017). Closure of the vertebral canal in human embryos and fetuses. J Anat. 231, 260-74.